Faculdade de Engenharia da Universidade do Porto

UPWIND - Converter connecting the DC bus to a single-phase power grid of an Airborne Wind Energy System

Cassien Alexandre Pereira Croisé

Mestrado em Engenharia Eletrotécnica e de Computadores

Supervisor: Maria Teresa Duarte Barroca Delgado

Second Supervisor: Carlos João Rodrigues Costa Ramos

July 23, 2024

Resumo

Os Sistemas de Energia Eólica Aerotransportada (AWES) estão a emergir como soluções inovadoras para o aproveitamento da energia eólica em ambientes onde as turbinas eólicas tradicionais são menos eficazes. Esta dissertação explora a integração de um conversor bidirecional que liga o barramento CC de um AWES a uma rede eléctrica monofásica no âmbito do projeto UPWIND. O objetivo principal é aumentar a eficiência da conversão de energia, assegurar uma sincronização contínua da rede e manter a estabilidade do sistema.

O estudo começa por introduzir o AWES e detalhar os princípios fundamentais dos conversores bidireccionais. É desenvolvida uma estratégia de controlo para enfrentar os desafios colocados pela corrente, proveniente do conversor CC/CA que liga o motor/gerador ao barramento CC, em que a amplitude pode variar significativamente. A investigação centra-se na conceção de um sistema de controlo que garanta uma regulação precisa da tensão.

São realizadas simulações exaustivas para validar a eficácia da estratégia de controlo proposta. Estas simulações demonstram a capacidade do sistema para manter um funcionamento estável em condições variáveis, apresentando o desempenho do conversor tanto em cenários normais como em cenários desafiantes.

Os resultados desta dissertação oferecem perspectivas significativas e soluções práticas para o projeto UPWIND, facilitando a integração eficiente e sustentável de AWES em redes eléctricas monofásicas. A estratégia de controlo desenvolvida e os dados de desempenho validados contribuem para o avanço da implementação de AWES, promovendo a utilização de fontes de energia renováveis em aplicações ligadas à rede.

Palavras-Chave: Sistemas Aéreos de Energia Eólica , rede monofásica, conversor bidirecional CC-CA, energias renováveis, projecto UPWIND.

Abstract

Airborne Wind Energy Systems (AWES) are emerging as innovative solutions for harnessing wind energy in environments where traditional wind turbines are less effective. This dissertation explores the integration of a bidirectional converter that connects the DC bus of an AWES to a single-phase power grid within the framework of the UPWIND project. The primary aim is to enhance energy conversion efficiency, ensure seamless grid synchronization, and maintain system stability.

The study begins by introducing AWES and detailing the fundamental principles of bidirectional converters. A control strategy is developed to address the challenges posed by the current, coming from the DC/AC converter connecting the motor/generator with the DC bus, in which the amplitude can vary significantly. The research focuses on designing a control system that guarantees a precise voltage regulation.

Extensive simulations are conducted to validate the effectiveness of the proposed control strategy. These simulations demonstrate the system's ability to maintain stable operation under varying conditions, showcasing the converter's performance in both normal and challenging scenarios.

The findings of this dissertation offer significant insights and practical solutions for the UPWIND project, facilitating the efficient and sustainable integration of AWES into single-phase power grids. The developed control strategy and validated performance data contribute to advancing the deployment of AWES, promoting the use of renewable energy sources in grid-connected applications.

Keywords: Airborne Wind Energy Systems, single-phase grid, bidirectional converter, renewable energy, UPWIND project.

Sustainable Development Goals for the United Nations

Adopted unanimously in 2015 by all UN Member States, the 2030 Agenda for Sustainable Development (2030 Agenda) with its 17 Sustainable Development Goals (SDGs), 169 targets, and 231 unique indicators shapes the direction of global and national development policies, and offers new entry points and opportunities for bridging the divide between human rights and development. It serves as the overall framework to guide global and national development action [1]. They recognise that ending poverty and other deprivations must go hand-in-hand with strategies that improve health and education, reduce inequality, and spur economic growth – all while tackling climate change and working to preserve our oceans and forests [2].

SDG	Goal	Contribution	Performance Indicators and Metrics
7	1	Promotion of the use of Airborne Wind Energy Systems (AWES) which harness wind energy at higher altitudes, making renewable energy more efficient and reliable.	**Energy Efficiency:** Efficiency of energy conversion (%) and **Renewable Energy Share:** Percentage of the total energy supplied by AWES.
	2	Enhances energy access by integrating renewable sources into the grid, potentially lowering costs and increasing reliability.	**Grid Stability:** Incidence of grid fluctuations or outages attributed to AWES and **Cost Reduction:** Reduction in energy cost per kWh due to AWES.
9	1	Enhance infrastructure resilience by integrating innovative AWES with existing power grids.	**Integration Success Rate:** Percentage of successful integrations of AWES with existing power grids, **Deployment Time:** Average time required to deploy AWES technology in new locations, **Infrastructure Resilience:** Metrics on the ability of the infrastructure to withstand adverse conditions (e.g., uptime percentage during extreme weather), **Grid Stability Improvement:** Reduction in power outages and fluctuations due to AWES integration, **Maintenance Costs:** Annual costs associated with maintaining AWES infrastructure and **User Satisfaction:** Satisfaction scores from utility companies and consumers.
	2	Promote industrial growth by developing a robust supply chain and local manufacturing capabilities for AWES components.	**Local Manufacturing Share:** Percentage of AWES components manufactured locally, **Employment Impact:** Number of jobs created in the local supply chain, **Supply Chain Efficiency:** Metrics on the time and cost efficiency of the local supply chain, **Economic Contribution:** Increase in local GDP due to AWES-related industrial activities, **Skill Development Programs:** Number of training programs conducted for the local workforce and **Community Feedback:** Feedback from local stakeholders on the economic impact.
11	1	Provide clean and reliable energy solutions to urban areas through AWES deployment.	**Urban Energy Supply Metrics:** Proportion of urban areas utilizing AWES for energy, **Reduction in Urban Pollution:** Decrease in pollution levels attributed to AWES and **Energy Reliability Index:** Improvement in energy reliability metrics for urban grids.
	2	Support urban planning initiatives by integrating AWES into city infrastructure.	**Urban Planning Integration:** Number of urban planning projects integrating AWES, **Sustainable Development Measures:** Metrics on how AWES contributes to sustainable development in urban areas and **Urban Resilience Index:** Increase in urban resilience against energy disruptions.
13	1	Reduce greenhouse gas emissions by increasing the use of renewable wind energy.	**CO2 Emissions Reduction:** Tons of CO2 emissions avoided annually due to AWES, **Renewable Energy Adoption:** Increase in the percentage of energy from renewable sources and **Environmental Impact Assessment:** Score from environmental impact assessments.
	2	Enhance community awareness and preparedness for climate change impacts through renewable energy education and deployment.	**Community Awareness Index:** Increase in awareness levels in communities where AWES is deployed, **Climate Action Programs:** Number of educational programs or initiatives launched and **Public Engagement Metrics:** Community participation rates in climate action programs.
17	1	Foster global partnerships to advance renewable energy technologies and share knowledge.	**Partnership Formation Metrics:** Number and effectiveness of partnerships formed, **Technology Transfer Cases:** Number of successful technology transfers involving AWES and **Joint Research Publications:** Number of publications resulting from global partnerships.
	2	Attract investment and funding for large-scale deployment of AWES technologies.	**Investment Metrics:** Total amount of investment secured for AWES projects, **Funding Sources Diversity:** Diversity of funding sources (public, private, international) and **Project Scaling Metrics:** Rate of scaling and deployment of AWES technologies globally.

Acknowledgement

I’m grateful for my parents’ and coordinators’ support.

I would like to express my deepest gratitude to all those who supported me throughout this project.

First and foremost, I am immensely thankful to my supervisors, for their invaluable guidance, expertise, and encouragement. Their continuous support and insightful feedback were crucial in navigating the challenges and complexities of this research.

I am also grateful to my parents, whose unwavering support and belief in me provided the foundation for my academic pursuits. Their encouragement has been a source of strength and inspiration throughout my educational journey.

Special thanks to my colleagues and friends at the FEUP for their collaboration, discussions, and camaraderie, which enriched this project and made this experience truly memorable.

Lastly, I would like to extend my appreciation to everyone involved in the UPWIND project, whose collective efforts and innovative spirit made this research possible. Their commitment to advancing Airborne Wind Energy Systems has been a source of inspiration.

Cassien Alexandre Pereira Croisé

*"Non exiguum temporis habemus,
sed multum perdidimus"*

Seneca - De Brevitate Vitae I-III

Contents

List of Figures

List of Tables

Abbreviations and Symbols

AC	Alternating Current
ADC	Analog-to-Digital Converter
AWES	Airborne Wind Energy Systems
BAT	Buoyant Airborne Turbine
BJT	Bipolar Junction Transistor
CCS	Continuous Control Set
DC	Direct Current
DPC	Direct Power Control
DSPs	Digital Signal Processors
DTC	Direct Torque Control
FCS	Finite Control Set
FCS-MPC	Finite Control Set Model Predictive Control
FPGAs	Field Programmable Gate Arrays
GaN	Gallium Nitride
IGBT	Insulated Gate Bipolar Transistor
LUT	Look-Up Tables
MOSFET	Metal-Oxide-Semiconductor Field-Effect Transistor
MPC	Model Predictive Control
PI	Proportional Integral
PLL	Phase-Locked Loop
PR	Proportional Resonant
PWM	Pulse-Width Modulation
RMS	Root Mean Square
SDGs	Sustainable Development Goals
SHE-MPC	Selective Harmonic Elimination Model Predictive Control
SiC	Silicon Carbide
SPWM	Sinusoidal Pulse-Width Modulation
THD	Total Harmonic Distortion
VOC	Voltage-Oriented Control
VSI	Voltage Source Inverter
WPD	Wind Power Density
ZOH	Zero-Order Holds

Chapter 1

Introduction

1.1 Context

Airborne Wind Energy Systems (AWES) have emerged as a groundbreaking frontier in renewable energy, promising to revolutionise the way wind power is captured. Unlike traditional wind turbines that are grounded to the earth, AWES ascend to higher altitudes, where wind currents are more consistent and powerful. This innovative approach not only capitalizes on stronger winds but also addresses challenges related to land use and installation constraints, making AWES a compelling alternative in pursuing sustainable energy solutions.

As these systems continue to advance, the seamless integration of their energy generation into existing grids becomes paramount. This integration is facilitated by two essential components: the initial bidirectional converter, linking the generator's alternating current (AC) output to the internal direct current (DC) bus, and the second one, connecting the DC bus to a single-phase grid.

1.2 Goals

This dissertation centres its focus on the converter connecting the DC bus to the single-phase grid. Unlike conventional wind energy systems, the variable nature of airborne wind necessitates adaptability and precision in energy conversion. The converter plays a pivotal role in this context, transforming the stable DC power from the bus into the requisite AC for grid connection.

Apart from its technical complexity, the converter also has significant practical implications. Its ability to ensure the smooth transition of energy determines the efficiency, stability, and reliability of the entire energy transfer process. This dissertation comprehensively explores the converter's operational principles, and control algorithms to shed light on its capabilities and limitations.

Through analysing the converter, it aims to clarify and simplify the complexities of integrating AWES, ultimately paving the way for a more sustainable energy future. This study makes a significant contribution toward enhancing energy sustainability.

Another goal for this dissertation is to fulfil the academic requirements for the degree of Master of Science in Electrical and Computer Engineering.

1.3 Dissertation Structure

This dissertation will be structured in the following manner:

- Chapter 1: Introduction - This chapter introduces the context, goals, and structure of the dissertation. It also outlines the motivation behind studying the integration of bidirectional converters in AWES as part of the UPWIND project.

- Chapter 2: Background of AWES - This chapter contains an overview of AWES, highlighting their advantages and different approaches. It details the benefits of AWES, such as their ability to access higher wind speeds and their reduced material usage compared to traditional wind turbines. The chapter also compares various AWES technologies and discusses competitors to the UPWIND project. The content aims to establish a foundation for understanding the context in which the UPWIND project operates.

- Chapter 3: Background and Literature Review of Bidirectional Converters - This chapter reviews the fundamentals of bidirectional converters, focusing on their topologies, control strategies, and modulation methods. It explores different control techniques, including PWM-based linear control and advanced methods without a modulator. The chapter emphasizes the importance of selecting appropriate converter topologies and control strategies to achieve efficient integration with AWES.

- Chapter 4: Modelling and Simulation - This chapter focuses on the modelling and simulation of the proposed bidirectional converter for the UPWIND project. It details the development of the converter's model, including the LCL filter and d-q transformation. The chapter presents simulations with both analogue and digital control, addressing various operational scenarios such as normal operation with load, current source, and alternate load. The results are compared to determine the effectiveness of the proposed system under different conditions.

- Chapter 5: Conclusion and Future Work - This chapter summarizes the key findings from the dissertation and discusses the implications for the UPWIND project. The chapter also outlines potential areas for future research, suggesting improvements and further investigations to enhance the integration and performance of AWES in single-phase grid systems.

Chapter 2

Background of Airborne Wind Energy Systems

2.1 Introduction

In this chapter, a brief overview of the background of Airborne Wind Energy Systems (AWES) will be given. A talk about how it works, about its different approaches, which approach the UPWIND project uses and about UPWIND's competitors will be given.

2.2 AWES and its advantages

The AWES represent an innovative class of wind energy technologies that utilize flying devices or tethered wings to harness wind power. These systems operate at high altitudes, capitalizing on stronger and more consistent winds compared to ground-level wind turbines. Airborne Wind Energy holds significant interest within the renewable energy sector for two primary reasons.

The first is that winds at higher altitudes exhibit substantially higher power density than those at ground level. Wind Power Density (WPD), illustrated in Figure 2.1, demonstrates an increase with altitude. The wind at elevated heights carries several times more power than ground-level winds. This disparity in power potential indicates a significant advantage for airborne systems over traditional wind turbines. As a conservative estimate based on the standard atmosphere, high-altitude winds carry approximately twice as much power as their low-altitude counterparts [3]. However, it's crucial to note that this estimation varies depending on the specific site characteristics.

The second is that the construction of structures for harnessing energy from high-altitude wind tends to be more lightweight and cost-effective. While conventional wind power methods involve building taller towers to access energy from laminar Airborne Wind ranges, this approach significantly increases costs. The escalation in tower expenses, larger rotor blade dimensions entering the bending range, and the need for disproportionate reinforcement curtails economic efficiency. In contrast, utilizing flying machines to capture Airborne Wind energy presents a more pragmatic

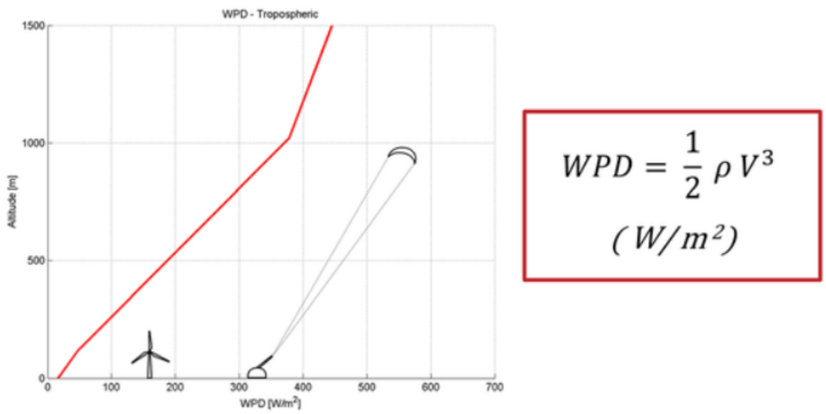

Figure 2.1: Chart showing the WPD (x-axis) variation with altitude (y-axis) [4].

and cost-effective solution. These lighter and adaptable flying systems circumvent the drawbacks associated with conventional tower-based methods, making the harvesting of high-altitude wind energy more economically feasible.

2.3 AWES approaches

There are three different approaches for the location of the generators of the AWES. The first one is the stationary generator. This approach uses the lift force of the flying machines to generate power by providing torque to the generators located on the ground [5]. In addition to the diverse methods of converting Airborne Wind energy, various approaches exist for generating the necessary lift force. The foremost among these is the YoYo approach, a harvesting technology where flying machines execute movements in the shape of a lemniscate, circular trajectory, or along a linear path [5]. Figure 2.2 illustrates these different flight paths. The two primary applications of the YoYo concepts, depicted in Figure 2.3, include the use of either hard kite or soft kite structures. Furthermore, the distinct harvesting methods associated with the YoYo concepts are detailed in Figure 2.4, showcasing the variability within this approach to harnessing airborne wind energy.

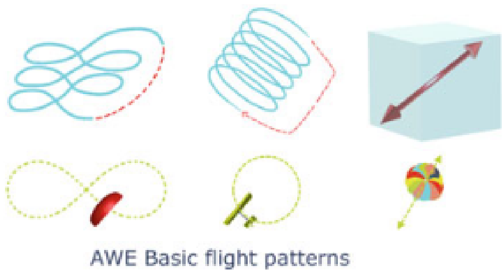

Figure 2.2: Flight patterns of the kite [5]

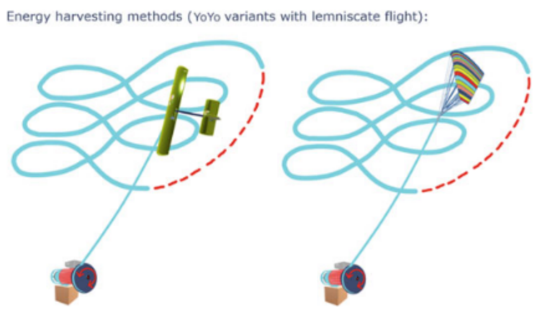

Figure 2.3: YoYo flight concept with lemniscate path [5]

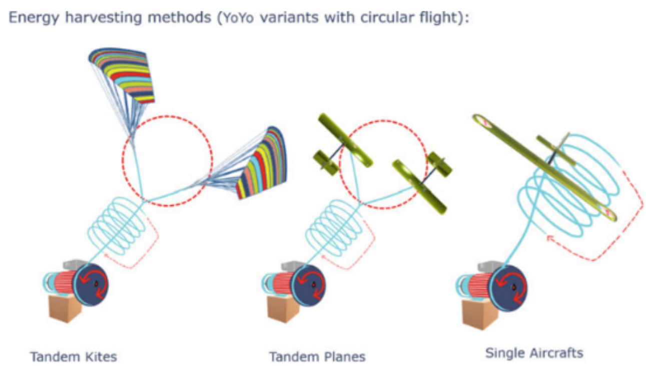

Figure 2.4: YoYo flight concept with circular path [5]

The second approach is the flying generator, which in this operation, generators are equipped with propellers and mounted on aircraft. These are controlled by Airborne Wind power so that the propellers provide torque to generate electricity [5]. The primary concept involves elevating generators aloft and transmitting the generated electricity to the ground via cables in the tethers. The most common approach employs airfoils equipped with generators and propellers. During production mode, the propellers function either in push or pull mode, depending on their placement, with some mounted on the back [5]. An example can be shown in Figure 2.5. The cable connection not only facilitates power transmission but also enables the generators to function as engines, facilitating fully automated take-offs and landings. This innovative design allows for a unique integration of aerial generators capable of both energy production and autonomous flight operations [5].

The third approach is ship or generator propulsion, which uses the lift force to pull ships or movable generators (e.g. electric locomotives) with the resulting horizontal force [5].

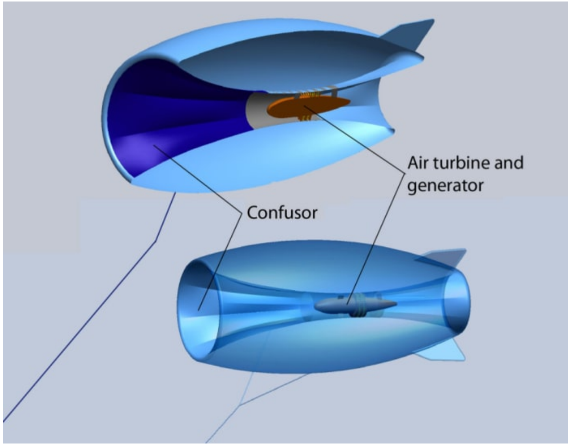

Figure 2.5: Example of a flying generator [5]

2.4 Competitors of the UPWIND project

There are several competitors of the UPWIND project in the airborne wind energy sector. Here are some competitors or alternative projects:

- **EnerKite**: EnerKite is a German company developing tethered flying devices to harness wind energy. Their system uses a kite-like structure equipped with turbines to generate electricity. They focus on efficient energy capture and ease of deployment.

- **Makani**: Makani, previously a project under Alphabet (Google's parent company), was aimed at generating electricity using a kite-like structure equipped with turbines. While the project was discontinued in early 2020, its approach to airborne wind energy shared similarities with EnerKite's concept of using tethered flying devices to capture wind energy.

- **Kitenergy**: An Italian startup, Kitenergy, develops kite-based wind energy systems. They aim to create scalable and modular systems that generate electricity through the motion of tethered kites flying in loops.

- **Kitepower**: Kitepower, based in the Netherlands, specialises in airborne wind energy systems. They design and develop high-altitude kite systems capable of producing renewable energy by capturing wind at higher altitudes.

- **Ampyx Power**: Ampyx Power, headquartered in the Netherlands, works on airborne wind energy using tethered aircraft. Their system involves autonomous aircraft that fly in patterns to generate electricity.

- **SkySails Power**: SkySails Power, a German company, focuses on airborne wind energy using large-scale kites. They aim to produce renewable energy by exploiting high-altitude winds.

- **Altaeros**: Altaeros, a US-based company, works on an airborne wind turbine called the Buoyant Airborne Turbine (BAT). The BAT is a helium-filled, inflatable wind turbine that operates at high altitudes to harness strong winds.
- **Kitemill**: Kitemill, a Norwegian company, develops airborne wind energy solutions using tethered kites. They aim to create cost-effective systems for wind energy production.
- **TwingTec**: TwingTec, based in Switzerland, designs airborne wind energy systems using tethered drones. Their approach involves drones flying in a figure-eight pattern to generate electricity.

2.5 Summary

In summary, AWES represent an innovative and promising approach to harnessing wind power for electricity generation. These systems operate by utilizing flying devices or tethered wings at high altitudes, where wind speeds are stronger and more consistent compared to ground-level turbines.

The operation of AWES involves deploying aerodynamic devices that capture wind energy, generating electricity through various methods such as tethered kites, drones, or autonomous aircraft. This unique approach allows for the exploitation of abundant wind resources at higher altitudes, offering several advantages over traditional wind energy systems.

Competitors in the AWES sector, including companies like Makani, Ampyx Power, Kitepower, SkySails Power, TwingTec, and Kitemill, are exploring different technological solutions to optimize energy capture, improve efficiency, and reduce costs. These competitors often focus on innovative designs, control systems, and materials to gain a competitive edge in the rapidly evolving field of airborne wind energy.

Chapter 3

State of the art on Bidirectional Converters

3.1 Introduction

In the UPWIND project, the generator is connected to a DC bus through a bidirectional DC/AC converter, which in turn is connected to batteries and braking resistors through DC/DC converters and is connected to the single-phase grid through a bidirectional DC/AC converter. This can be seen in the diagram in Figure 3.1. The focus of this dissertation will be on the converter connecting the DC bus and the single-phase grid. The grid will have 230 V, 50 Hz with a maximum power of 3680 VA.

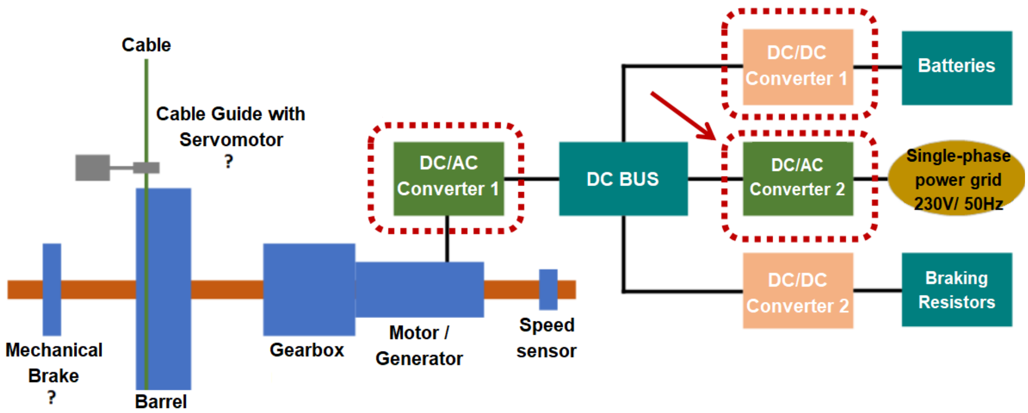

Figure 3.1: Diagram of the Stationary generator and its connections

In this chapter, it will tell about the converter's topologies and control strategies.

3.2 Topology

The converter will be voltage-sourced. There are two main circuits for the converter, the half-bridge and full-bridge circuits. The half-bridge circuit also called a two-level converter generates bipolar voltages, with $-\frac{V_{DC}}{2}$ and $+\frac{V_{DC}}{2}$ the only possible outputs (as shown in Figure 3.2). Meanwhile, the full-bridge generates a monopolar voltage (0 to $-V_{DC}$ or 0 to V_{DC}, shown in Figure 3.2), giving full supply to the load and gives better control to the sistem. Furthermore, the full-bridge permits the current to flow both ways of the converter, while the half-bridge is unidirectional.

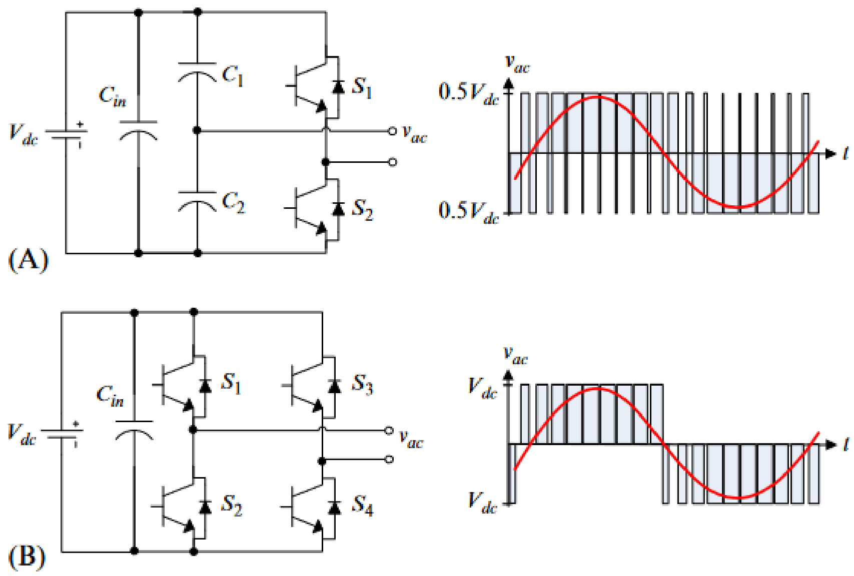

Figure 3.2: Half-bridge (A) and full-bridge (B) topology with their AC output voltage. [6].

3.3 Control

3.3.1 Control Targets

Control strategies for converters must address fundamental requirements to ensure safe and efficient operation [6]. These essential considerations, widely acknowledged in converter design (see [7]), encompass the following key targets:

- **Limited or constant switching frequency:** Managing the switching frequency offers benefits in terms of identifiable power losses, aiding hardware efficiency, and effective thermal dissipation [6]. Additionally, maintaining a consistent current and/or voltage spectrum simplifies interface filter design [6].

- **Reduced ripple:** Minimizing ripple assists in downsizing passive components (like capacitors and inductors) within the converter [6].

- **High dynamic response:** Given converters' integration into larger systems like electric vehicles or renewable power plants, a swift adjustment in power flow is crucial to meet evolving demands [6].

- **No Phase and Amplitude Error in AC-Systems' Steady State:** Controllers are designed to track steady references, crucial for regulation [6]. In AC systems, maintaining precise sinusoidal references is vital to prevent undesired effects, like the injection or absorption of reactive power in converters like unity power factor rectifiers [6].

- **Reduced harmonic content:** Preferably, in AC or DC applications, controlled currents or voltages should ideally exhibit the desired fundamental frequency or a minimal harmonic content for DC components, ensuring optimal operation [6]. High harmonic levels can induce losses in electric motors (e.g., in electrical drives) or provoke unwanted grid resonances in grid-connected applications [6].

It's important to note that some requirements may conflict, such as a high dynamic range conflicting with reduced harmonic content. Therefore, selecting appropriate controller classes becomes crucial to manage these interdependencies while striving to meet these targets.

3.3.2 Control Classification

Three different control classes are identified based on how the control input is chosen. The first class (Figure 3.3A) is the classic linear approach employing a modulator [6]. Here, the controller tracks the converter output (e.g., current, voltage, power) and provides an control input, u [6]. As this average input cannot be directly applied, it's synthesized through a modulation stage, usually generating the necessary duty cycle, u = d, to control the average output, y [6]. Operating within a continuous control set (CCS), for instance, $d \in [0, 1]$, this method commonly employs an average model of the converter and load while neglecting the modulator's effect [6]. The advantage lies in fixing the converter's switching frequency and defining a clear spectrum across controlled variables, thus accommodating various control objectives [6].

The second control class (Figure 3.3B) directly utilizes the state of switches or output voltage levels as the input, $u = S_w$, eliminating the need for a modulation stage [6]. As the control input has fixed states, falling into a finite control set (FCS) like $S_w \in 0, 1$, this approach allows designers to use instantaneous models of the converter and load for faster dynamic responses [6]. However, it results in output variables displaying a spread spectrum [6].

The third control class (Figure 3.3C) incorporates the modulator into its strategy alongside an instantaneous model of the converter and load [6]. Here, the instants when switches must commutate, t_{S_w}, within a sampling time, T_s, serve as a control input, $u = t_{S_w}$, also falling within a CCS, e.g., $t_{S_w} \in [0, T_s]$ [6]. This method achieves rapid dynamics during transients with a fixed switching frequency and a well-defined spectrum [6].

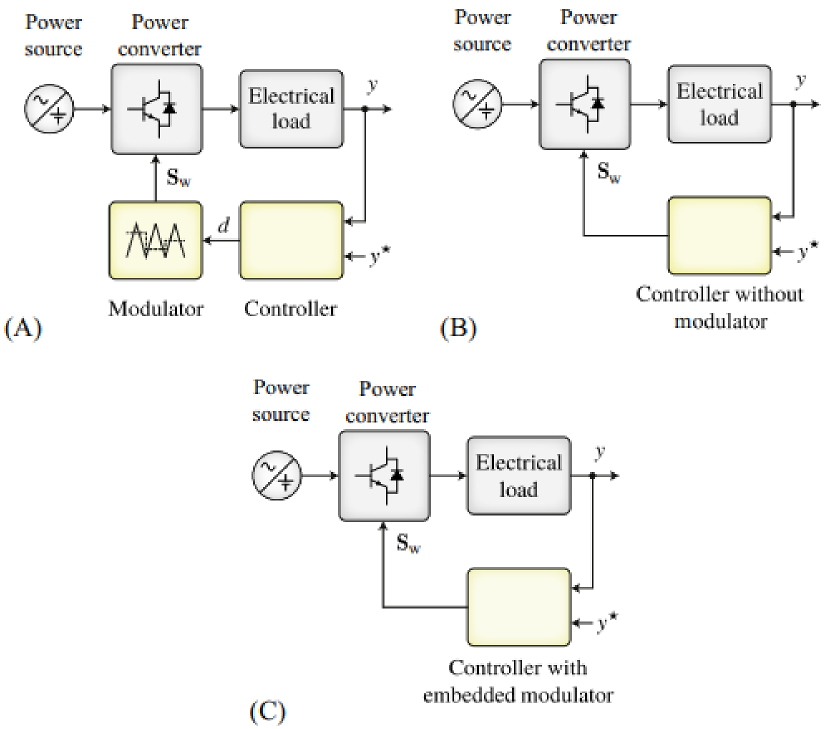

Figure 3.3: Classification of control strategies: (A) modulation-base controllers,(B) controllers without a modulator, and (C) controllers with embedded modulator [6].

3.3.3 Modulation Methods

The modulator's pivotal role in governing converters, irrespective of their type (DC/DC, DC/AC, or AC/DC), involves decoding the controller's effort (d in Figure 3.4A) and converting it into switching signals (S_w in Figure 3.4A) that propel the power semiconductors [6].

The specifications of modulators' output greatly hinge upon the specific application. For low-power scenarios, analogue modulators capable of handling several kilohertz in switching signal frequency are typically sought to reduce converter weight and size by elevating the switching frequency. Conversely, high-power applications like DC/AC or AC/DC converters necessitate digital modulators functioning at lower frequencies (less than kilohertz), capable of managing multiple outputs and often featuring enhanced sophistication [6].

Pulse-width modulation (PWM) stands as the most prevalent technique for implementing modulators in DC/DC, DC/AC, and AC/DC converters, persisting for a long time. Illustrated in Figure 3.4, PWM governs the switched waveform by modifying the pulse width as per the controller's effort, d [8, 9]. PWM implementation can be either in continuous time using analogue signals or in discrete time as part of an analogue-to-digital process [6].

The evolution of power electronics in recent years has brought forth new challenges in modulation, such as computational demands, feasibility, and optimal harmonic distortion, among others [6]. With the ongoing development of new converter topologies and applications, these challenges

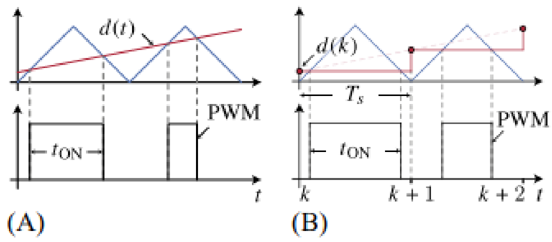

Figure 3.4: Basic concept of modulation: (A) analogue PWM and (B) digital PWM [6].

continue to evolve. As a response, adaptations and refinements to classic PWM and other modulation methods have been introduced [6].

3.3.3.1 Conventional PWM Techniques

Voltage source inverters necessitate a modulator to generate a PWM voltage mirroring the harmonic components akin to the controller's effort while maximizing the utilization of the DC voltage [6]. As the controller's effort waveform typically assumes a sinusoidal shape, the PWM waveform should exhibit harmonics with a fundamental frequency component aligning with the desired controller's effort waveform [6]. Here are some of PMW techniques:

- **Square-wave modulation method:** The initial method to produce a PWM waveform from a sinusoidal waveform, while foundational, often yields significant distortion in the low-order harmonics of the resulting waveforms, as depicted in Figure 3.5 [6]. Consequently, this approach sees limited practical application. PWM-based methods offer a viable alternative to enhance the performance of output waveforms.

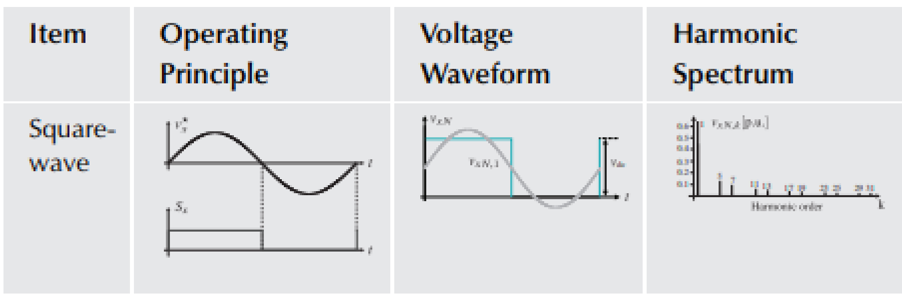

Figure 3.5: Square-wave modulation method for Two-Level Voltage Source Inverters [6].

- **Carrier-Based PWM Techniques - Bipolar and Unipolar PWM for Single-Phase Converter:** In the circuit diagram shown in Figure 3.6, a single-phase VSI is depicted. This inverter is commonly employed to convert a constant DC input voltage, v_{dc}, into an AC output voltage, v_{AB}, which can exhibit a variable amplitude and frequency [6]. The fundamental principle underlying the operation of the PWM for this inverter is elucidated in Figure 3.7 [6]. The gating signals,

S_1 and S_2, are generated by comparing a sinusoidal modulating waveform, v_{mA}, with a periodic triangular carrier waveform, v_{cr} [6]. This approach is often termed Sinusoidal PWM (SPWM) owing to the sinusoidal nature of the modulating waveform.

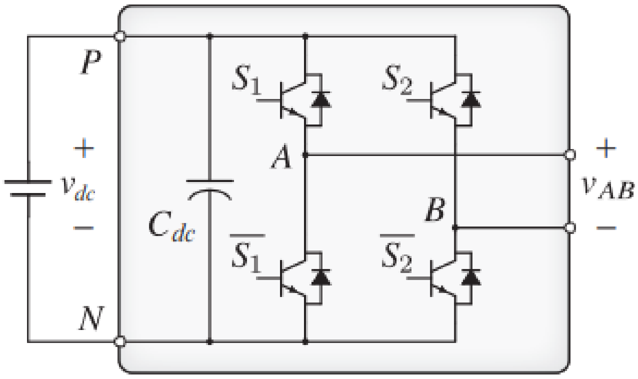

Figure 3.6: Example of a single-phase full-bridge inverter [6].

As a first option, the two gating signals can be complementary to each other, resulting in a bipolar voltage waveform [6]. Consequently, the inverter output voltage v_{AB} alternates between $+v_{dc}$ and $-v_{dc}$, as depicted in Figure 3.7. This modulation technique is referred to as bipolar modulation [10]. The power switches' switching frequency (f_{sw}) is then equal to the carrier frequency (f_{cr}) [6].

Alternatively, the equivalent switching frequency in v_{AB} can be doubled by maintaining the same power switches' switching frequency through the utilization of unipolar PWM [6]. Here, an additional modulating wave, v_{mB}, 180 degrees out of phase with v_{mA}, is required [6]. Gating signals S_1 and S_2 are generated by comparing v_{mA} and v_{mB} with the carrier wave v_{cr} [6]. Consequently, the converter output voltage v_{AB} switches either between 0 and $+v_{dc}$ during the positive half-cycle or between 0 and $-v_{dc}$ during the negative half-cycle of the fundamental frequency, as outlined in Figure 3.7 [10].

Under unipolar modulation, switches in phases A and B do not switch simultaneously, unlike bipolar modulation where all four switches are commutated simultaneously [6]. Despite the equivalent output fundamental amplitude and power switches' switching frequencies match the carrier frequency, the converter switching frequency is effectively doubled under unipolar modulation (i.e., $f_{sw,inv} = 2 * f_{sw}$) [6]. This feature facilitates potential size and cost reduction of converter output filters if employed [6].

The modulation index (m_a), defined as the ratio between the peak values of the modulating and carrier waves, can be adjusted to influence the fundamental-frequency component $v_{AB,1}$ in the converter output voltage [6] using the formula:

$$m_a = \frac{\hat{v}_m}{\hat{v}_{cr}} \tag{3.1}$$

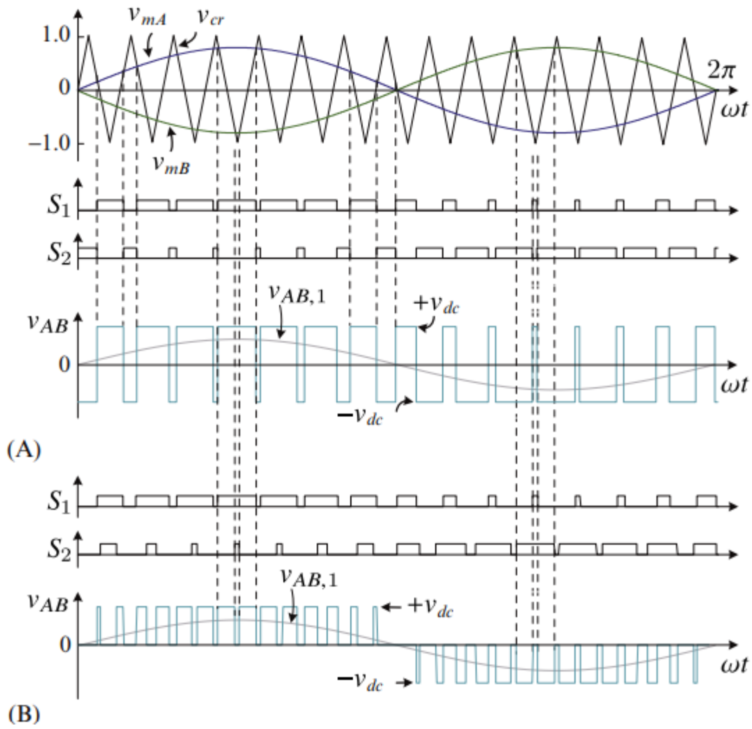

Figure 3.7: Bipolar and unipolar PWM for a single-phase inverter: (A) bipolar and (B) unipolar [6].

The modulation index m_a is typically adjusted by varying $\hat{v}_m$ while maintaining $\hat{v}_{cr}$ constant [6]. Additionally, the frequency modulation index (m_f) is defined as the ratio between the frequencies of the carrier and modulating waves [6], given by:

$$m_f = \frac{f_{cr}}{f_m} \tag{3.2}$$

When the modulation frequency (f_m) synchronizes with the carrier wave and the modulation index (m_f) is an integer, the modulation scheme is identified as synchronous PWM [6]. Conversely, if m_f is not an integer, the scheme is termed asynchronous PWM [6]. In the latter case, the carrier frequency (f_{cr}) is typically fixed and independent of f_m [6]. Asynchronous PWM, often implemented with analogue circuits, features a fixed switching frequency. However, its output spectrum encompasses non-characteristic harmonics whose frequency is not a multiple of f_m [6]. Conversely, synchronous PWM, more conducive to implementation with a digital processor, offers distinct advantages.

3.3.4 Control of Converters - PWM-Based Linear Control

The prevalent control structure for linear systems like converters often employs the linear feedback control loop, illustrated in Figure 3.8A [6]. This loop aims to minimize the tracking error ($e = r - y$)

by applying a control input (u) to the system (G(s)) using a feedback controller (C(s)) [6]. However, disturbances that may arise can affect the closed-loop performance [6]. Variations between nominal ($\bar{y}$) and actual (y) system outputs may occur due to measurement noise or uncertainties (denoted by η_o), and deviations may occur between nominal input ($\bar{u}$) from the controller and the actual input due to external factors (denoted by η_i) [6]. Therefore, designing a feedback controller must consider both reference tracking error performance and disturbance rejection capability [6].

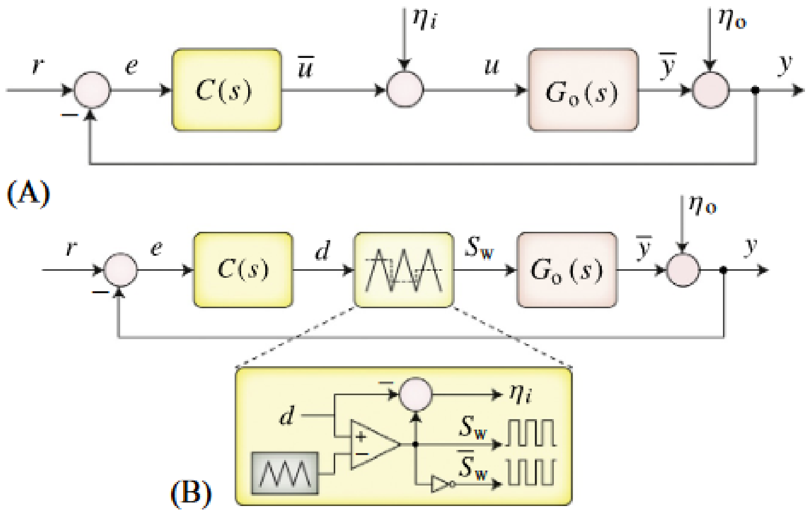

Figure 3.8: Linear feedback controller: (A) a general closed-loop representation and (B) closed-loop including modulator [6].

The input-to-output relationship for the closed loop depicted in Figure 3.8A can be expressed as:

$$y(s) = T(s)r(s) + S(s)d_o(S) + S_i(s)d_i(S) \tag{3.3}$$

Here, T(s) represents the reference-to-output transfer function that determines the reference tracking error performance [6]. S(s) and $S_i(s)$ are sensitivity transfer functions governing disturbance rejection, given by:

$$T(s) = \frac{C(s)G_o(s)}{1 + C(s)G_o(s)} \tag{3.4}$$

$$S(s) = \frac{1}{1 + C(s)G_o(s)} \tag{3.5}$$

$$S_i(s) = G_o(s)S(s) \tag{3.6}$$

Note that T(s) and S(s) are complementary (i.e., T(s) + S(s) = 1). For optimal reference tracking and effective disturbance rejection, ideally, $T(s) \simeq 1$ and $S(s) \simeq 0$ are sought [6]. The controller C(s), as per equations (3.4) and (3.5), influences both reference tracking and disturbance rejection performances [6]. However, achieving these control targets across the entire frequency spectrum separately is often unfeasible [6]. Yet, for specific frequency ranges, this ideal condition might be achievable [6].

In the realm of converter control, a linear controller typically generates a duty cycle, d, which must be synthesized by a modulator (Figure 3.8B) [6]. As explained in Section 3.3.3, the modulator maintains a constant switching frequency with a well-defined spectrum in the steady state. However, the actual input applied to the system ($u = S_w$), represented by the state of power switches, differs from the nominal input provided by the controller ($\bar{u} = d$) [6]. This discrepancy can be viewed as an input disturbance, $\eta_i = S_w - d$ [6]. Under high bandwidth closed loops, this input disturbance may impact tracking performance, as the controller attempts to compensate for modulation noise [6]. In analogue implementations, this can lead to additional commutations, resulting in increased power losses and harmonic distortion. Conversely, digital implementations often synchronize controller sampling with the PWM carrier, limiting the closed-loop bandwidth to the PWM frequency [6]. Consequently, system output measurements (current, power, torque, etc.) mimic their average values, allowing the use of average converter and load models (i.e., G(s)) for designing a linear feedback controller.

3.3.4.1 PI Controller

The Proportional-Integral (PI) controller remains the most commonly used linear controller. Its continuous-time expression is:

$$u(t) = K_p e(t) + K_i \int e(t)dt \tag{3.7}$$

In the frequency domain, the equivalent representation of a PI controller is:

$$C_{PI}(s) = K_p + \frac{K_i}{s} = K_p(\frac{1 + sT_i}{sT_i}) = K_p(1 + \frac{\tau_i}{s}) \tag{3.8}$$

where $Ti = K_p/K_i$ and $\tau_i = 1/T_i$. Figure 3.9 portrays two standard implementations of this conventional controller based on equation (3.8).

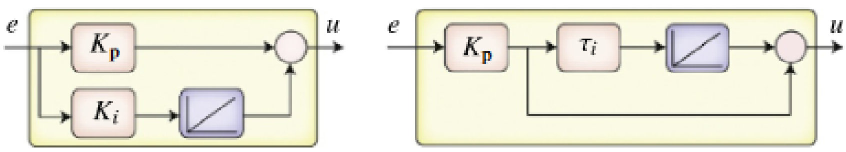

Figure 3.9: Standard PI controller structures [6].

Determining appropriate values for K_p and T_i is crucial to achieving the desired closed-loop performance, particularly when dealing with first-order systems.

Design Criteria of PI Controllers for First-Order Systems

In certain scenarios, control of converters and electrical drives can be achieved by considering one or more first-order systems. For instance, the AC current of a rectifier connected to the grid through an inductor and its DC-link can be modelled as two cascaded first-order systems [6]. Similar situations occur in systems like the speed and current dynamics of induction motors under a field-oriented control strategy [6]. This section aims to provide a comprehensive analysis and design approach for a PI controller applicable to first-order systems. Given a plant modelled as:

$$G_o(s) = \frac{K_o}{\tau_o s + 1} \tag{3.9}$$

the closed-loop transfer function for a first-order system governed by a PI controller, based on equation (3.4), can be expressed as:

$$T(s) = \frac{\frac{K_o K_p}{\tau_o T_i}(T_i s + 1)}{s^2 + (\frac{1+K_o K_p}{\tau_o})s + \frac{K_o K_p}{\tau_o T_i}} \tag{3.10}$$

This closed-loop transfer function yields a second-order system with one zero. The selection of poles for the closed-loop system referred to as pole placement, can be accomplished by setting the controller parameters K_p and T_i. Simplifying the closed-loop characteristic equation as:

$$s^2 + 2\zeta\omega_n s + w_n^2 \tag{3.11}$$

where ζ represents the relative damping and ω_n is its natural frequency. The resulting closed-loop poles are given by:

$$p_{1,2} = -\zeta\omega_n \pm \omega_n \sqrt{\zeta^2 - 1} \tag{3.12}$$

while the closed-loop time constant is defined as:

$$\tau_D = \frac{1}{\zeta\omega_n} \tag{3.13}$$

Thus, instead of determining the controller parameters K_p and T_i, closed-loop poles can be set by choosing ζ and ω_n. By comparing equation (3.11) with equation (3.10), the relationship between ω_n and ζ can be established as follows:

$$\omega_n^2 = \frac{K_o K_p}{\tau_o T_i} \tag{3.14}$$

$$\zeta = \frac{1 + K_o K_p}{2\omega_n \tau_o} \tag{3.15}$$

Therefore, the PI tuning parameters K_p and T_i are determined by:

$$T_i = \frac{2\zeta\omega_n\tau_o - 1}{\omega_n^2\tau_o} = \frac{2\zeta}{\omega_n} - \frac{1}{\omega_n^2\tau_o} \tag{3.16}$$

$$K_p = \frac{2\zeta\omega_n\tau_o - 1}{K_o} = \frac{\omega_n^2\tau_o}{K_o}T_i \tag{3.17}$$

The closed-loop bandwidth of T(s) in equation (3.10) is indicated as:

$$\omega_{BW} = \mu * \omega_n \tag{3.18}$$

where

$$\mu = \sqrt{1 + 2\zeta^2 + \sqrt{4\zeta^4 + 4\zeta^2 + 2}} \tag{3.19}$$

To achieve the desired closed-loop performance, typically a damping factor ζ of 0.707 or higher is selected [6]. Moreover, to ensure positive PI parameters, the natural frequency ω_n should be greater than $\frac{1}{2\zeta\tau_o}$ [6]. Nevertheless, increasing ω_n leads to faster controller response according to equation (3.16). Consequently, from equation (3.16), it can be deduced that for large ω_n values:

$$T_i \simeq \frac{2\zeta}{\omega_n} \tag{3.20}$$

This implies that T_i remains unaffected by changes in system parameters, rendering the controller more resilient to uncertainties in those parameters. However, in analogue implementations, it's important to maintain the closed-loop bandwidth $f_{BW} = \omega_{BW}/(2\pi)$ below half the PWM frequency f_{cr} to prevent the PI controller from compensating for modulation errors beyond this limit, leading to additional switch commutations [6]. Hence, for analogue implementations, the range for ω_n is recommended as:

$$\frac{1}{2\zeta\tau_o} < \omega_n \leq \frac{\pi}{\mu}f_{cr} \tag{3.21}$$

Lastly, the reference-to-input and sensitivity transfer functions in terms of ζ and ω_n are given as:

$$T(s) = \frac{(2\zeta\omega_n - \frac{1}{\tau_o})s + \omega_n^2}{s^2 + 2\zeta\omega_n s + \omega_n^2} \tag{3.22}$$

$$S(s) = \frac{s(s + \frac{1}{\tau_o})}{s^2 + 2\zeta\omega_n s + \omega_n^2} \tag{3.23}$$

These transfer functions indicate $T(0) = 1$ and $S(0) = 0$ when $s = 0$, illustrating the PI controller's capability to precisely track constant references and resist steady disturbances. Note that both T(s) and S(s) share identical poles, meaning the tuning of the PI controller affects both aspects of these characteristics.

Anti-windup Scheme

In power electronics applications, the actuators have their limits, notably the modulator's duty cycle constraint. When the controller output surpasses this actuator limit, the integral action can accumulate to a significant value [6]. Upon the input's return to the linear zone, a substantial transient occurs, termed as "wind-up" [6]. To prevent adverse closed-loop behaviours that could potentially damage a converter or electrical drive, mitigating measures against the detrimental effects of wind-up are crucial [6]. Among the simplest anti-windup schemes is the back-calculation method, illustrated in Figure 3.10. This scheme is easily implementable in the analogue form. Initially, the saturation effect is considered by incorporating the saturation error:

$$e_{sat}(t) = u(t) - v(t) = sat(v(t)) - v(t) \tag{3.24}$$

This error is then utilized to offset the integral action. Importantly, this anti-windup scheme doesn't impact the controller output, u(t), as long as the unsaturated PI output, v(t), remains within the linear range (i.e., e(t) = 0) [6].

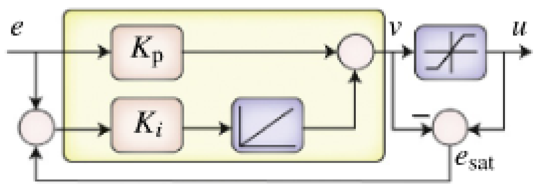

Figure 3.10: PI controller with anti-windup strategy [6].

While, as previously noted, the PI controller excels at tracking constant references, it poses challenges in tracking sinusoidal references, particularly in inverters. Therefore, the subsequent section will delve into designing linear AC compensators to specifically tackle this significant issue.

3.3.4.2 Resonant Controller

To control converters, one commonly used solution is to operate in a synchronous $d-q$ frame. This approach converts the sinusoidal tracking problem into a regulation problem with a constant reference. Another method is to transform the PI controller, $C_{PI}(s)$, as shown in equation (3.8), into an AC compensator that operates at a frequency of ω_o [6]. This type of controller is also called a resonant controller, or $C_{RE}(s)$ [11]. By doing this, the controller can work in a stationary frame without requiring any transformations. To achieve this, the integral action is replaced with the following transformation:

$$\frac{1}{s} \rightsquigarrow \frac{2s}{s^2+\omega_o^2} \tag{3.25}$$

As such, the resonant controller can be represented as:

$$C_{RE}(s) = K_p + \frac{2K_i s}{s^2 + \omega_o^2} \tag{3.26}$$

Finally, the reference-to-input and sensitivity transfer functions can be expressed in the following way:

$$T(s) = \frac{K_p K_o s^2 + 2K_i K_o s + K_p K_o \omega_o^2}{(s^2 + \omega_o^2)(\tau_o s + 1) + K_p K_o s^2 + 2K_i K_o s + K_p K_o \omega_o^2} \tag{3.27}$$

$$S(s) = \frac{(s^2 + \omega_o^2)(\tau_o s + 1)}{(s^2 + \omega_o^2)(\tau_o s + 1) + K_p K_o s^2 + 2K_i K_o s + K_p K_o \omega_o^2} \tag{3.28}$$

In this scenario, it can be concluded that for $s = j\omega_o$, $T(j\omega_o) = 1$, and $S(j\omega_o) = 0$. This means that the resonant controller, $C_{RE}(s)$ in equation (3.26), can precisely track and reject sinusoidal references and disturbances with frequency ω_o.

If you want to create a resonant controller for a plant that can be represented as a first-order system, you can use the same design approach as you would for a PI controller. However, it's crucial to remember that a damping factor lower than one may lead to undesirable oscillations that can have a negative impact on the closed-loop performance. Hence, it is advisable to opt for $\zeta \geq 1$ in this scenario [6].

3.3.4.3 Digital Implementation of PI and Resonant Controllers

Presently, digital controllers dominate converter control due to the reduced cost of digital platforms coupled with their increased computing power and speed [12]. Digital controllers offer enhanced flexibility compared to analogue versions and can incorporate additional functionalities like maximum power point tracking algorithms, faster and more accurate Phase-Locked Loops (PLLs), sensorless drive strategies, and more, within the same digital platform [6].

Figure 3.11 illustrates a standard digital implementation of a PWM-based linear controller within a digital platform. Analogue measurements undergo conversion to digital form via an Analog-to-Digital Converter (ADC) and typically pass through a low-pass filter to mitigate high-frequency noise [6]. Field Programmable Gate Arrays (FPGAs) and Digital Signal Processors (DSPs) stand out as the most popular digital platforms for converters. In some cases, a hybrid approach involving both FPGA for handling peripherals (ADCs and modulators) and DSP for controller implementation is employed [6].

In digital implementations, the PWM stage holds significant importance as it not only generates controller actuation but also synchronizes the entire digital process, encompassing measurements, execution of control algorithms, and actuation. The sampling time, denoted as T_s, is directly linked to the PWM carrier period, T_{cr}, as depicted in Figure 3.12.

When an asymmetric carrier is utilized, both the PWM and the controller operate at the same sampling frequency, as illustrated in Figure 3.12A [6]. Conversely, symmetric carriers can adjust the sampling frequency. For instance, with a single update mode (as depicted in Figure 3.12B), the sampling frequency mirrors the PWM frequency, resulting in $f_s = f_{cr}$ [6]. However, in a double

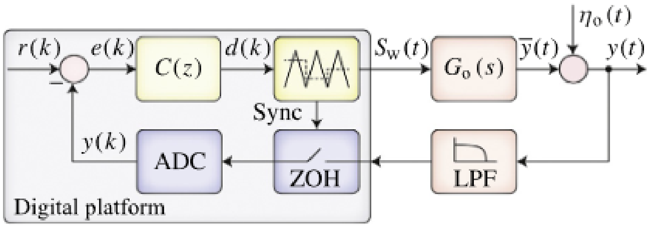

Figure 3.11: Digital implementation of a PWM-based linear controller [6].

update mode (sampling at both edges of the triangular carrier), the sampling frequency becomes double the carrier frequency, establishing $f_s = 2f_{cr}$, as shown in Figure 3.12C [6]. Importantly, the duty cycles (d(k)) remain constant throughout the sampling time, ensuring that no additional commutations occur [6].

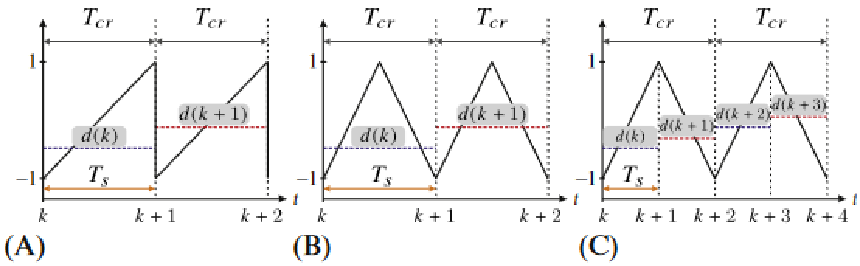

Figure 3.12: PWM-based sampling synchronization: (A) asymmetric PWM, $f_s = f_{cr}$; (B) single update symmetric PWM, $f_s = f_{cr}$; and (C) double update symmetric PWM, $f_s = 2f_{cr}$ [6].

Designing a linear controller directly in discrete time is feasible [13]. However, the continuous-time plant model, G(s), must be transformed into an equivalent discrete-time plant, or the controller can be initially designed in the s-domain (C(s)), which is then transformed into an equivalent controller in the z-domain, obtaining C(z) [6].

Opting for the latter choice, it capitalizes on the continuous-time design previously delineated. As such, by applying a zero-order hold approximation to equation (3.8), the continuous-time PI controller, $C_{PI}(s)$, can be converted into discrete-time, yielding:

$$C_{PI}(z) = \frac{K_a z + K_b}{z-1} = \frac{K_a + K_b z^{-1}}{1-z^{-1}} \tag{3.29}$$

where

$$K_a = K_p, \, and \, K_b = K_i T_s - K_p \tag{3.30}$$

Likewise, the discrete-time polynomial equation:

$$u(k) = K_a e(k) + K_b e(k-1) + u(k-1) \tag{3.31}$$

implements the PI controller at each sampling instant k. Similarly, the continuous-time resonant controller, $C_{RE}(s)$ in equation (3.26), approximates a discrete-time equivalent:

$$C_{RE}(z) = \frac{a_0 z^2 + a_1 z + a_2}{z^2 - b_1 z + 1} = \frac{a_0 + a_1 z^{-1} + a_2 z^{-2}}{1 - b_1 z^{-1} + z^{-2}} \tag{3.32}$$

where

$$\begin{aligned} a_0 &= K_p \\ a_1 &= 2(\frac{K_i}{\omega_o}\sin\omega_o T_s - K_p \cos\omega_o T_s) \\ a_2 &= K_p - \frac{2K_i}{\omega_o}\sin\omega_o T_s \\ b1 &= 2\cos\omega_o T_s \end{aligned} \tag{3.33}$$

The discrete-time polynomial equation:

$$u(k) = a_0 e(k) + a_1 e(k-1) + a_2 e(k-2) + b_1 u(k-1) - u(k-2) \tag{3.34}$$

implements the resonant controller at each sampling instant k. Both discretizations are dependent on the sampling time, T_s, derived from the PWM carrier period, T_{cr}. For a strong correlation between continuous-time controller C(s) and its discrete-time equivalent C(z), the Nyquist criterion stipulates the sampling frequency, $f_s = \frac{1}{T_s}$, should exceed the closed-loop time constant, τ_D in equation (3.13) [6]:

$$T_s \leq \frac{\tau_D}{2} = \frac{1}{2\zeta\omega_n} \tag{3.35}$$

Thus, the range of values for ω_n in equation (3.21) is substituted by:

$$\frac{1}{2\zeta\tau_o} < \omega_n \leq \frac{f_s}{2\zeta} \tag{3.36}$$

Finally, digital implementation of both PI and resonant controllers in a DSP or FPGA can be achieved following the algorithms depicted in Figure 3.13 and Figure 3.14, respectively [6]. It's important to note that a digital anti-windup scheme is incorporated for both cases. Assumedly, the control input is constrained within the range of -1 to 1; if the carrier operates within a different range, adjustments to these limits will be necessary.

3.3.5 Control of Converters - Without Modulator

Control strategies for converters that operate without a modulator involve direct generation of the converter's gate signals by the controller. These controllers aim to minimize the instantaneous error between control references and variables, striving to achieve specific control objectives. While enhancing transient operation, these methods can result in variable switching frequency due to the coupling of fundamental and harmonic components of the control variables [6]. Here, we'll explore closed-loop control methods that don't rely on an external modulator.

```
ALGORITHM — Digital PI Controller C_PI(z)
Initialization at k = 0 : e(k − 1) ← 0, u(k − 1) ← 0
    function u(k) = PI(r, y(k), K_a, K_b)
      e(k) ← r − y(k)
      u(k) ← K_a e(k) + K_b e(k − 1) + u(k − 1)
      if −1 ≤ u(k) ≤ 1 then                          ▷ Antiwindup
        u(k) ← ±1                                     ▷ Saturation
      end if
      Memory: e(k − 1) ← e(k), u(k − 1) ← u(k)
    end function
```

Figure 3.13: Algorithm for Digital PI Controller $C_{PI}(z)$ [6].

```
ALGORITHM — Digital Resonant Controller C_RE(z)
Initialization at k = 0 : e(k − 1) ← 0, e(k − 2) ← 0
                          u(k − 1) ← 0, u(k − 2) ← 0
    function u(k) = RE(r, y(k), a_0, a_1. a_2, b_1)
      e(k) ← r − y(k)
      u(k) ← a_0 e(k) + a_1 e(k − 1) + a_2 e(k − 2) + b_1 u(k − 1) − u(k − 2)

      if −1 ≤ u(k) ≤ 1 then                          ▷ Antiwindup
          u(k) ← ±1
          e(k) ← 0
          e(k − 1) ← 0
      end if
      Memory:  e(k − 2) ← e(k − 1), e(k − 1) ← e(k)
               u(k − 2) ← u(k − 1), u(k − 1) ← u(k)
    end function
```

Figure 3.14: Algorithm for Digital Resonant Controller $C_{RE}(z)$ [6].

3.3.5.1 Hysteresis

Hysteresis control methods, implemented in an analogue or digital form, entail significant changes in the controller's output (S_w) whenever the error between control references and variables crosses the boundaries of positive or negative hysteresis bands (Figure 3.15) [6]. This rapid response characteristic leads to high-gain behaviour, enabling quick adjustment to deviations from control references [6]. However, in digital implementations, such as shown in Figure 3.16B, the control variable ripples might not consistently stay within the specified hysteresis band limits [6]. This discrepancy is highlighted in the zoomed view within Figure 3.16A. Consequently, the operation of digital hysteresis controllers often differs from their analogue counterparts.

3.3.5.2 Direct Torque Control/Direct Power Control

Direct Torque Control (DTC) is a widely embraced motor drive control system renowned for its simplicity, rapid response, and robust performance across industry and academia [15]. This system employs hysteresis controllers to trace torque and flux references [6]. It operates with a switching table, facilitated by look-up tables (LUT), to determine the optimal converter output [6]. The operational principle of DTC is depicted in Figure 3.17A, while its block diagram is represented in Figure 3.17B.

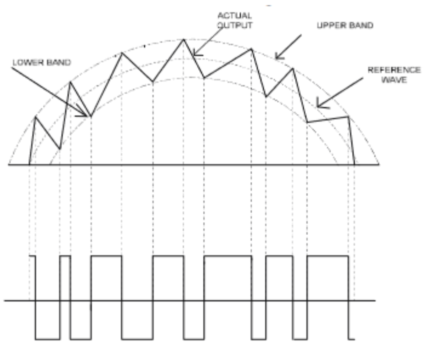

Figure 3.15: Hysteresis operation principle [14].

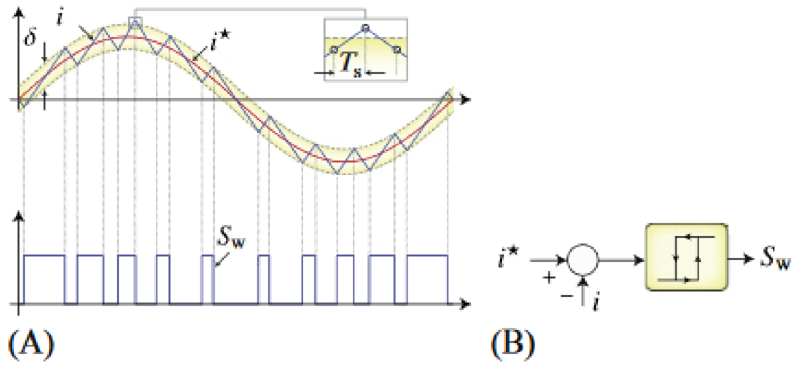

Figure 3.16: A digital implementation of hysteresis control: (A) operation principle and (B) block diagram [6].

Similarly, Direct Power Control (DPC), was developed specifically for grid-connected applications, DPC is akin to DTC in its approach but diverges in its focus on controlling instantaneous active and reactive power [6]. Rather than referencing torque and flux, DPC uses the instantaneous errors of active and reactive power to determine the optimal converter switching state [16]. Figure 3.18 portrays the block diagram illustrating the functioning of DPC.

For this work, the DTC isn't important since motors will not be dealt with.

3.3.5.3 FCS Model Predictive Control

FCS Model Predictive Control (FCS-MPC) stands as a nonlinear control strategy employed to enhance control performance, specifically targeting transient conditions across a converter's complete operational spectrum [6]. This approach necessitates a system model for predicting future behaviour in variables of interest (y) and a defined cost function outlining desired control objectives. The system model predicts variable values within a finite prediction horizon during each sampling interval. An optimization algorithm then tackles the optimal control problem defined by the cost function [6].

The cost function (J(k)) spanning the finite prediction horizon (N) is expressed as:

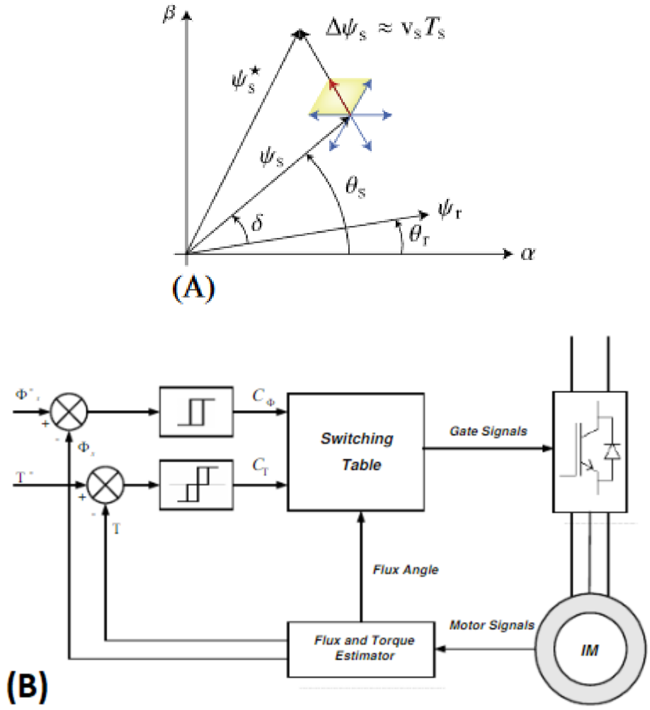

Figure 3.17: An example of a DTC: (A) operation principle and (B) block diagram [6, 17].

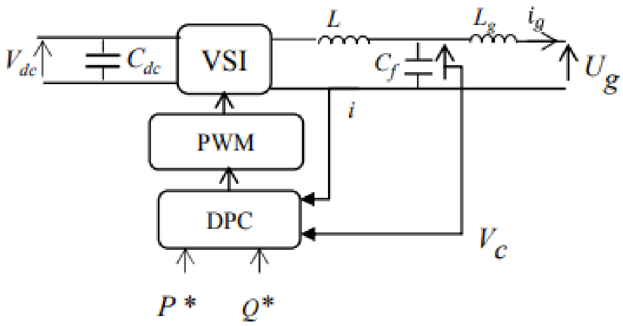

Figure 3.18: An example of a DPC for a single-phase converter [18].

$$J(k) = \sum_{l=k}^{k+N-1} \|y(l+1) - y^{*}(l+1)\|^{2},\; s.t. S_{w}(l) \in: \mathbb{S}(FCS)\, \forall l \in k, ..., k+N-1 \tag{3.37}$$

Noteworthy is the capability to incorporate system limitations into the control problem formulation. The optimal control problem is addressed by determining the necessary control action without relying on an external modulator, utilizing the equation $S_{w}(k) = argmin_{S_{w}(k)}\{Jk\}$ [6]. This process iterates at each sampling moment following a receding horizon policy [19, 20, 21].

The operational principle of FCS-MPC is demonstrated in Figure 3.19A, while its block diagram is depicted in Figure 3.19B.

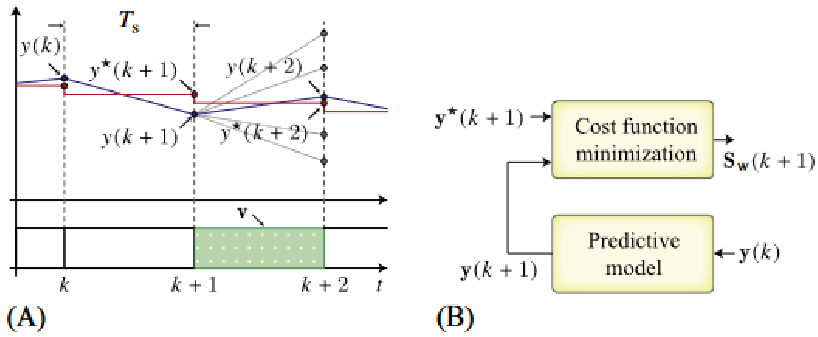

Figure 3.19: A generalised FCS-MPC: (A) operation principle and (B) block diagram [6].

3.3.6 Control of Converters - With Embedded Modulator

The discussion on controlling converters without an external modulator highlights the advantages of this approach, such as simplified implementation and enhanced dynamic performance. The power switch states remain fixed between sampling intervals by eliminating the need for an external modulator to produce power switch gate signals, facilitating rapid attainment of control references [6]. However, this technique often results in converters operating at variable switching frequencies, presenting challenges in designing passive components to prevent resonances. Consequently, the research community has concentrated on devising high-performance controllers that integrate the benefits of PWM-based output behaviour with modulator-free control strategies [6]. Advanced algorithms like Selective Harmonic Elimination MPC (SHE-MPC) [22] (see Section 2.3.3 Optimal PWM in [6]) have been proposed to address optimal PWM techniques within this context.

This control strategy will not be extensively discussed since it involves optimal PWM.

3.4 Main Decisions For the Project According to the State of the Art

3.4.1 For the topology of the converter

Due to the need for the converter to be bidirectional, a full-bridge topology has been selected to be implemented for the converter.

3.4.2 For the control strategy

Regarding the control strategy to be implemented for the converter, table 3.1 compares the various strategies analysed. According to this table, the Proportional Integral (PI) controller has been selected to be implemented in the converter due to the fact it presents a low value of total harmonic distortion (THD), only slightly surpassed by the Resonant Controller however it has not been selected because is more complex to be implemented. Moreover, the dynamic response which has been taken into account, for the PI controller is only slightly inferior in comparison to the

Hysteresis and the DPC, however, these have high THD values as well as variable switching frequencies.

Table 3.1: Comparison among the controllers.

Parameter	PI	Resonant Controller (PR)	Hysteresis	DPC	FCS-MPC
Steady State Response	Very low THD	The lowest THD	High THD, high ripple, and variable switching frequency	High THD and variable switching frequency	Low THD
Sensitivity to system parameters	None	None	None	None	Sensitive to system parameters
Dynamic response	Slightly inferior compared to Hysteresis, DPC and FCS MPC	Slightly inferior compared to Hysteresis, DPC and FCS MPC	Very fast	Very fast	Very fast

3.5 Summary

This chapter reviewed the fundamentals of bidirectional converters, focusing on their topologies, control strategies, and modulation methods. It explored various control techniques, including PWM-based linear control and advanced methods without a modulator. The chapter emphasized the importance of selecting appropriate converter topologies and control strategies to achieve efficient integration with AWES. It concluded with key decisions for the project's converter design based on the state-of-the-art review.

Chapter 4

Modelling and Simulation

This chapter is divided into four parts. In the first part, the details of the implementation of the converter and its control in PSIM are presented, in the second and third parts will show the simulation results and analysis for the analogue and digital control respectively while the fourth part will compare the results obtained in the second and third parts.

4.1 Modelling

This section details the method used to implement the proposed circuit, depicted in Figure 4.1, and its controller circuit, depicted in Figure 4.2, in simulations conducted using PSIM. The chosen switching frequency is 10kHz.

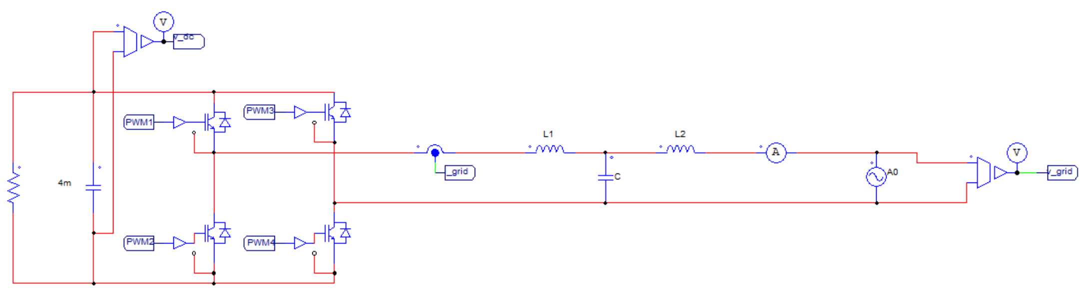

Figure 4.1: Proposed circuit.

4.1.1 LCL Filter

In this work, it was decided to go for an LCL filter. As the name suggests, the LCL filter consists of two inductors in series and a capacitor in parallel as shown in Figure 4.3. It provides greater harmonic attenuation, with 60dB/decade attenuation for frequencies above the resonance frequency, and 20dB/decade attenuation below the resonance frequency, thus allowing the inverter to be switched at lower frequencies, and the use of this filter results in better system performance.

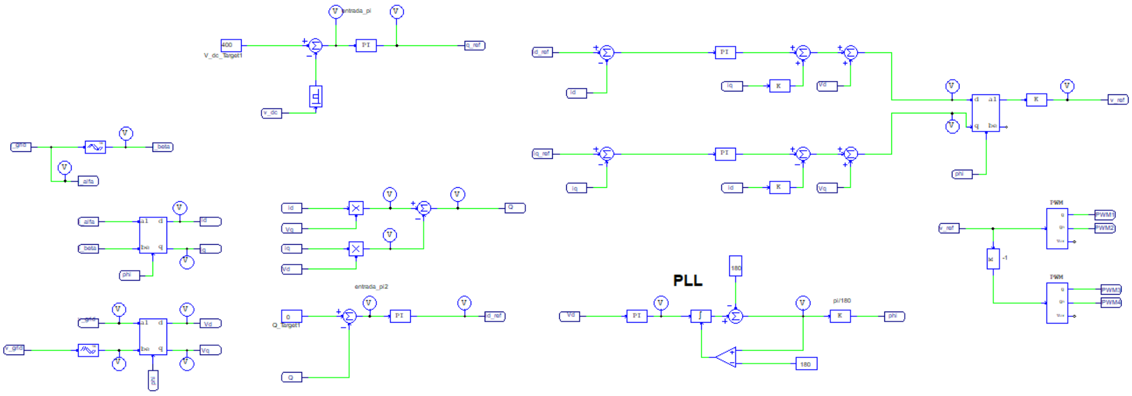

Figure 4.2: Proposed control circuit.

Furthermore, this filter allows for better decoupling between the impedance of the inverter and the grid. One of the parameters to pay attention to when dimensioning this filter is its cut-off frequency, which should be dimensioned taking into account approximately half of the converter's switching frequency so that the filter has sufficient attenuation within the switching range.

To obtain the values of the inductor L1 the following equation was used:

$$L_1 = \frac{V_{dc}}{4 * F_{sw} * \Delta I_{pp}} [23] \tag{4.1}$$

with F_{sw} being the switching frequency, and ΔI_{pp} being the max permissible current ripple. The ΔI_{pp} can be obtained as:

$$\Delta I_{pp} = I_{grid} * \sqrt{2} * I_{rip} [23] \tag{4.2}$$

with I_{grid} being the root mean square (RMS) value of the current and I_{rip} being the limitation, in percentage, of the current ripple in relation to the rated current.

For the value of the inductor L2, it can be obtained by using the following equations:

$$L = 0.1 * \frac{V_{grid}^2}{S * 2 * \pi * 50} [23] \tag{4.3}$$

$$L2 = L - L1 \tag{4.4}$$

with S being the power of the circuit which will be 3680 VA, and 0.1 being the chosen value for the percentage of max drop of rated voltage divided by 100.

For the value of the capacitator, the following equation was used:

$$C = \frac{0.05 * S}{V_{grid} * 2 * \pi * 50} [23] \tag{4.5}$$

with 0.05 being the limitation of the reactive power absorbed by the capacitator in relation to the value of S.

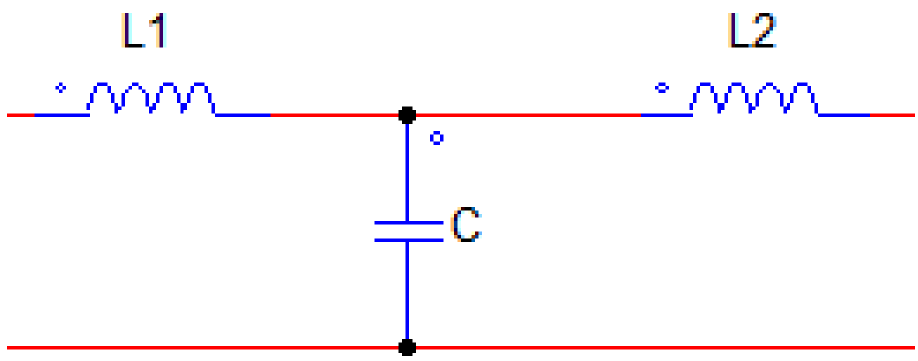

Figure 4.3: LCL filter of the converter circuit

4.1.2 Direct-Quadrature (d-q)

By demand, the direct-quadrature components will be used to control the converter. This subsection explains how it was implemented

4.1.2.1 Imaginary Orthogonal Phase in Single-Phase Systems

In single-phase converters, the challenge of applying the d-q synchronous frame transformation method arises due to the availability of only one phase. To address this issue, a second orthogonal phase must be created for each state variable in the circuit [24]. There are three approaches to achieve this:

- The first approach involves differentiating the converter output voltage and inductor current [25]. By differentiating the measured real component, a stationary orthogonal component is created. However, this method is sensitive to noise, as the converter's real-phase output waveform contains harmonics in addition to the fundamental component. This results in the differentiation process not yielding a purely orthogonal component. The errors in the stationary orthogonal phases significantly impact the converter feedback controller. Additionally, the differentiation calculations require a significant amount of microcontroller processing time [24].

- Another approach suggests using an observer to construct the β-axis component, as proposed in some works such as [26]. While this approach can deliver good results, it necessitates complex software and processing for design and implementation.

- The third technique involves generating a 90º phase shift in relation to the real phase to create an imaginary orthogonal phase [27, 28, 29, 30]. By utilizing equation (4.6), the original phase delay of one-fourth of the line phase of the system can create another component

(β) that is perpendicular to the original waveform (α), as demonstrated in Figure 4.4. The imaginary orthogonal component is estimated from the real component and introduces the dynamics of a quarter-cycle delay in its construction [24].

$$\begin{aligned} X_\alpha &= X * sin(w*t) \\ X_\beta &= X * sin(w*t-90) \end{aligned} \tag{4.6}$$

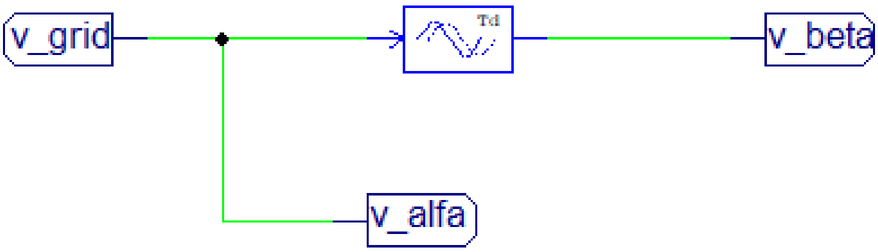

Figure 4.4: Circuit to obtain the α and β values in PSIM for the grid voltage

The first two approaches do not represent a simple solution or are cheap to implement, as such it was chosen the third option. The waveforms obtained from the phase shift can be seen in Figure 4.5.

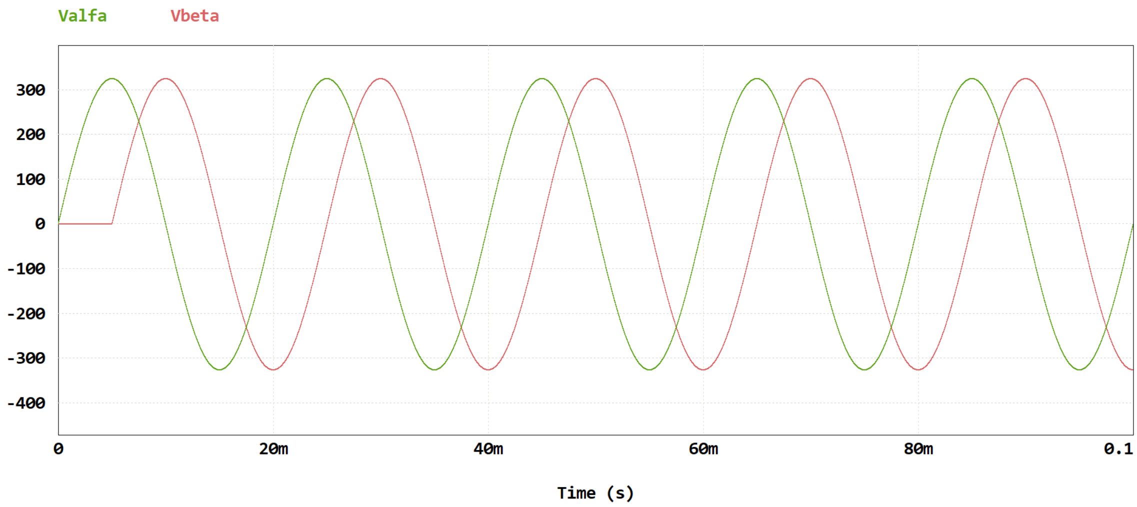

Figure 4.5: Waveforms of V_α and V_β

4.1.2.2 α-β to d-q Transformation

The next step is to transform the α-β components into the d-q components. This transformation is achieved using the following voltage matrix:

$$\begin{bmatrix} V_d \\ V_q \end{bmatrix} = \begin{bmatrix} cos(\phi) & sin(\phi) \\ -sin(\phi) & cos(\phi) \end{bmatrix} * \begin{bmatrix} V_\alpha \\ V_\beta \end{bmatrix} \tag{4.7}$$

and for current:

$$\begin{bmatrix} I_d \\ I_q \end{bmatrix} = \begin{bmatrix} cos(\phi) & sin(\phi) \\ -sin(\phi) & cos(\phi) \end{bmatrix} * \begin{bmatrix} I_\alpha \\ I_\beta \end{bmatrix} \tag{4.8}$$

Figure 4.6 shows the waveforms for V_d and V_q.

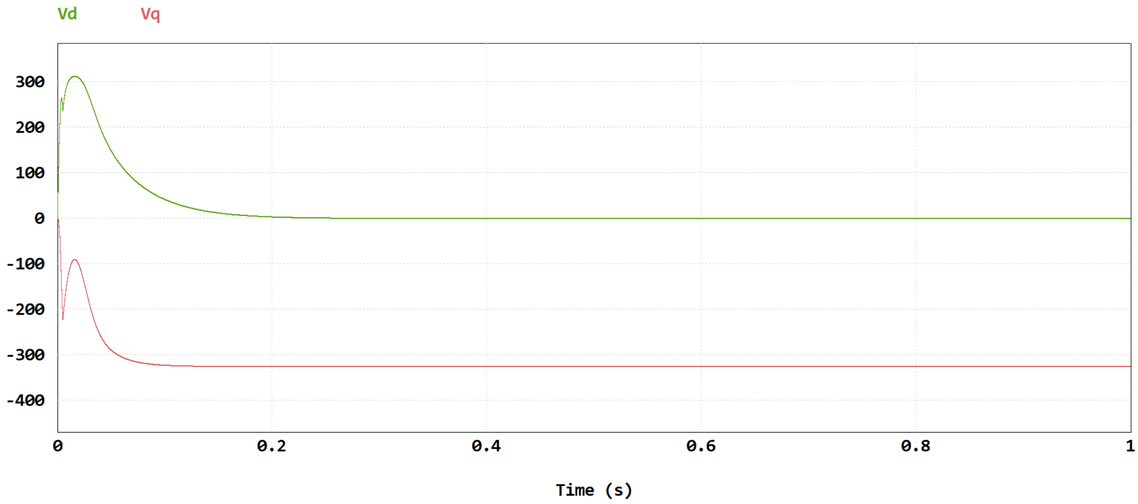

Figure 4.6: Waveforms of V_d and V_q

4.1.2.3 Phase Locked Loop (PLL)

To perform the transformation from α-β to d-q components, it is essential to determine the angle ϕ. This is achieved using a PLL, as shown in Figure 4.7. In this figure, the d component of the grid voltage is processed through a PI controller and subsequently through an external resettable integrator to obtain the value of ϕ. The PI controller values are determined as follows:

$$K_p = 2 * \zeta * w_n \tag{4.9}$$

$$K_i = w_n^2 \tag{4.10}$$

$$T_i = \frac{K_p}{K_i} \tag{4.11}$$

with ζ being the damping ratio and w_n being the natural frequency. Their values are:

$$0.5 \leq \zeta \leq 1 \tag{4.12}$$

$$0.1 * w_o \leq w_n \leq 0.5 * w_o \tag{4.13}$$

with w_o being equal to $2 * \pi * f$, where f is the grid frequency.

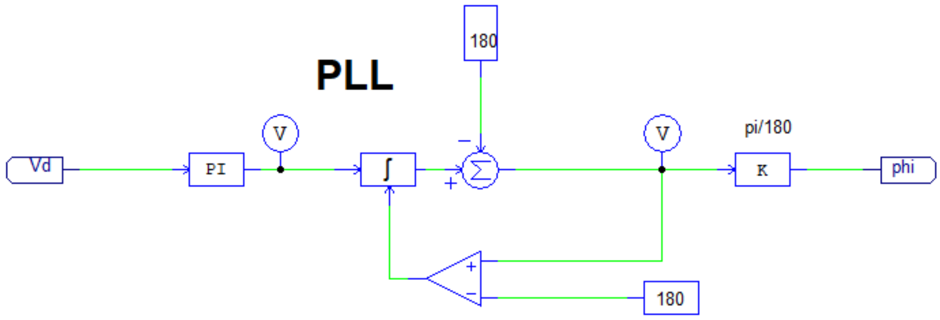

Figure 4.7: Circuit of the PLL created based on the Conventional 3-Phase PLL shown in [31].

The waveform of ϕ, in degrees, can be seen in Figure 4.8.

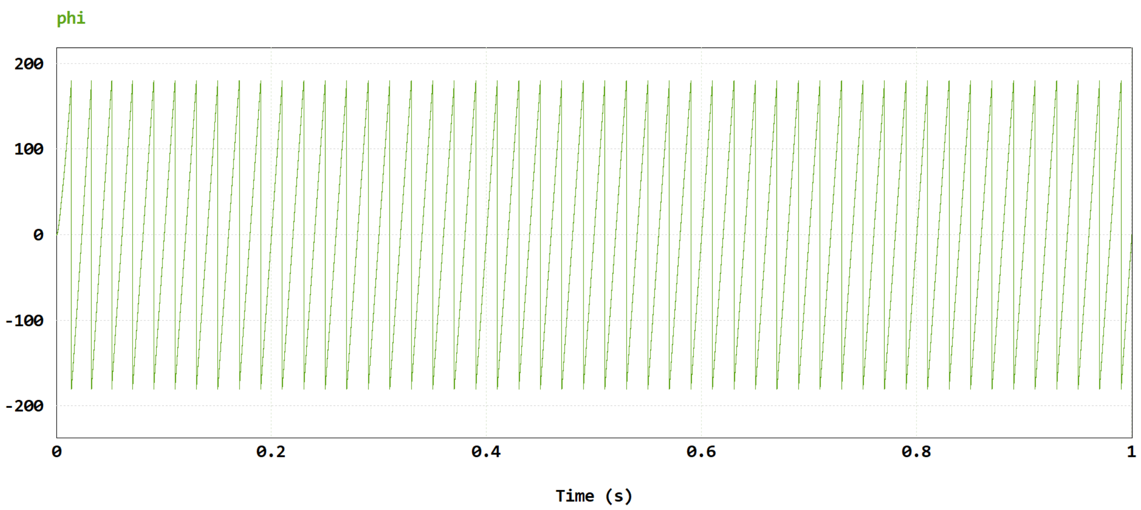

Figure 4.8: Waveform of ϕ obtained through the PLL of Figure 4.7.

4.1.2.4 Controller

After the grid voltage and current are transformed into d-q components (V_d, V_q, I_d, and I_q), they enter a decoupling circuit, as shown in Figure 4.9. In this circuit, the reference values for the d and q components are subtracted from the measured I_d and I_q respectively. The d component represents the reactive power, while the q component represents the active power. These differences are then processed through a PI controller with gains $K_p = 5$ and $K_i = 300$. Following the PI controller, the d component is adjusted by adding V_d and its decoupling term $I_q * w * L$, where $w = 2 * \pi * f$ and L is the total inductance. Similarly, the q component is adjusted by adding V_q and its decoupling term $I_d * w * L$.

After the sums, the d and q components will be transformed back to α and β components using the following matrix:

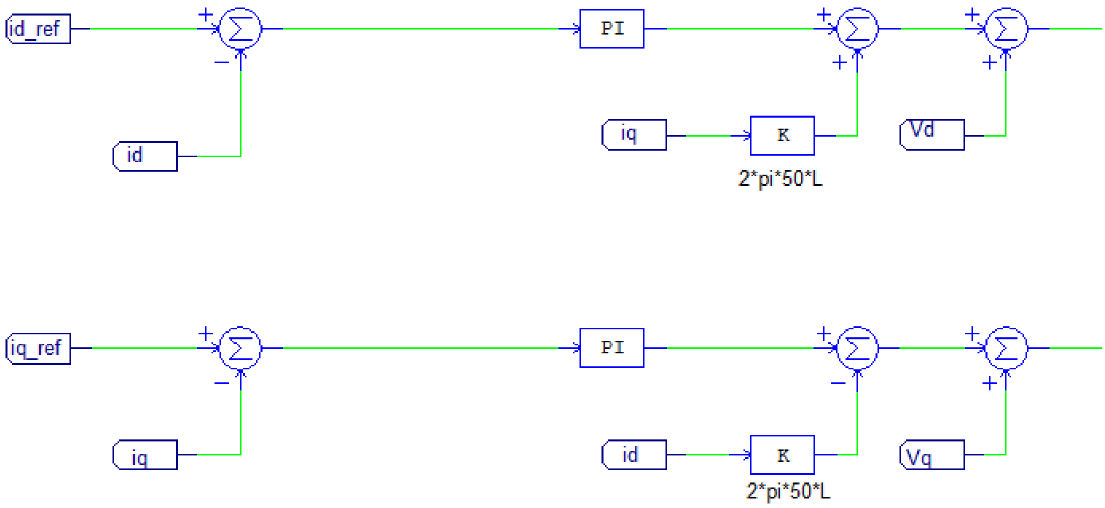

Figure 4.9: The d and q decoupling terms on the controller side.

$$\begin{bmatrix} V_\alpha \\ V_\beta \end{bmatrix} = \begin{bmatrix} cos(\phi) & -sin(\phi) \\ sin(\phi) & cos(\phi) \end{bmatrix} * \begin{bmatrix} V_d \\ V_q \end{bmatrix} \tag{4.14}$$

Then, only the α component is used and divided by the desired DC voltage, as illustrated in Figure 4.10.

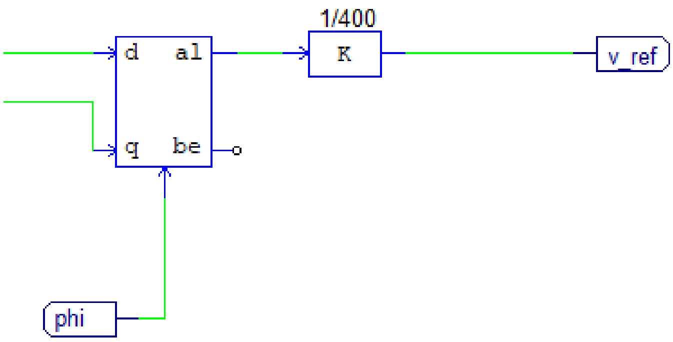

Figure 4.10: Transformation of the d-q components to α-β components, divided by the DC voltage reference.

With component α divided, it will then be modulated by two unipolar PWMs, one using the α component and the other using α multiplied by -1, as shown in Figure 4.11. These PWM signals then control the IGBTs of the converter.

To control the I_q reference, a voltage-oriented control (VOC) approach was implemented. This was chosen to enable the converter to regulate the voltage of the DC bus, specifically maintaining it at 400V. Figure 4.12 illustrates this control strategy.

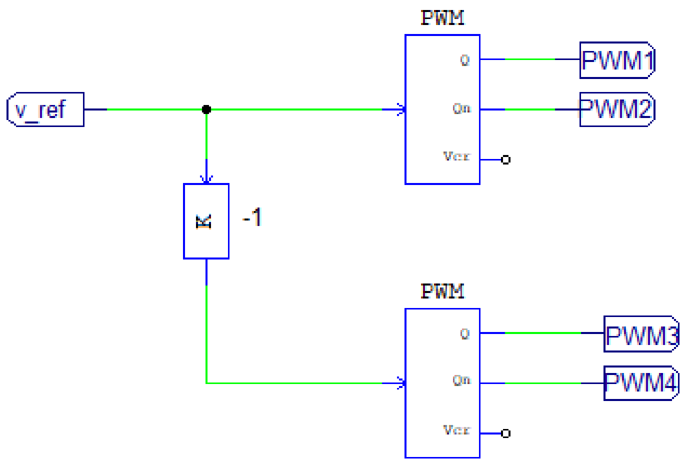

Figure 4.11: Unipolars PWMs used for the controller circuit.

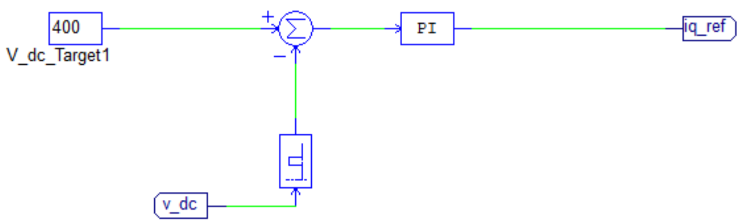

Figure 4.12: Voltage-Oriented Control (VOC). Circuit to obtain the reference of I_q through the DC Voltage.

The reference value for I_d was determined by calculating the reactive power (Q) in the grid using the following equation:

$$Q = I_d * V_q - I_q * V_d \tag{4.15}$$

This calculation is depicted in Figure 4.13. Subsequently, the target Q was set to zero, and the difference between the target and the calculated Q was input into a PI controller. The output of the PI controller provides the reference value for I_d, as illustrated in Figure 4.14.

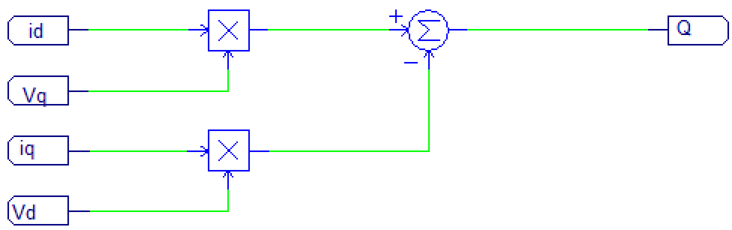

Figure 4.13: Circuit Reactive Power (Q) calculation.

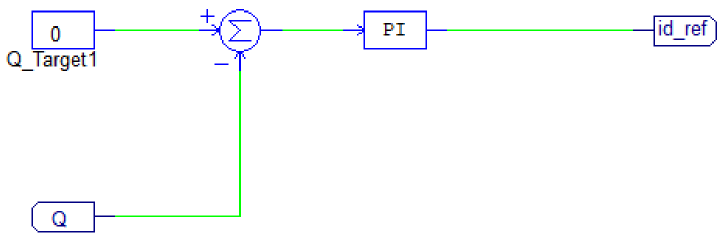

Figure 4.14: Circuit to obtain the reference of I_d through the Reactive Power.

4.2 Simulations with Analogue Control

This section will present the simulations with analogue control conducted.

4.2.1 Case 1 - Normal Operation with a Load

Here, a resistor of 65Ω was employed in the DC bus to replicate the load from both the batteries and the motor/generator. The capacitor began with an initial voltage of 380V. The circuit configuration is depicted in Figure 4.1. The waveforms obtained from this simulation are illustrated in Figure 4.15.

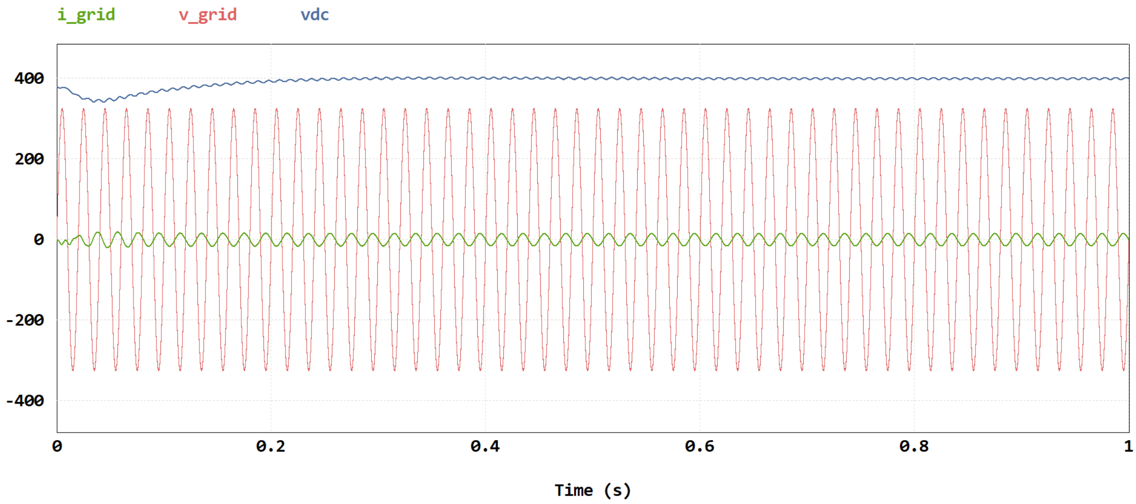

Figure 4.15: Waveforms for the normal operation with a load: the grid current in green, the grid voltage in red, and the DC voltage in blue.

The expected results have been achieved: the DC voltage stabilizes at 400V, and the grid current lags the grid voltage by 180º because it flows from the grid to the DC bus.

Figure 4.16 displays the harmonic spectrum of the grid current. From Figures 4.17 and 4.18, it is evident that the fundamental harmonic is at 50 Hz, with minimal presence of other harmonics. Only the 3rd harmonic (150 Hz) shows a small peak, indicating minimal waveform distortion in the grid current. This observation aligns with the obtained total harmonic distortion (THD) value of $1,5\%$, as shown in Figure 4.19 using PSIM.

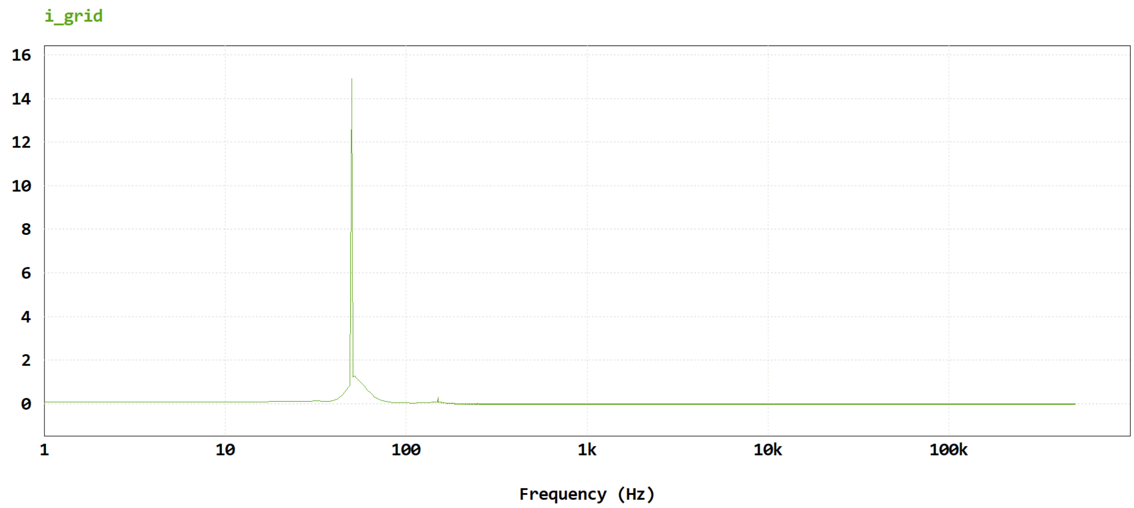

Figure 4.16: Harmonic spectrum of the grid current.

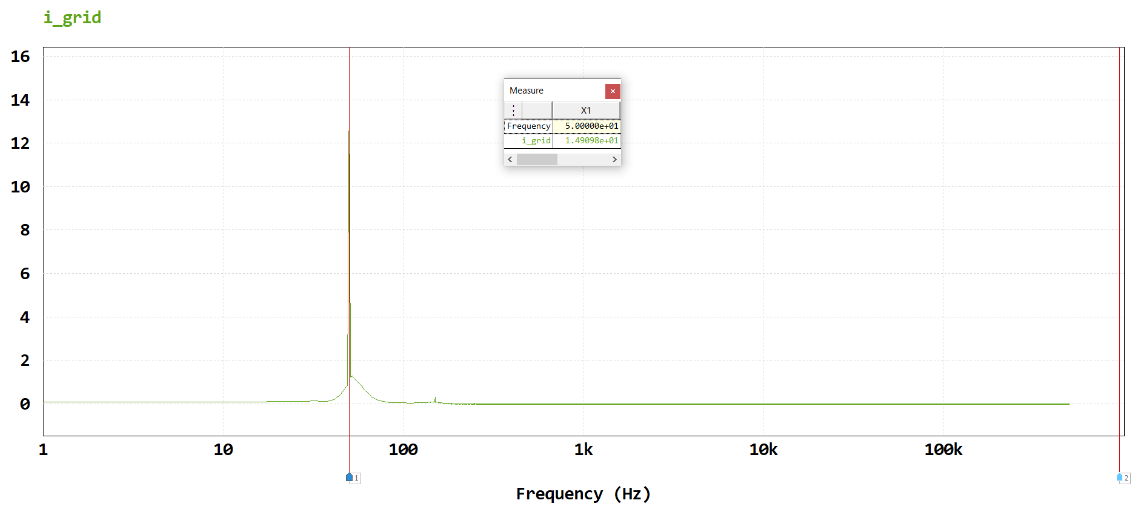

Figure 4.17: Fundamental harmonic highlighted in the harmonic spectrum of the grid current.

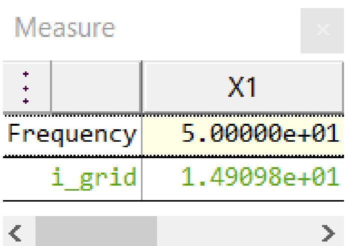

Figure 4.18: Measure box shown in Figure 4.17.

	X1	X2	Δ	THD
Time	7.60776e-01	7.80776e-01	2.00000e-02	freq=50
i_grid	-4.33721e+00	-4.33643e+00	7.81433e-04	1.50000e-02

Figure 4.19: THD of the grid current

4.2.2 Case 2 - Normal Operation with a Current Source

Here a current source of 6A was employed in the DC bus instead of the resistor to simulate the current being supplied by the batteries and/or the motor/generator. The capacitor started with an initial voltage of 380V. The circuit can be seen in Figure 4.20.

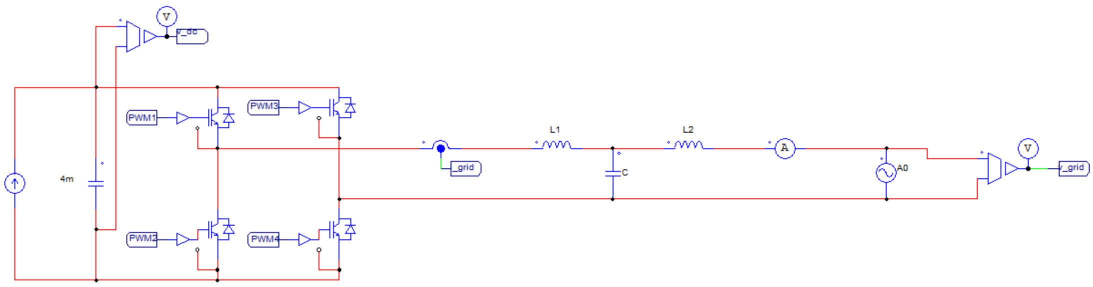

Figure 4.20: Circuit with the resistor replaced by a current source.

The waveforms obtained in this simulation can be seen in Figure 4.21.

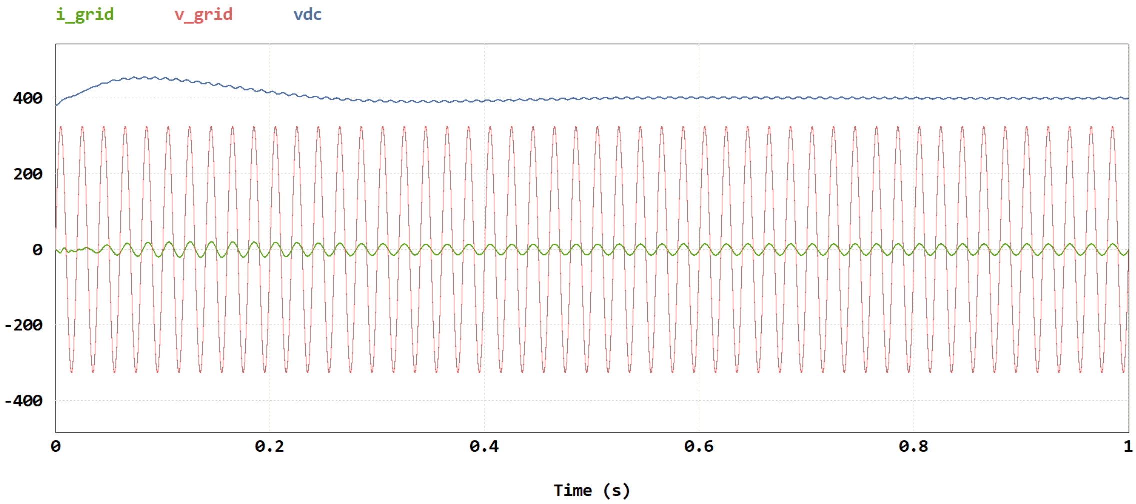

Figure 4.21: Waveforms for the normal operation with a current source: the grid current in green, the grid voltage in red, and the DC voltage in blue.

The expected results were achieved. Similar to the scenario described in 4.2.1, the DC voltage stabilizes at 400V. However, in this setup, the grid current is in phase with the grid voltage because the current flows from the DC bus to the grid.

4.2.3 Case 3 - Operation with Alternate Load

Here a voltage-controlled current source was employed in the DC bus to simulate the varying load from the batteries and the motor/generator. The capacitor started with an initial voltage of 380V. The circuit can be seen in Figure 4.22.

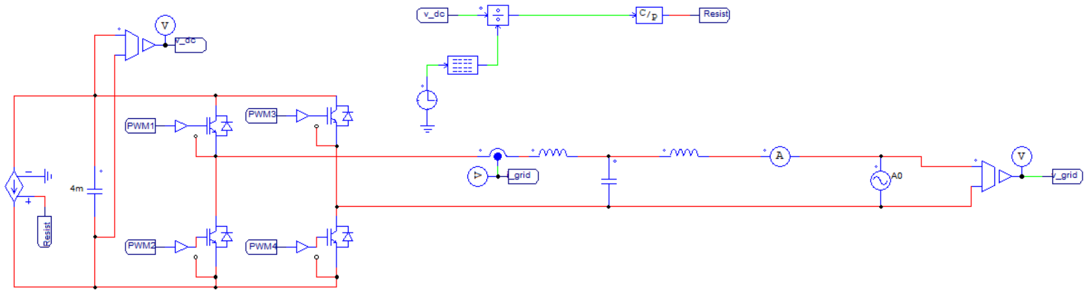

Figure 4.22: Circuit with the resistor replaced by a voltage-controlled current source.

As depicted in Figure 4.22, an additional circuit is implemented to determine the values of the voltage-controlled current source. These values are derived by dividing the DC voltage by a Lookup table that emulates resistance values varying over time between 65Ω and 130Ω, as shown in Figure 4.23. Subsequently, the output passes through a control-to-power interface, resulting in the voltage-controlled current source having roughly the value of 6,1538A when the Lookup table corresponds to 65Ω, and 3,0769A when it corresponds to 130Ω.

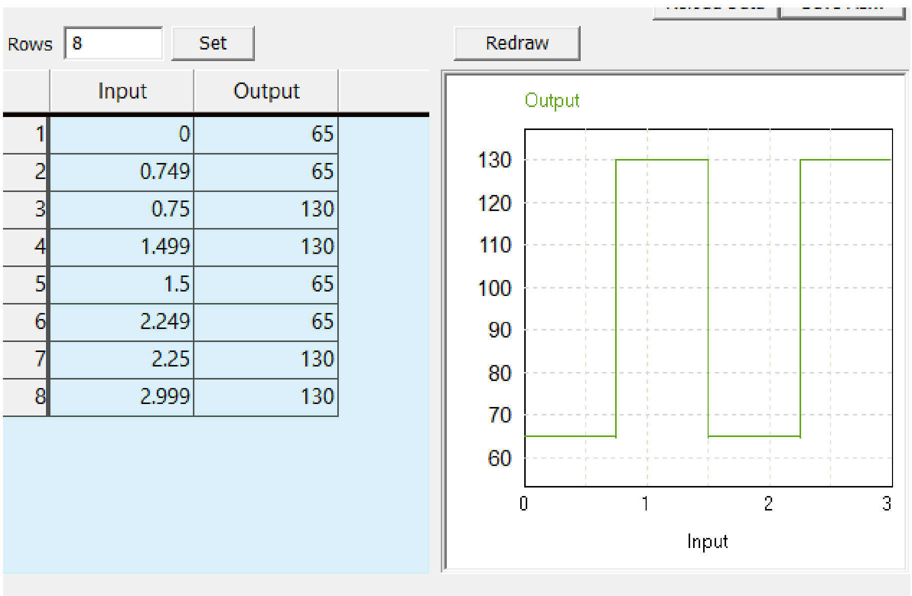

	Input	Output
1	0	65
2	0.749	65
3	0.75	130
4	1.499	130
5	1.5	65
6	2.249	65
7	2.25	130
8	2.999	130

Figure 4.23: Lookup Table for the voltage-controlled current source.

The waveforms obtained in this simulation can be seen in Figure 4.24.

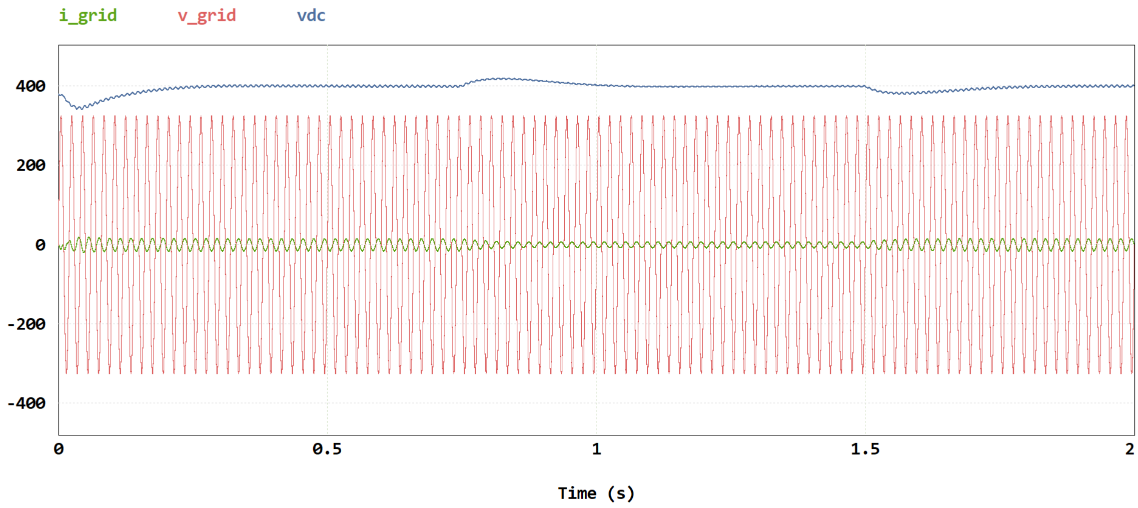

Figure 4.24: Obtained waveform for the operation with an alternate load: the grid current in green, the grid voltage in red, and the DC voltage in blue.

The expected results were achieved: the DC voltage ended up stabilising consistently at 400V regardless of load changes. The amplitude of the grid current varies accordingly with load changes, decreasing with increased load and increasing with decreased load.

4.2.4 Case 4 - Operation with Alternate Reference Voltage

The circuit used here is identical to the one described in 4.2.1. However, the voltage-oriented control (VOC) has been adjusted, specifically varying the reference voltage within the VOC between 380V and 420V. These adjustments are illustrated in Figure 4.25.

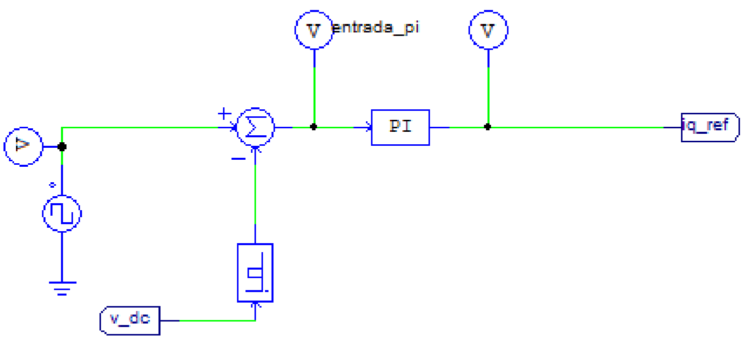

Figure 4.25: VOC with the constant changed with a square wave voltage source.

The waveforms obtained in this simulation can be seen in Figure 4.26.

The expected results were achieved: with each change in the reference voltage for the DC bus (380V or 420V in this case), the DC voltage stabilizes at the specified reference value. Concurrently, the amplitude of the grid current varies accordingly with changes in the DC voltage, increasing when the DC voltage increases and decreasing when the DC voltage decreases.

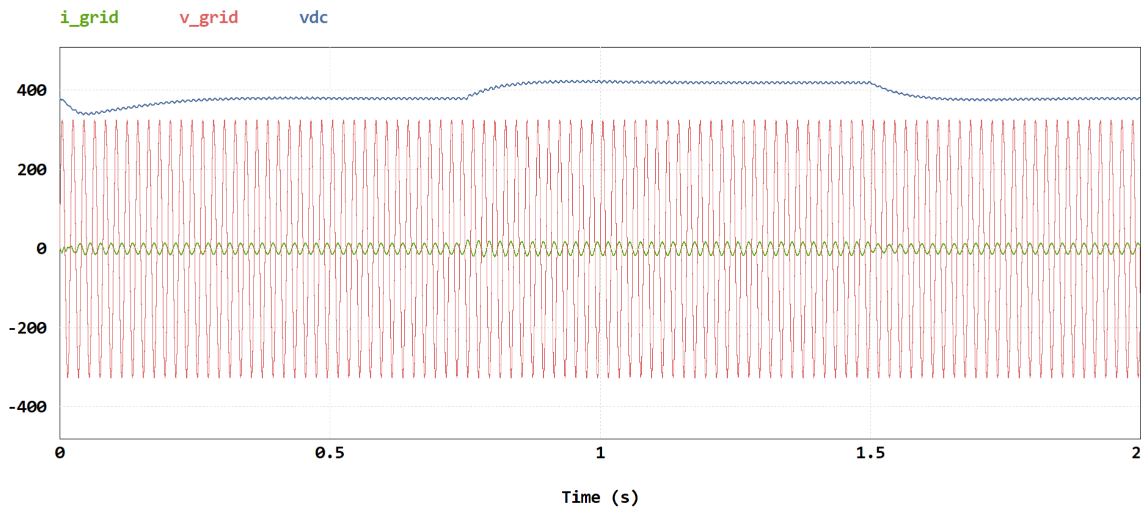

Figure 4.26: Obtained waveform for the operation with an alternate reference voltage: the grid current in green, the grid voltage in red, and the DC voltage in blue.

4.2.5 Case 5 - Starting Operation

To prevent obtaining the current waveform depicted in Figure 4.27, which exhibits a spike at the beginning of the waveform, a modification was made to the circuit described in 4.2.3. A resistor of $17,5\Omega$ was added on the grid side between the filter and the voltage source. This resistor is initially in place and will be bypassed by a switch after 0.7 seconds from the start of operations. This modification is illustrated in Figure 4.28. The load on the DC bus is set to simulate a load of 65Ω for $t \geq 0,7$s and an open circuit for $t < 0,7$s.

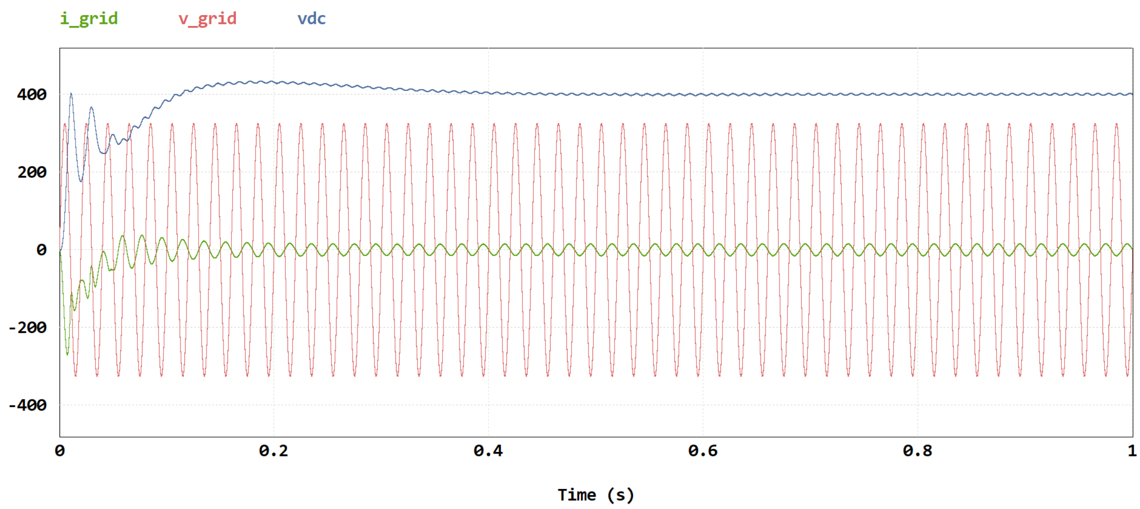

Figure 4.27: Obtained waveform for the normal operation with a load when the initial capacitor voltage is 0: the grid current in green, the grid voltage in red, and the DC voltage in blue.

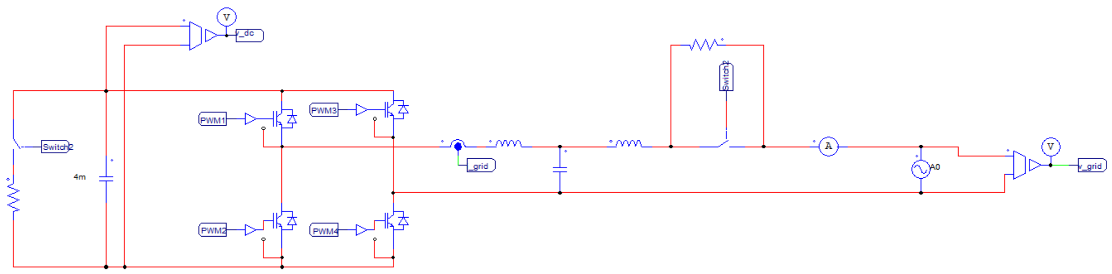

Figure 4.28: Circuit in 4.2.3 with a resistor added on the grid side and a switch to the resistor on the DC bus so that the system alternates between an open circuit and a 65Ω Load.

Furthermore, changes were made to the controller circuit, as shown in Figures 4.29 and 4.30. Here, the reference of q in the decoupling phase was changed to a constant while $t < 0,7$s, only changing to the VOC when $t = 0,7$s and the reference of the VOC was changed so that the VOC only effectively initializes when $t = 0,7$s.

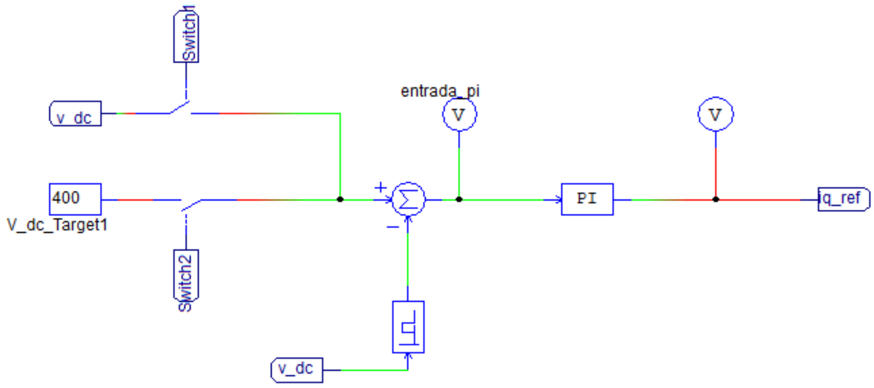

Figure 4.29: Changes in the reference of the VOC.

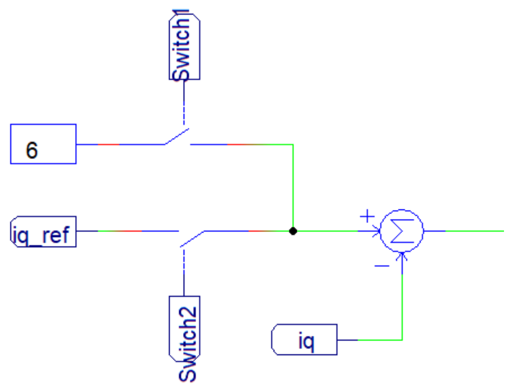

Figure 4.30: Changes in the reference of q in the decoupling phase.

In Figure 4.31, a circuit that controls the added switches is shown.

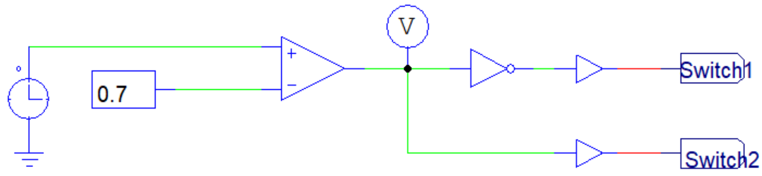

Figure 4.31: Circuit that controls the new switches.

The waveforms obtained in this simulation can be seen in Figure 4.32.

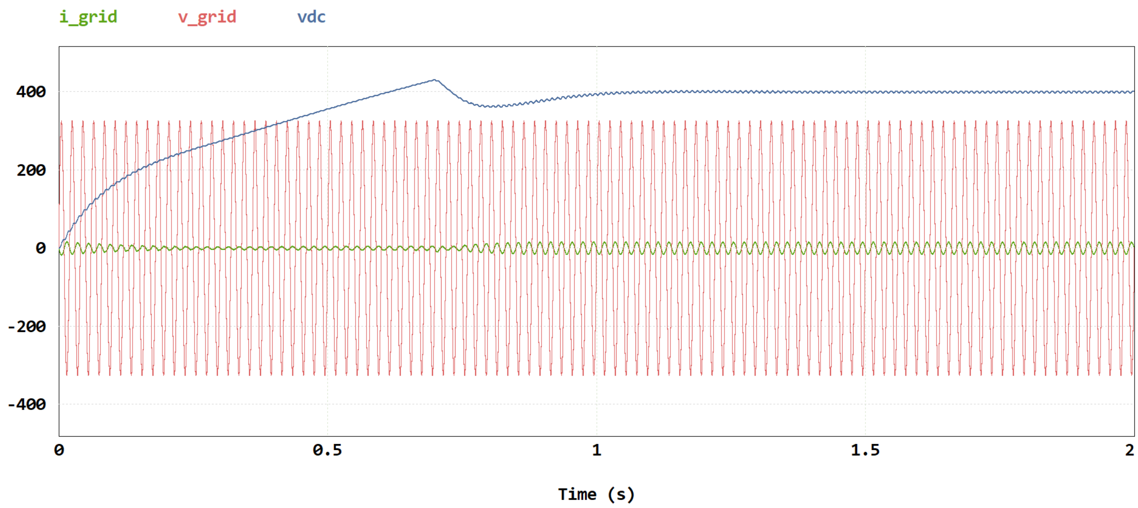

Figure 4.32: Waveforms for the starting operation: the grid current in green, the grid voltage in red, and the DC voltage in blue.

As shown in Figure 4.32, the grid current did not exhibit a spike at the beginning of the simulation. And from $t = 0,7s$ onwards the circuit is operating in normal condition with a load of 65Ω.

4.2.6 Case 6 - Simulations with IGBTs

This subsection employs non-ideal IGBTs for the simulations, replacing the ideal IGBTs.

4.2.6.1 Simulation with IKW30N60H3

Using the values in the datasheet [32], the circuit was simulated with four IKW30N60H3 instead of ideal IGBTs. The results are shown in Figure 4.33 and Figure 4.34.

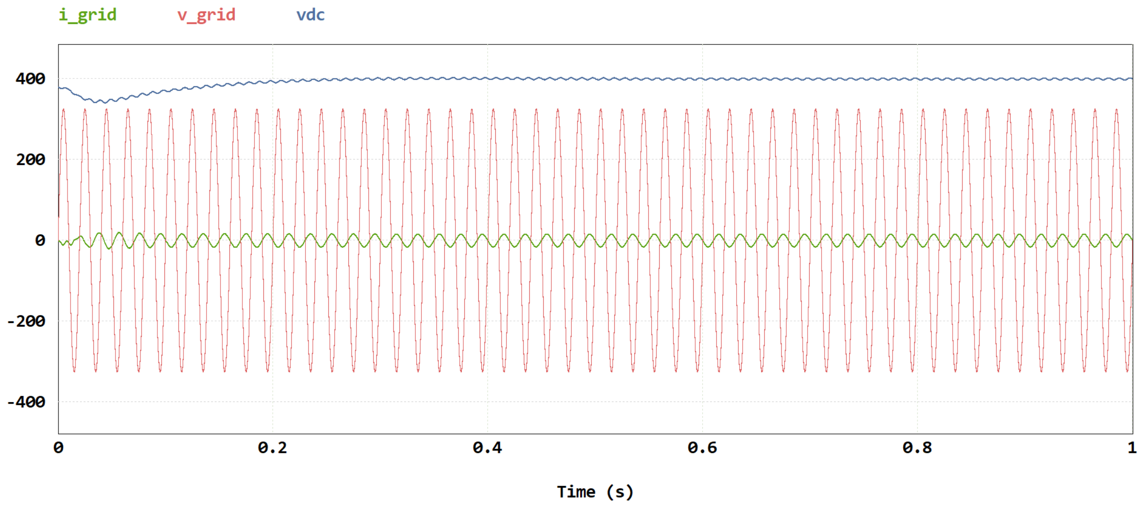

Figure 4.33: Waveforms of the analogue simulation with IKW30N60H3: the grid current in green, the grid voltage in red, and the DC voltage in blue.

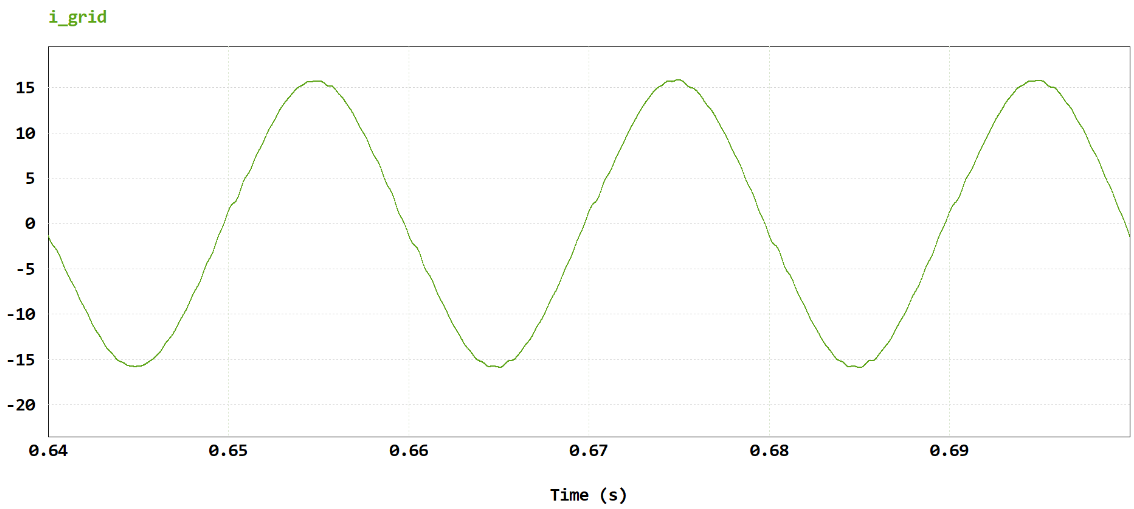

Figure 4.34: Current grid of the analogue simulation with IKW30N60H3

In Figure 4.34, it can be seen that the waveform is distorted, this is because switching on and off takes different amounts of time to execute. To address this issue, a dead time must be added. To obtain the value of the dead time we used the following equation:

$$tdead = (t_{d.off.max} - t_{d.on.min} + t_{pdd.max} - t_{pdd.min}) * 1,2 \tag{4.16}$$

Where, $t_{d.off.max}$ is the maximum turn-off delay time, $t_{d.on.min}$ is the minimum turn-on delay time, $t_{pdd.max}$ is the maximum propagation delay of the driver, $t_{pdd.min}$ is the minimum propagation delay of the driver and 1,2 is the safety margin value to be multiplied [33].

With the dead time, the results shown in Figures 4.35 and 4.36 were obtained.

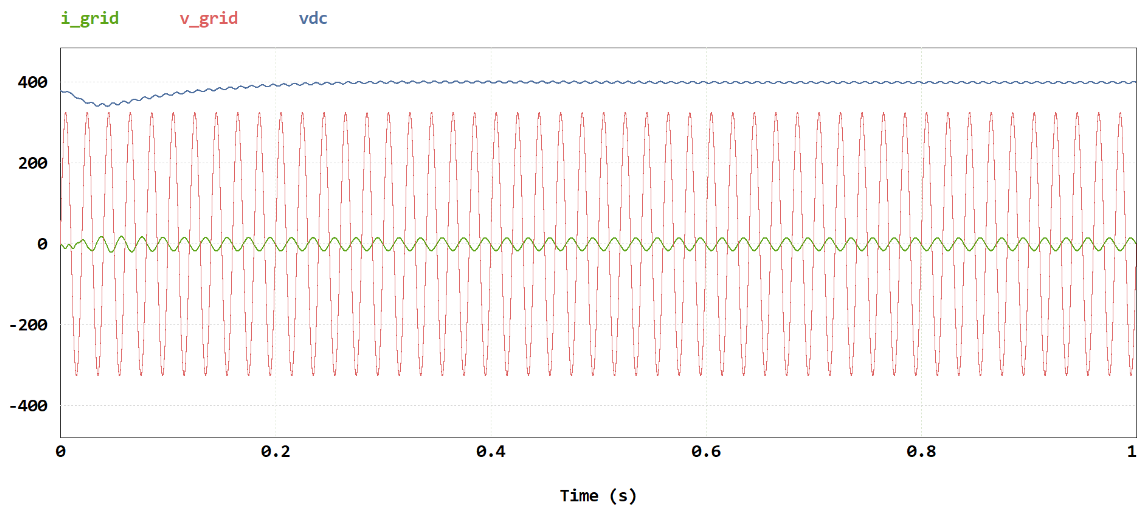

Figure 4.35: Waveforms of the analogue simulation with IKW30N60H3 and dead time: the grid current in green, the grid voltage in red, and the DC voltage in blue.

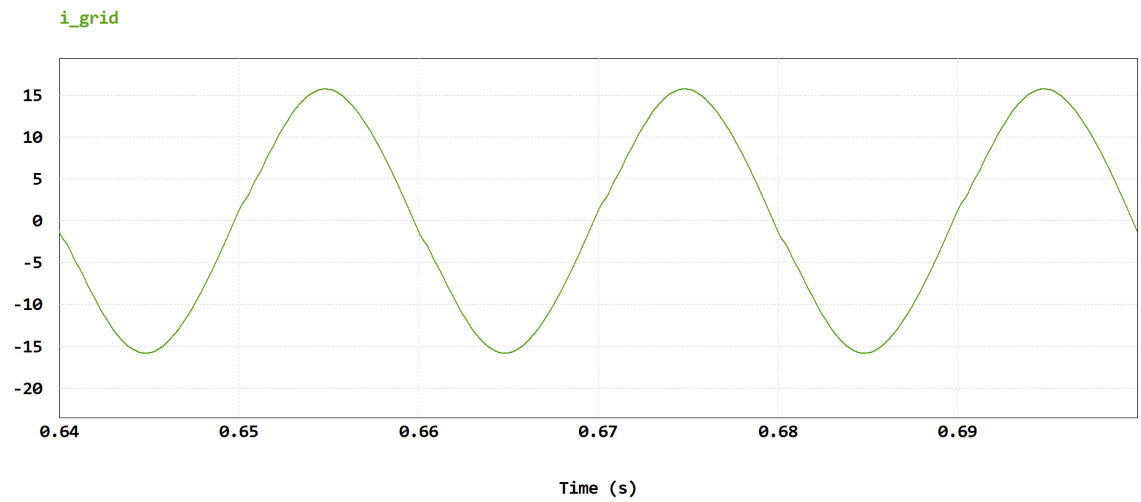

Figure 4.36: Current grid of the simulation with IKW30N60H3 and dead time.

In Figure 4.36, it can be seen that the distortion has greatly diminished in comparison with before. Figure 4.37 provides a clearer view by displaying the currents both with and without dead time.

4.2.6.2 Simulation with BIDNW30N60H3

Using the values in the datasheet [34], the circuit was simulated with four BIDNW30N60H3 instead of ideal IGBTs. The results are shown in Figure 4.38 and Figure 4.39.

In Figure 4.39, it can be seen that, like with IKW30N60H3, the waveform shows distortions in the waveform.

Using the formula 4.16, the dead time was obtained and with it, the results shown in Figures 4.40 and 4.41 were obtained.

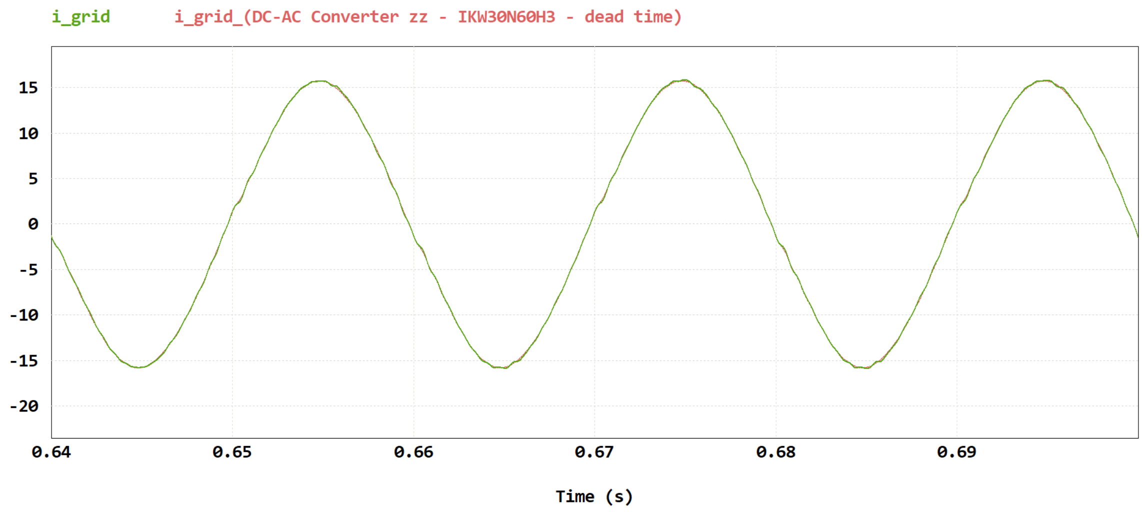

Figure 4.37: Comparison of the grid currents of the simulation with IKW30N60H3 with dead time, in red, and without it, in green.

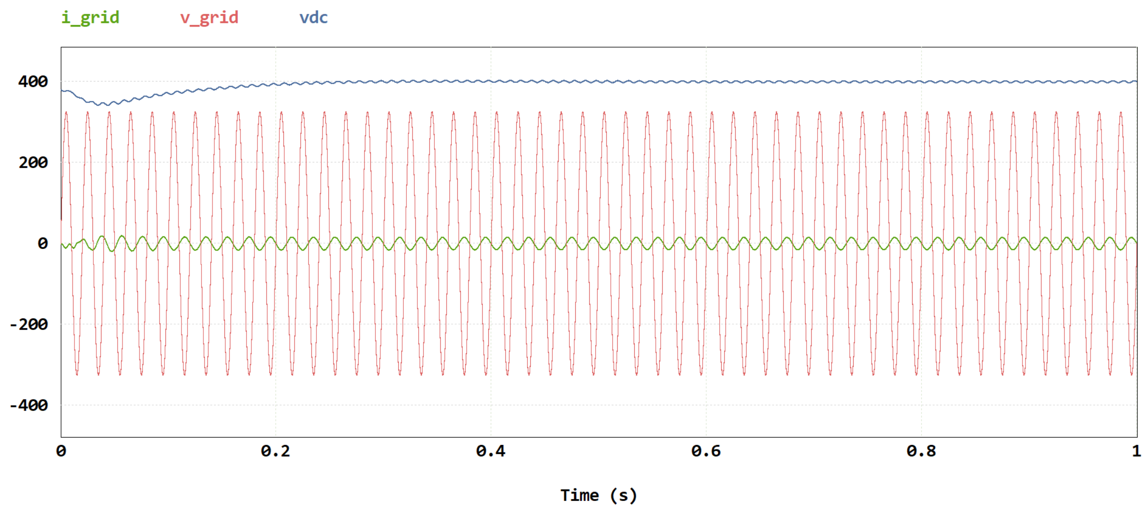

Figure 4.38: Waveforms of the analogue simulation with BIDNW30N60H3: the grid current in green, the grid voltage in red, and the DC voltage in blue.

In Figure 4.41, it can be seen that the distortion has greatly diminished in comparison with before. Figure 4.42 provides a clearer view by displaying the currents both with and without dead time.

4.2.7 Case 7 - Simulations with MOSFETs

This subsection employs non-ideal MOSFETs for the simulations, replacing the ideal IGBTs.

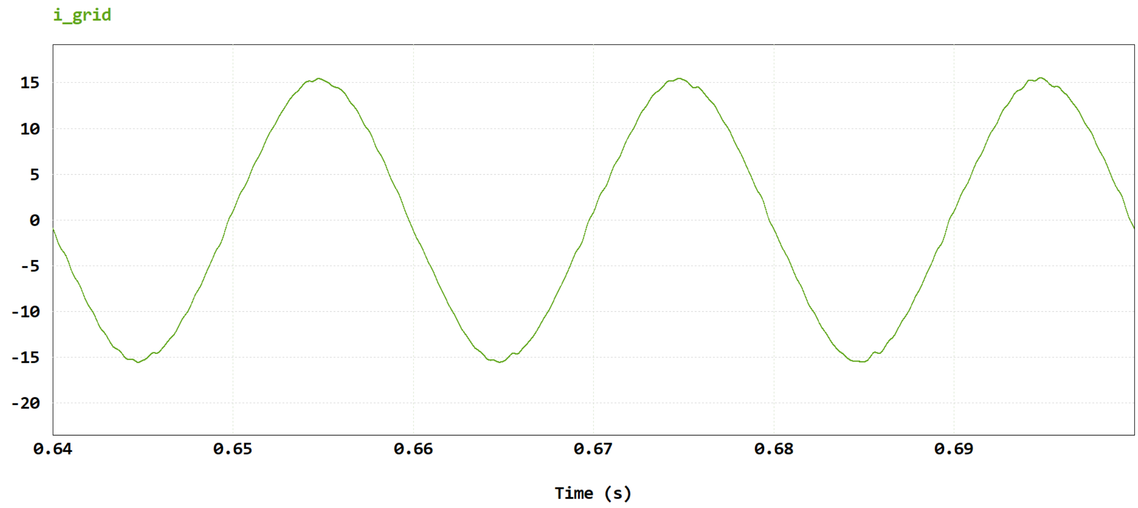

Figure 4.39: Current grid of the analogue simulation with BIDNW30N60H3

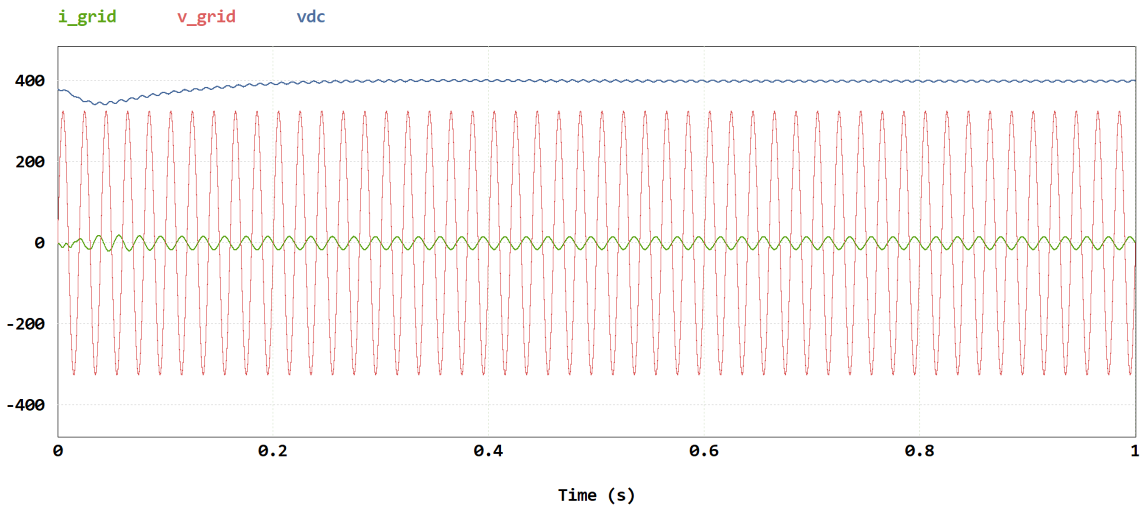

Figure 4.40: Waveforms of the analogue simulation with BIDNW30N60H3 and dead time: the grid current in green, the grid voltage in red, and the DC voltage in blue.

4.2.7.1 Simulation with IPZ60R040C7

Using the values in the datasheet [35], the circuit was simulated with four IPZ60R040C7 instead of ideal IGBTs. The results are shown in Figure 4.43 and Figure 4.44.

In Figure 4.44, it can be seen that, like for the IGBTs, the waveform shows distortions in the waveform.

Adding dead time and simulating with it, the results shown in Figures 4.45 and 4.46 were obtained.

In Figure 4.46, it can be seen that the distortion has greatly diminished in comparison with before. Figure 4.47 provides a clearer view by displaying the currents both with and without dead time.

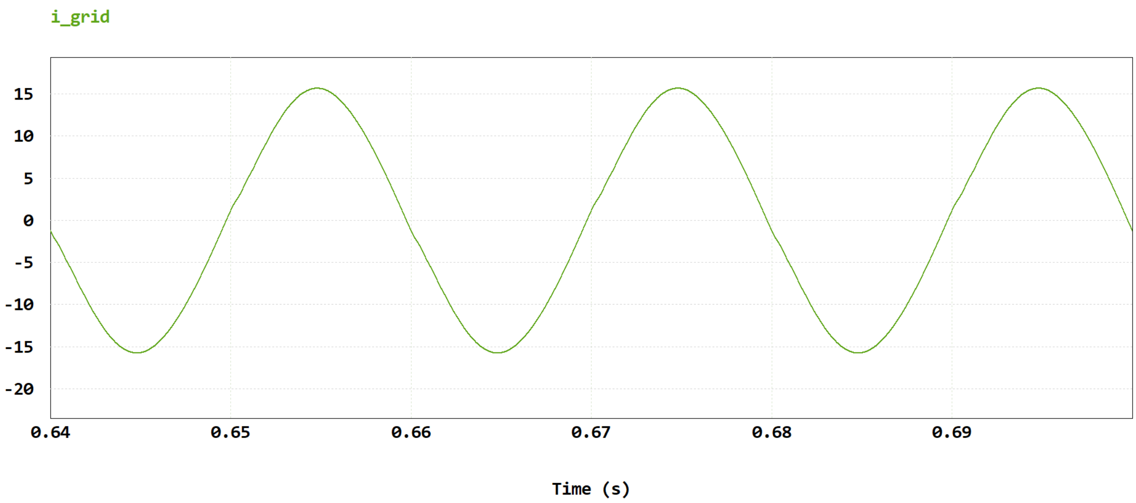

Figure 4.41: Current grid of the simulation with BIDNW30N60H3 and dead time.

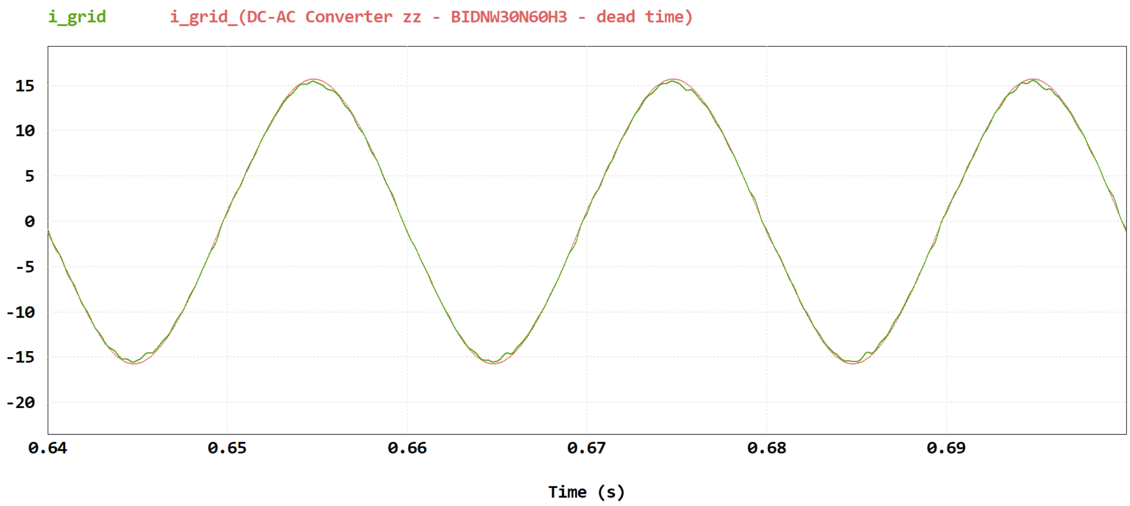

Figure 4.42: Comparison of the grid currents of the simulation with BIDNW30N60H3 with dead time, in red, and without it, in green.

4.2.7.2 Simulation with IXTH30N60L2

Using the values in the datasheet [36], the circuit was simulated with four IXTH30N60L2 instead of ideal IGBTs. The results are shown in Figure 4.48 and Figure 4.49.

In Figure 4.49, it can be seen that, like for the IPZ60R040C7, the waveform shows distortions in the waveform.

Adding dead time and simulating with it, the results shown in Figures 4.50 and 4.51 were obtained.

In Figure 4.51, it can be seen that the distortion has greatly diminished in comparison with before. Figure 4.52 provides a clearer view by displaying the currents both with and without dead time.

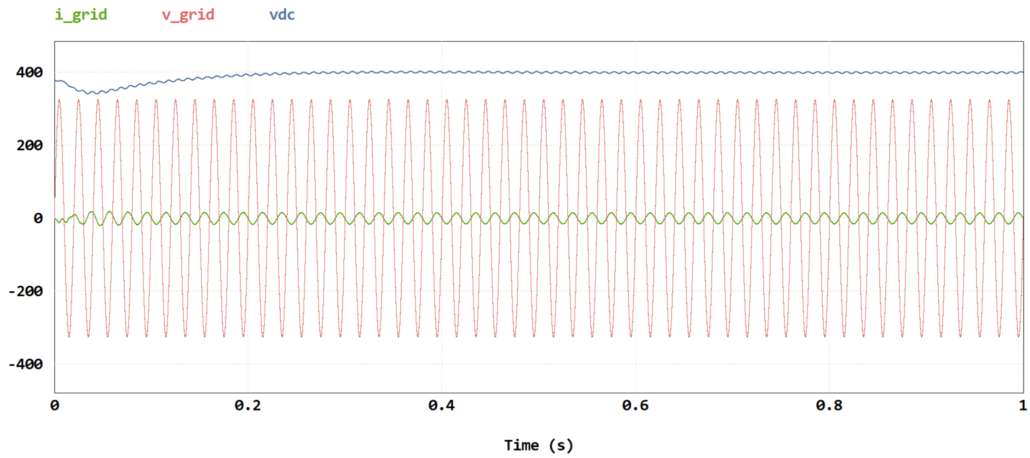

Figure 4.43: Waveforms of the analogue simulation with IPZ60R040C7: the grid current in green, the grid voltage in red, and the DC voltage in blue.

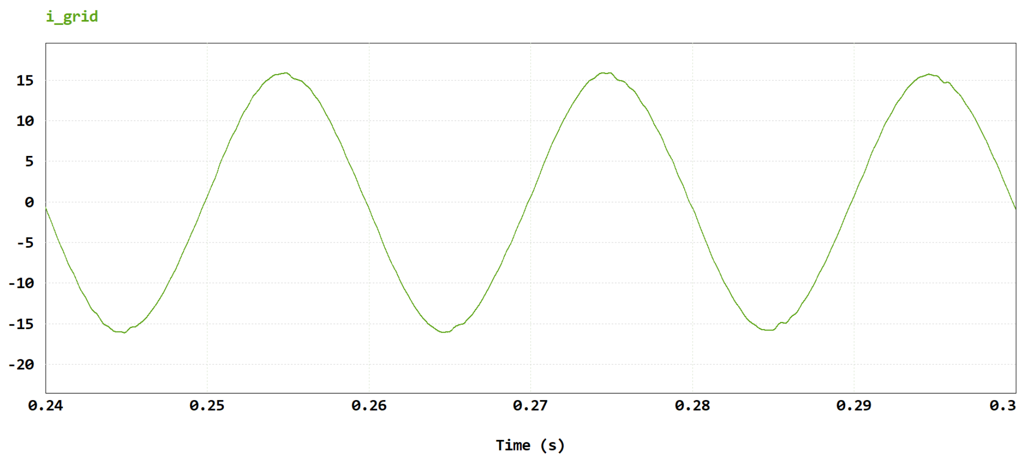

Figure 4.44: Current grid of the analogue simulation with IPZ60R040C7

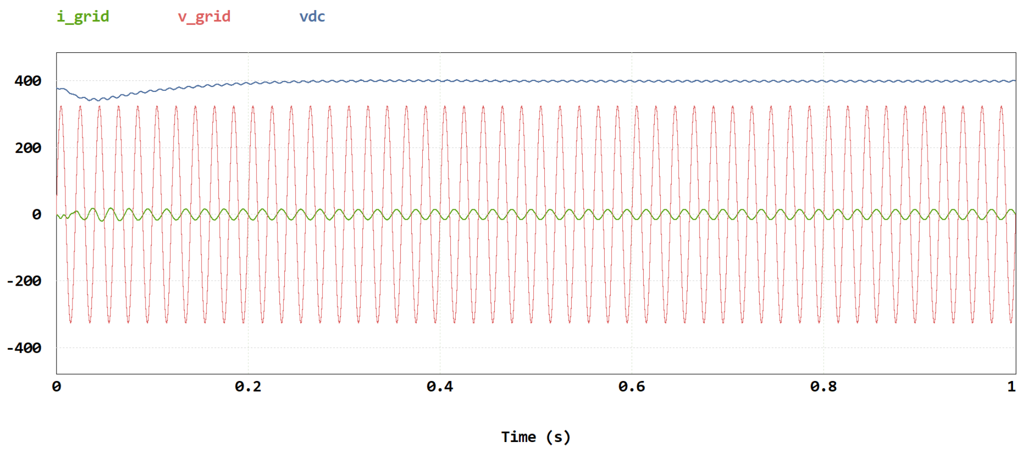

Figure 4.45: Waveforms of the analogue simulation with IPZ60R040C7 and dead time: the grid current in green, the grid voltage in red, and the DC voltage in blue.

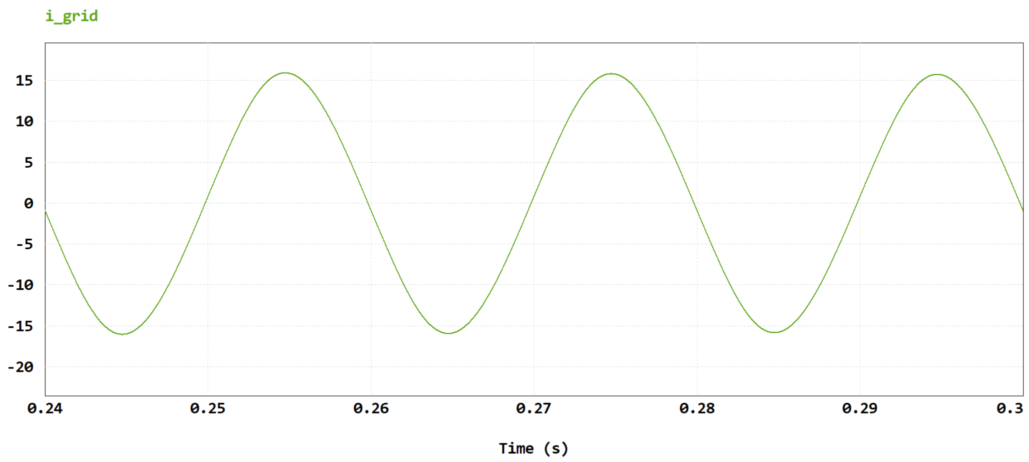

Figure 4.46: Current grid of the simulation with IPZ60R040C7 and dead time.

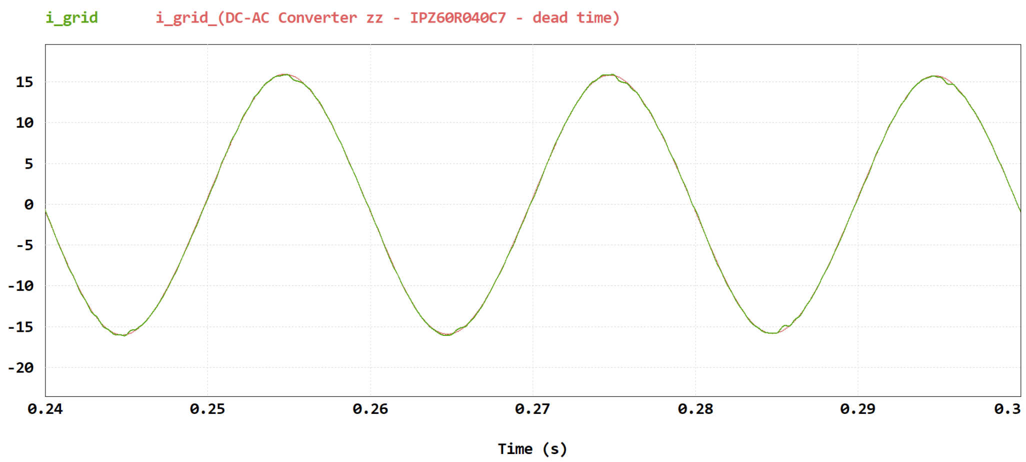

Figure 4.47: Comparison of the grid currents of the simulation with IPZ60R040C7 with dead time, in red, and without it, in green.

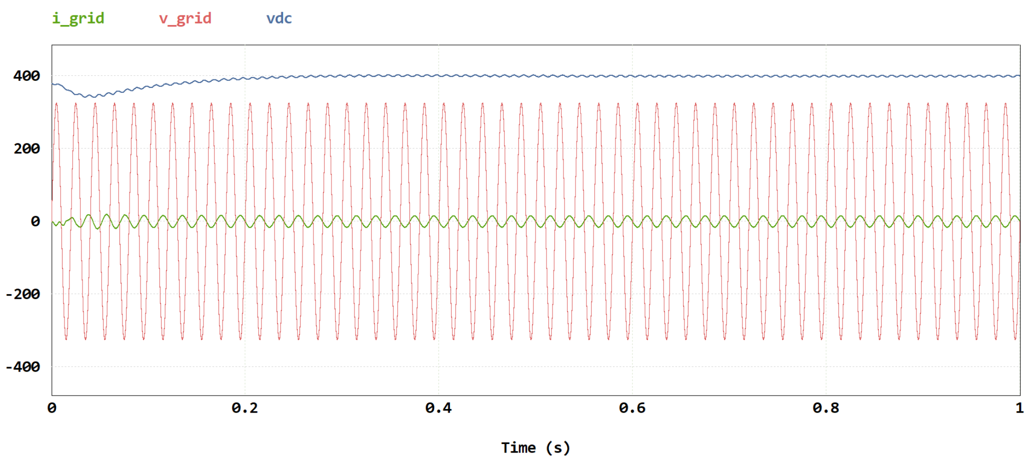

Figure 4.48: Waveforms of the analogue simulation with IXTH30N60L2: the grid current in green, the grid voltage in red, and the DC voltage in blue.

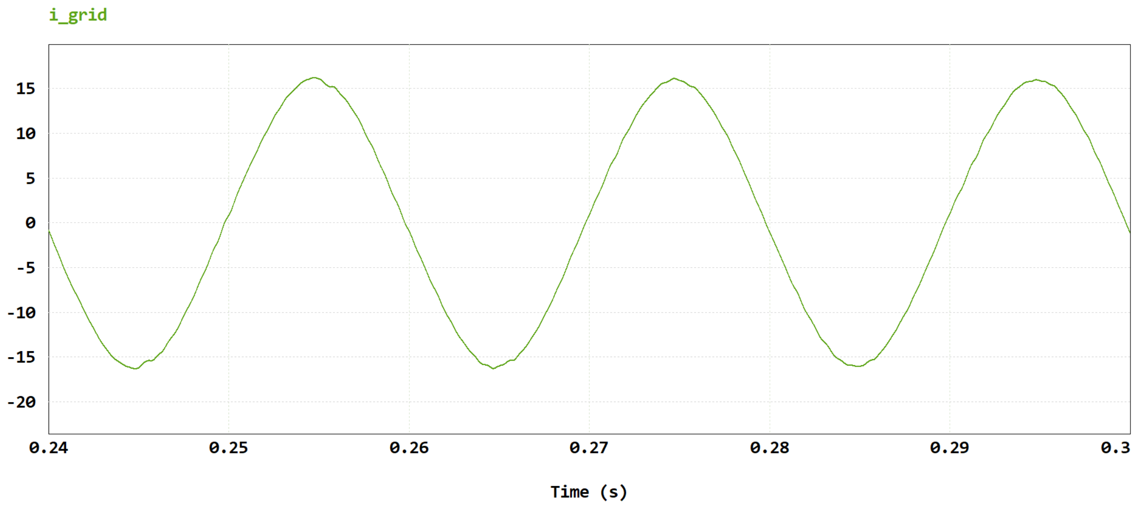

Figure 4.49: Current grid of the analogue simulation with IXTH30N60L2

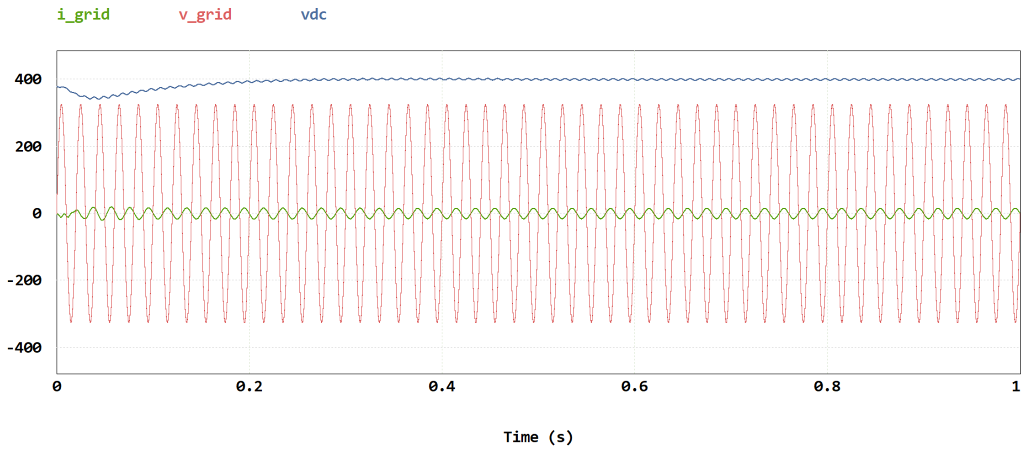

Figure 4.50: Waveforms of the analogue simulation with IXTH30N60L2 and dead time: the grid current in green, the grid voltage in red, and the DC voltage in blue.

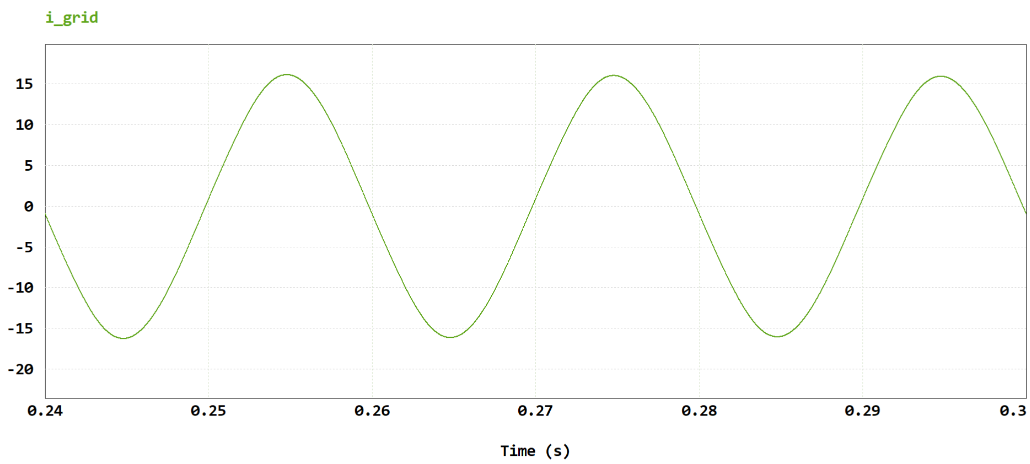

Figure 4.51: Current grid of the simulation with IXTH30N60L2 and dead time.

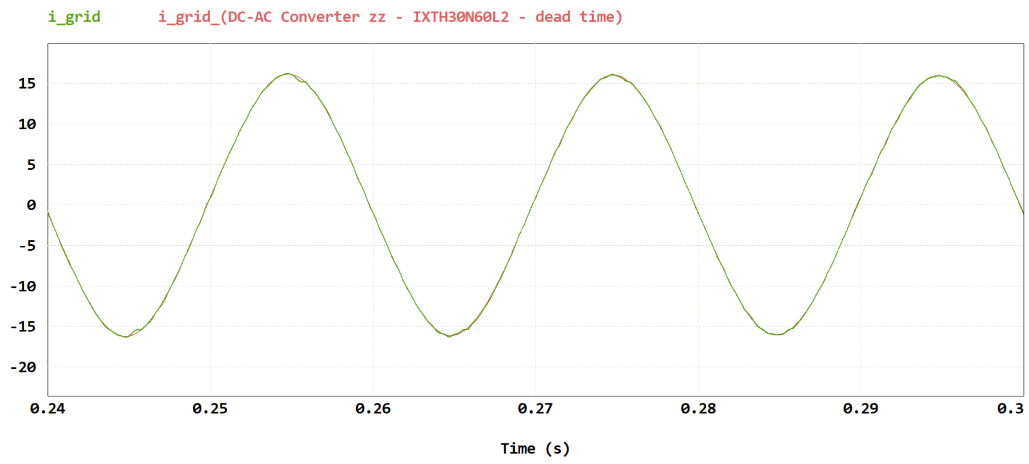

Figure 4.52: Comparison of the grid currents of the simulation with IXTH30N60L2 with dead time, in red, and without it, in green.

4.3 Simulations with Digital Control

4.3.1 Changes for the digital simulation

For the digital simulation, Zero-Order Holds (ZOH) were added to the control subcircuit to convert analogue waveforms into digital ones. The analogue PIs and integrators were converted to their digital counterparts using the bilinear (Tustin) transformation method. For the integrator, it went from

$$\frac{1}{s*T} \tag{4.17}$$

to

$$k_1 * \frac{T_s}{2} * \frac{1+z^{-1}}{1-z^{-1}} \tag{4.18}$$

where T is the time constant, T_s is the sampling time and k_1 is a constant that needs to be added to the digital integrator. For the PIs, it turns

$$k * \frac{1+s*T}{s*T} \tag{4.19}$$

into

$$k_1 + k_2 * \frac{T_s}{2} * \frac{1+z^{-1}}{1-z^{-1}} \tag{4.20}$$

where k is the value of the proportional component of the analogue PI and k_1 and k_2 correspond to the proportional and integral components of the digital PIs, respectively. The value of k_1 will be the same as the value of k and the value of k_2 will be the same as the value of $\frac{k}{T}$.

4.3.2 Case 1 - Normal Operation with Load

Using the circuit described in 4.2.1 and incorporating the digital transformations mentioned above, the waveforms depicted in Figure 4.53 were obtained.

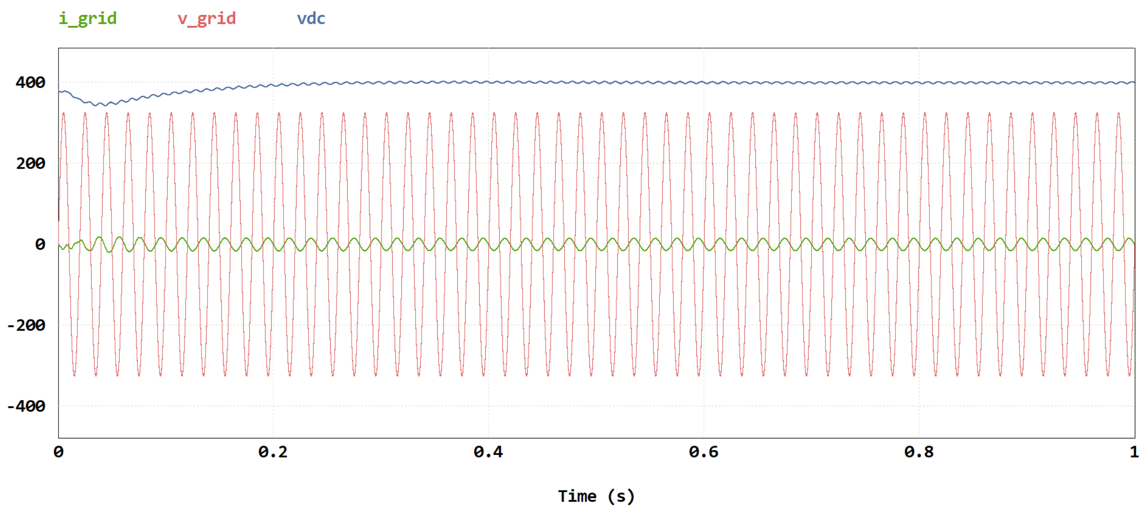

Figure 4.53: Waveforms for the normal operation with a load in the digital simulation: the grid current in green, the grid voltage in red, and the DC voltage in blue.

As depicted in Figure 4.53, the DC voltage stabilizes at 400V, and the grid current lags the grid voltage by 180º because it flows from the grid to the DC bus.

Figure 4.54 displays the harmonic spectrum of the grid current. Here, it can be observed that the results obtained in the digital simulation mirror those obtained in the analogue simulation.

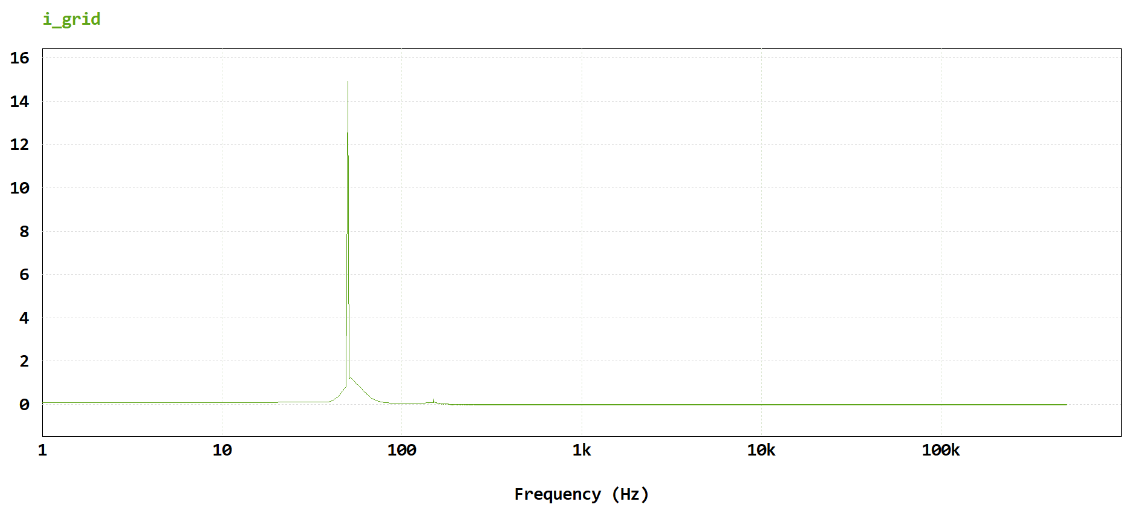

Figure 4.54: Harmonic spectrum of the grid current in the digital simulation.

4.3.3 Case 2 - Normal Operation with Current Source

Applying the same modifications described in 4.2.2 to the circuit, the waveforms depicted in Figure 4.55 were obtained.

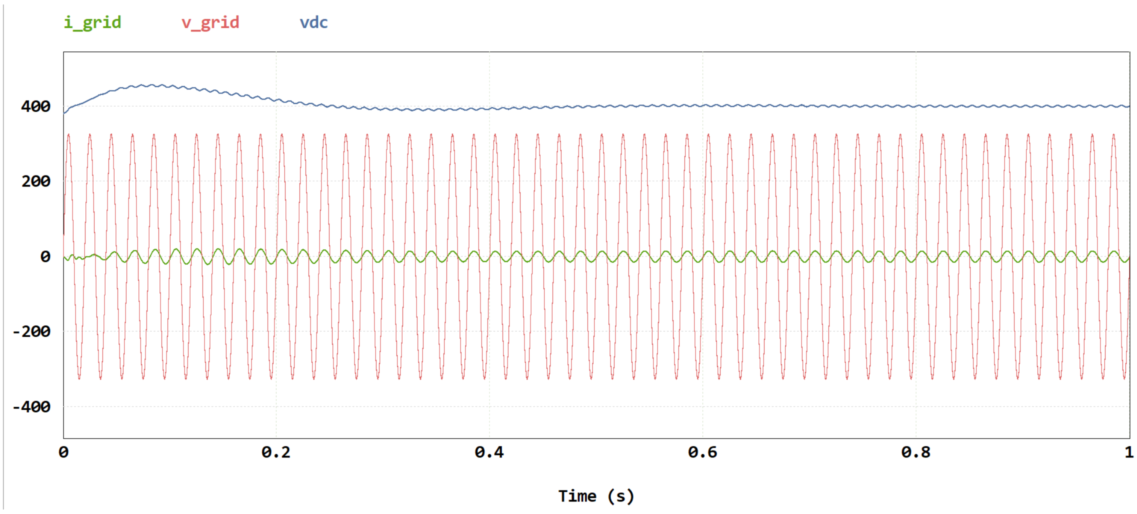

Figure 4.55: Obtained waveform for the normal operation with a current source in the digital simulation: the grid current in green, the grid voltage in red, and the DC voltage in blue.

Results similar to those described in 4.2.2 were achieved. The DC voltage stabilizes at 400V, and the grid current is in phase with the grid voltage because the current flows from the DC bus to the grid.

4.3.4 Case 3 - Operation with Alternate Load

Applying the same modifications as described in 4.2.3, the waveforms depicted in Figure 4.56 were obtained.

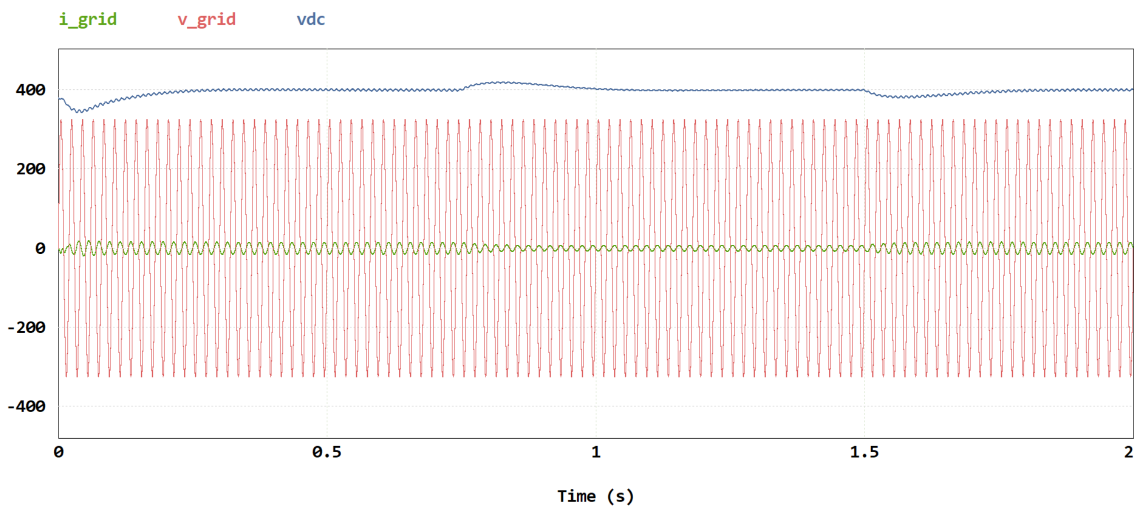

Figure 4.56: Waveforms for the operation with alternate load in digital simulation: the grid current in green, the grid voltage in red, and the DC voltage in blue.

Results similar to those described in 4.2.3 were achieved. With each change in the load, the DC voltage ends up stabilizing at 400V. The amplitude of the grid current varies correspondingly with changes in the load: decreasing when the load is increased and increasing when the load is decreased.

4.3.5 Case 4 - Operation with Alternate Reference Voltage

Implementing the identical modifications as described in 4.2.4, the waveforms depicted in Figure 4.57 were obtained.

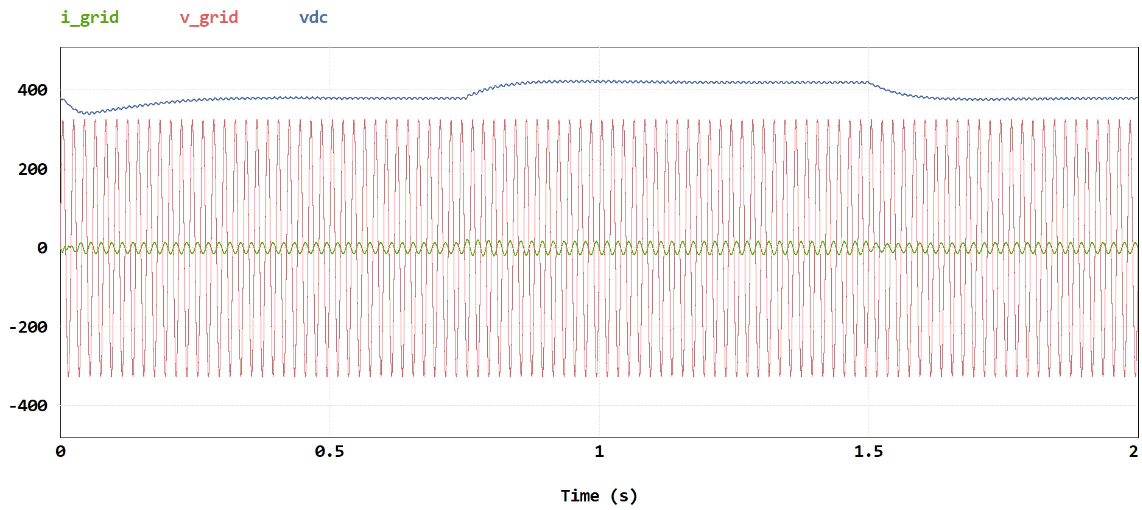

Figure 4.57: Waveforms for the operation with an alternate reference voltage in the digital simulation: the grid current in green, the grid voltage in red, and the DC voltage in blue.

Results similar to those described in 4.2.3 were achieved. With each change in the reference voltage for the DC bus (380V or 420V in this case), the DC voltage stabilizes at the specified reference value. The amplitude of the grid current varies accordingly with changes in the DC voltage: increasing when the DC voltage increases and decreasing when the DC voltage decreases.

4.3.6 Case 5 - Starting Operation

Similarly to 4.2.5, a resistor of $17,5\Omega$ was added on the grid side. This resistor will be bypassed by a switch when $t \geq 0,7$s. Additionally, a switch was introduced in the DC bus to simulate an open circuit when $t < 0,7$s and a load of 65Ω when $t \geq 0,7$s. Similar adjustments were made as in Figure 4.25 and Figure 4.30, and a circuit was added to control the switches (similar to the one shown in Figure 4.31).

The waveforms obtained in this simulation can be seen in Figure 4.58.

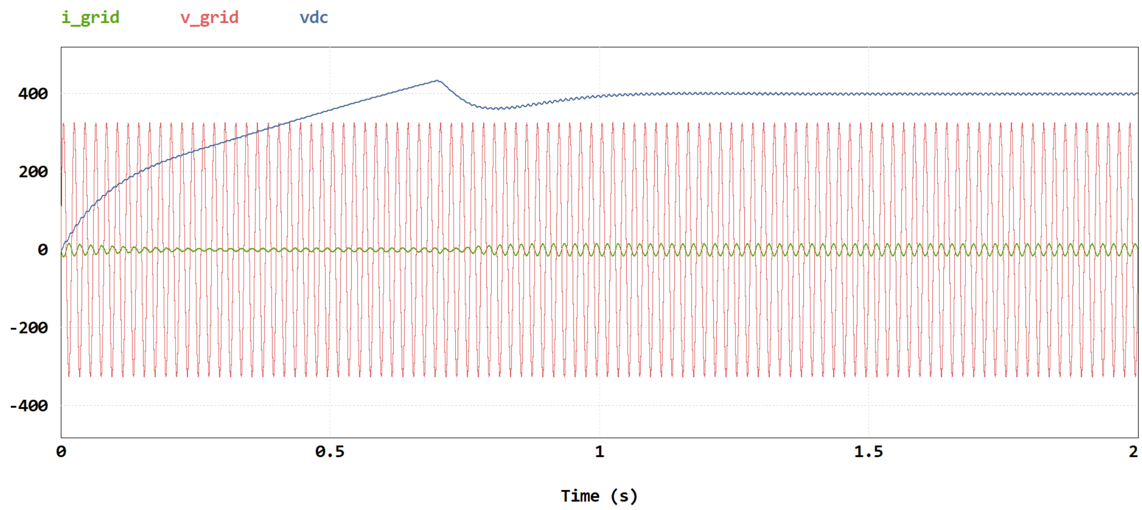

Figure 4.58: Waveforms for the starting operation in the digital simulation: the grid current in green, the grid voltage in red, and the DC voltage in blue.

As illustrated here, similar to 4.2.5, the grid current did not exhibit a spike at the beginning of the simulation. When $t \geq 0.7$s, the circuit operates under normal conditions with a load of 65Ω.

4.3.7 Case 6 - Simulations with IGBTs

This subsection employs non-ideal IGBTs for the simulations, replacing the ideal IGBTs.

4.3.7.1 Simulation with IKW30N60H3

Using the values in the datasheet [32], the circuit was simulated with four IKW30N60H3 instead of ideal IGBTs. The results are shown in Figure 4.59 and Figure 4.60.

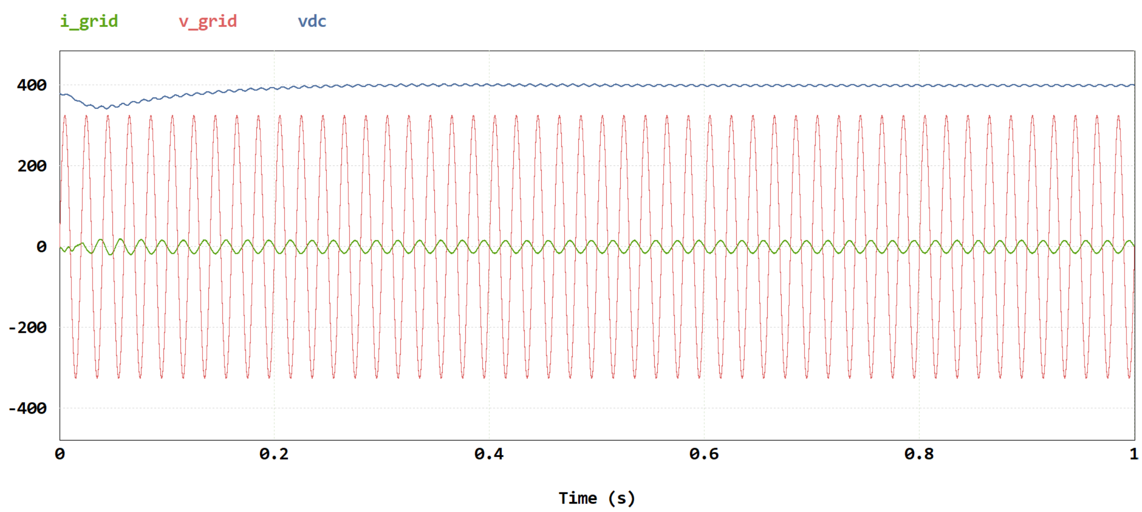

Figure 4.59: Waveforms of the digital simulation with IKW30N60H3: the grid current in green, the grid voltage in red, and the DC voltage in blue.

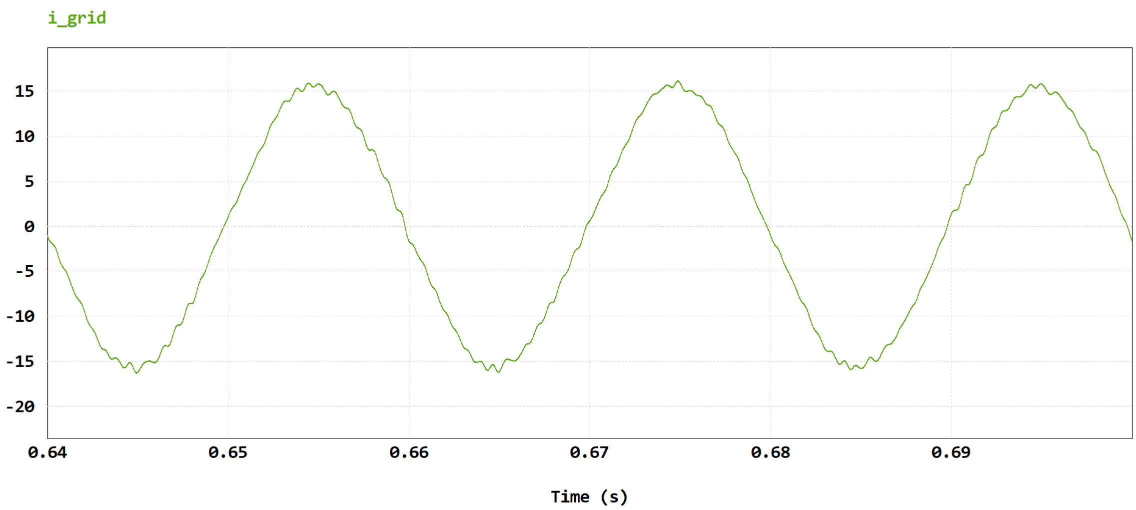

Figure 4.60: Current grid of the digital simulation with IKW30N60H3

In Figure 4.60, it can be seen, like with analogue simulations, that the waveform is distorted.

Using the formula 4.16, the dead time was obtained and with it, the results shown in Figures 4.61 and 4.62 were obtained.

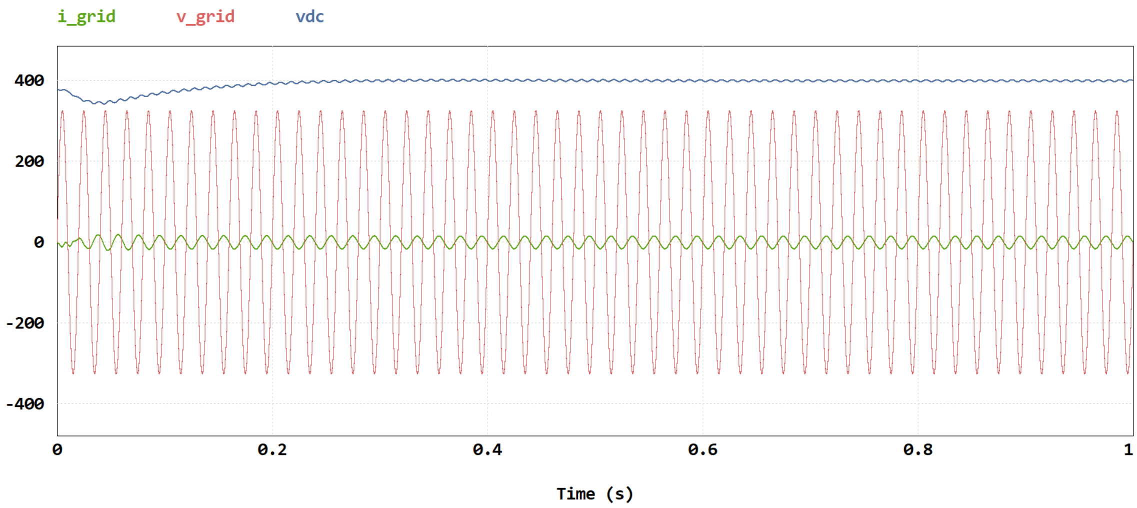

Figure 4.61: Waveforms of the digital simulation with IKW30N60H3 and dead time: the grid current in green, the grid voltage in red, and the DC voltage in blue.

In Figure 4.62, it can be seen that the distortion has greatly diminished in comparison with before. Figure 4.63 provides a clearer view by displaying the currents both with and without dead time.

4.3.7.2 Simulation with BIDNW30N60H3

Using the values in the datasheet [34], the circuit was simulated with four BIDNW30N60H3 instead of ideal IGBTs. The results are shown in Figure 4.64 and Figure 4.65.

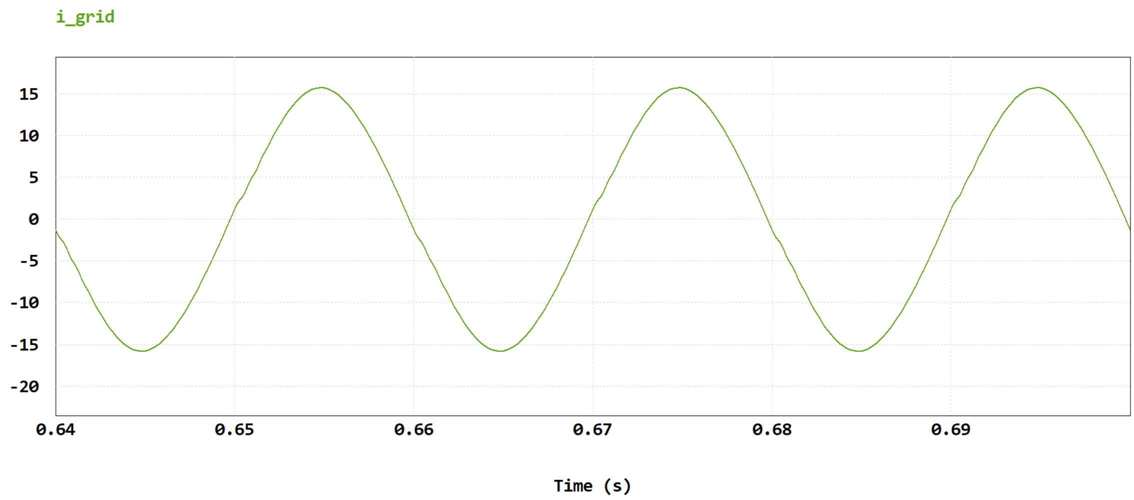

Figure 4.62: Current grid of the simulation with IKW30N60H3 and dead time.

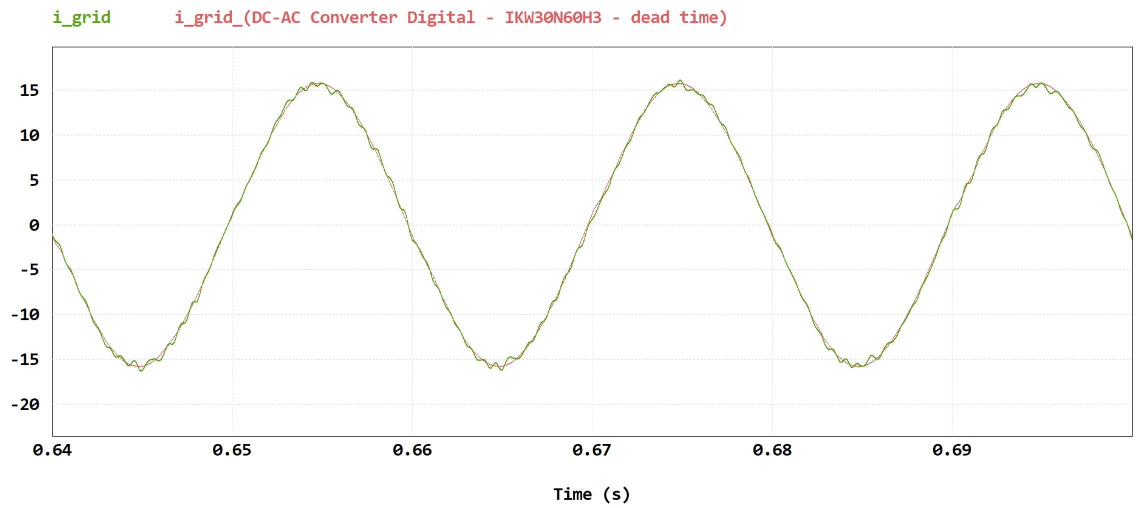

Figure 4.63: Comparison of the grid currents of the simulation with IKW30N60H3 with dead time, in red, and without it, in green.

In Figure 4.65, it can be seen that, like with IKW30N60H3, the waveform shows distortions in the waveform.

Adding dead time and simulating with it, the results shown in Figures 4.66 and 4.67 were obtained.

In Figure 4.67, it can be seen that the distortion has greatly diminished in comparison with before. Figure 4.68 provides a clearer view by displaying the currents both with and without dead time.

4.3.8 Case 7 - Simulations with MOSFETs

This subsection employs non-ideal MOSFETs for the simulations, replacing the ideal IGBTs.

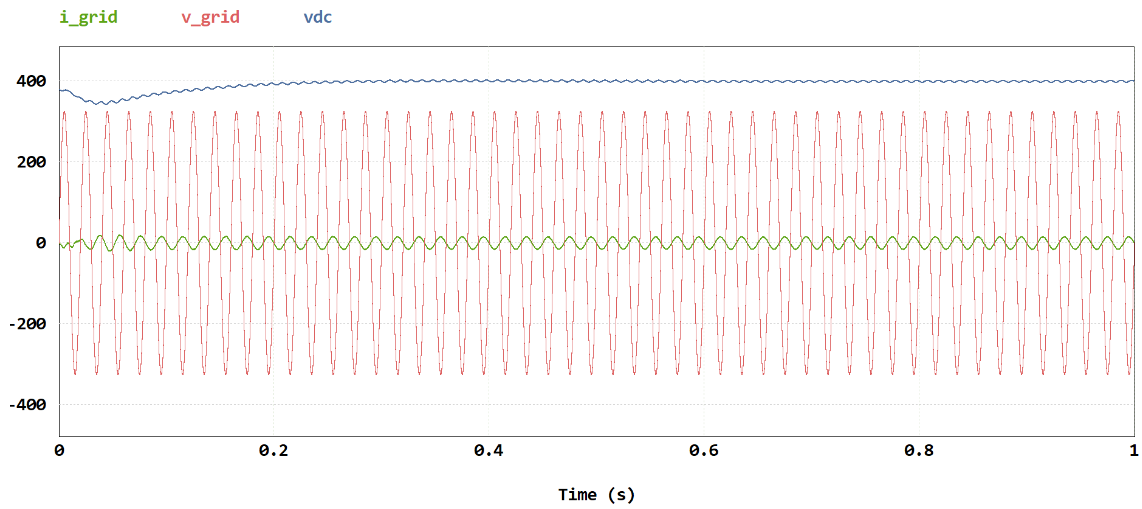

Figure 4.64: Waveforms of the digital simulation with BIDNW30N60H3: the grid current in green, the grid voltage in red, and the DC voltage in blue.

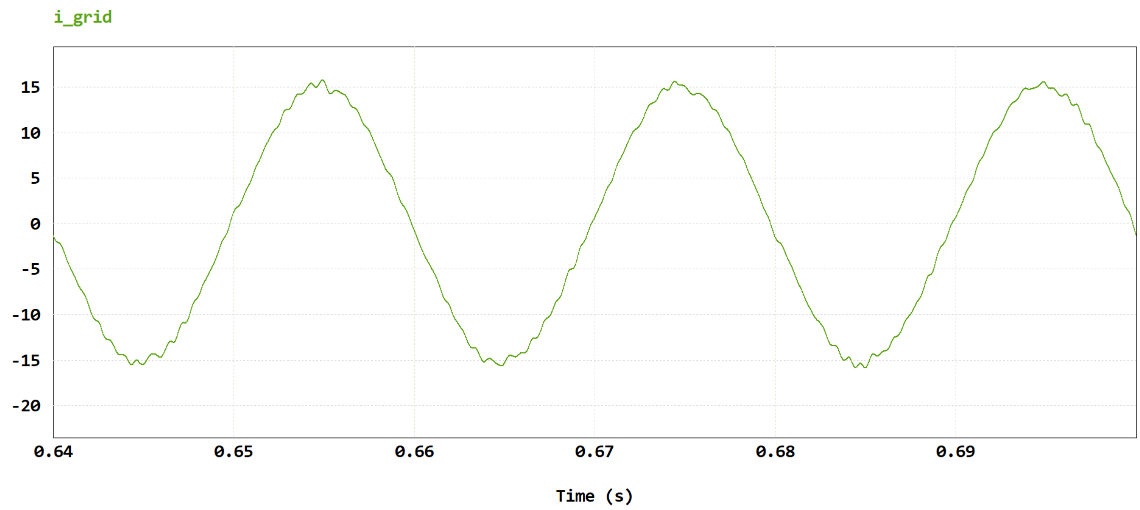

Figure 4.65: Current grid of the digital simulation with BIDNW30N60H3

4.3.8.1 Simulation with IPZ60R040C7

Using the values in the datasheet [35], the circuit was simulated with four IPZ60R040C7 instead of ideal IGBTs. The results are shown in Figure 4.69 and Figure 4.70.

In Figure 4.70, it can be seen that, like for the IGBTs, the waveform shows distortions in the waveform.

Adding dead time and simulating with it, the results shown in Figures 4.71 and 4.72 were obtained.

In Figure 4.72, it can be seen that the distortion has greatly diminished in comparison with before. Figure 4.73 provides a clearer view by displaying the currents both with and without dead time.

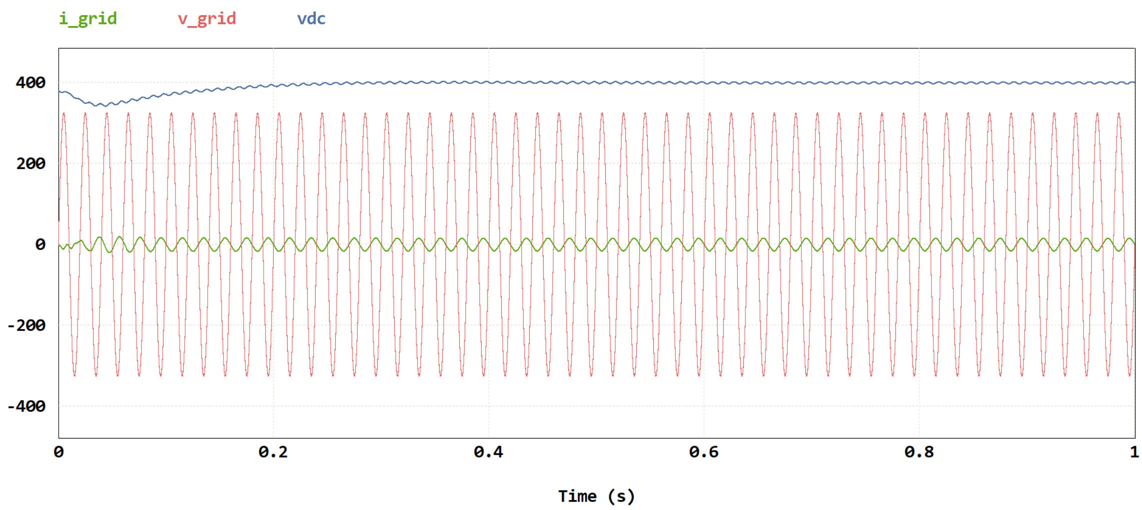

Figure 4.66: Waveforms of the digital simulation with BIDNW30N60H3 and dead time: the grid current in green, the grid voltage in red, and the DC voltage in blue.

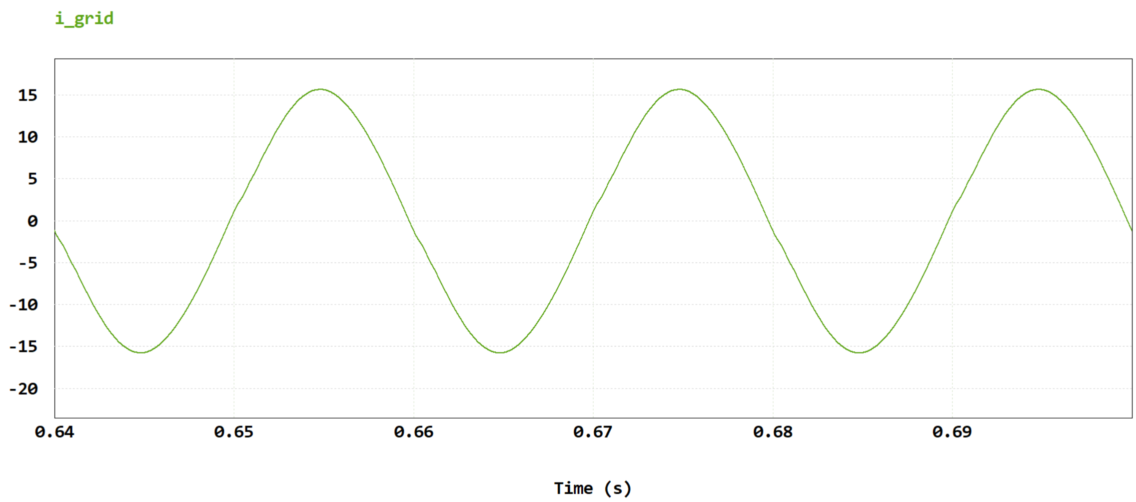

Figure 4.67: Current grid of the simulation with BIDNW30N60H3 and dead time.

4.3.8.2 Simulation with IXTH30N60L2

Using the values in the datasheet [36], the circuit was simulated with four IXTH30N60L2 instead of ideal IGBTs. The results are shown in Figure 4.74 and Figure 4.75.

In Figure 4.75, it can be seen that, like for the IPZ60R040C7, the waveform shows distortions in the waveform.

Adding dead time and simulating with it, the results shown in Figures 4.76 and 4.77 were obtained.

In Figure 4.77, it can be seen that the distortion has greatly diminished in comparison with before. Figure 4.78 provides a clearer view by displaying the currents with and without dead time.

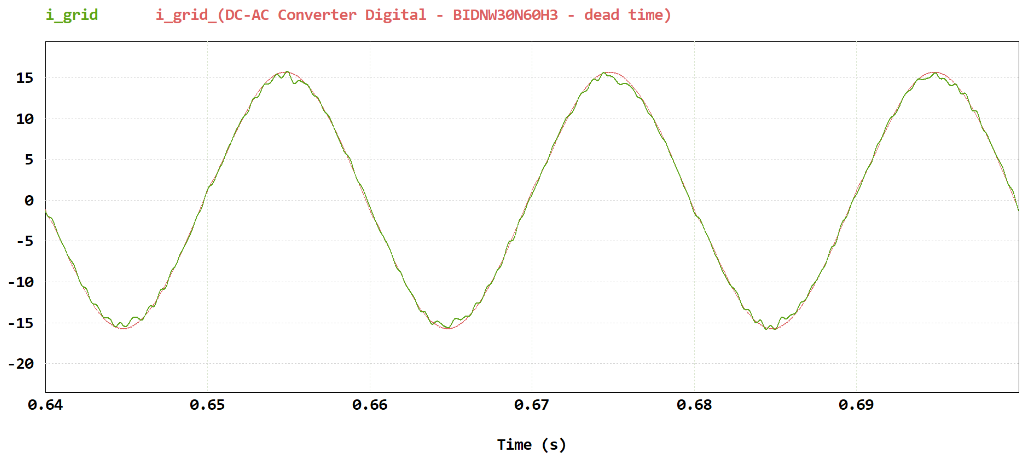

Figure 4.68: Comparison of the grid currents of the simulation with BIDNW30N60H3 with dead time, in red, and without it, in green.

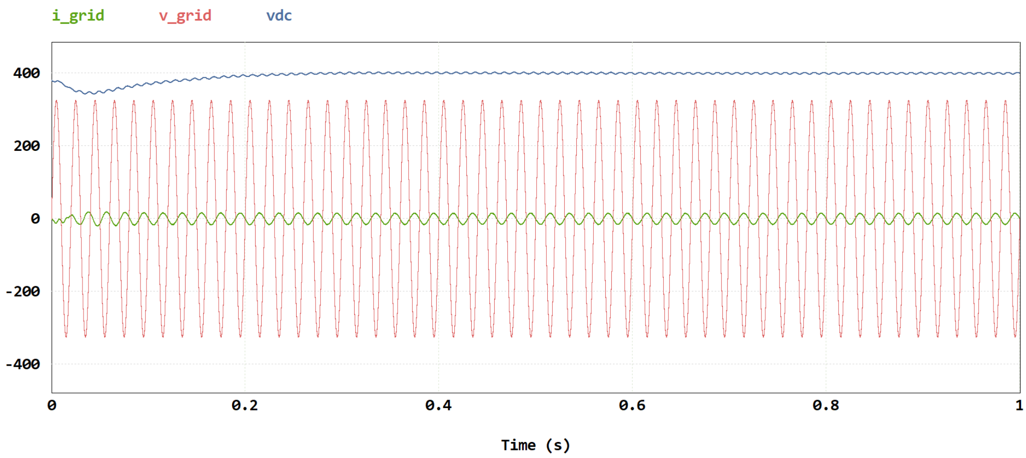

Figure 4.69: Waveforms of the digital simulation with IPZ60R040C7: the grid current in green, the grid voltage in red, and the DC voltage in blue.

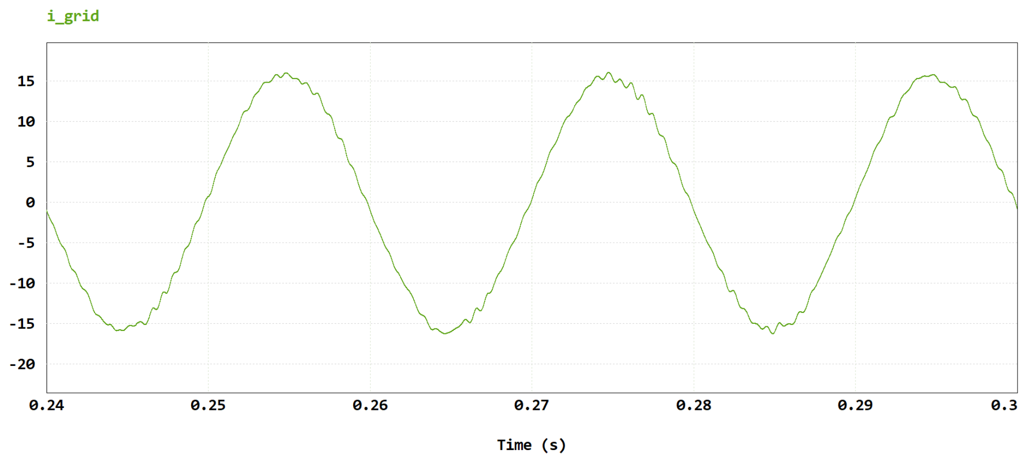

Figure 4.70: Current grid of the digital simulation with IPZ60R040C7

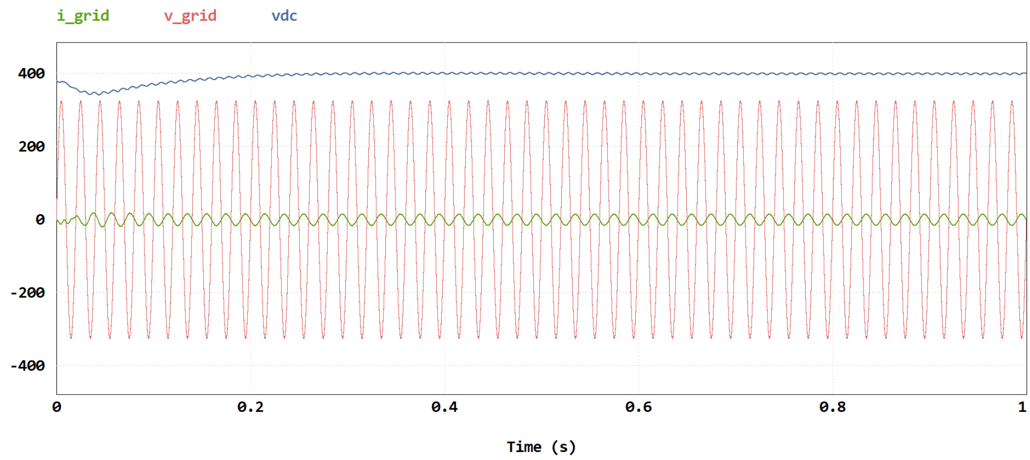

Figure 4.71: Waveforms of the digital simulation with IPZ60R040C7 and dead time: the grid current in green, the grid voltage in red, and the DC voltage in blue.

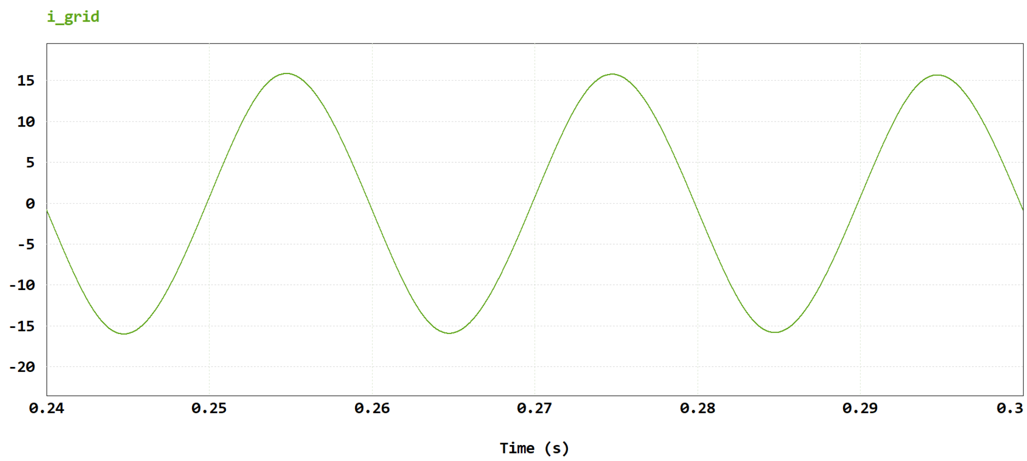

Figure 4.72: Current grid of the simulation with IPZ60R040C7 and dead time.

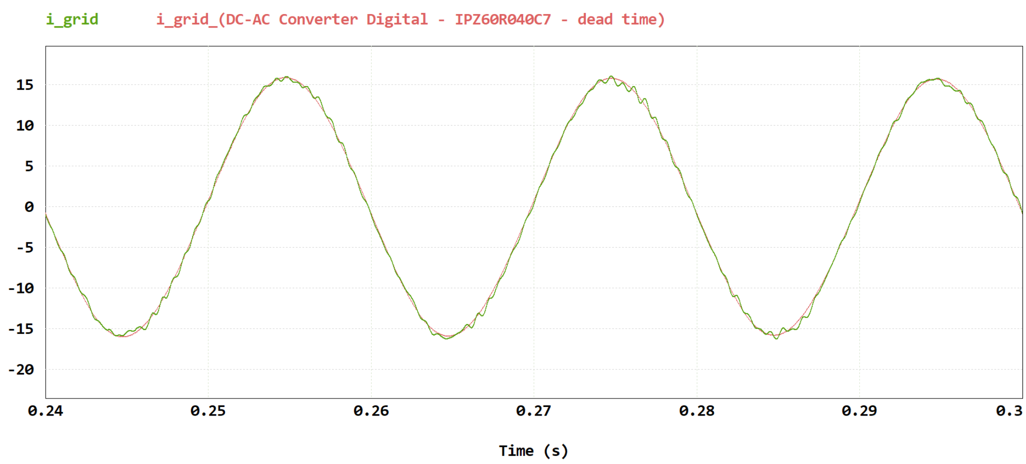

Figure 4.73: Comparison of the grid currents of the simulation with IPZ60R040C7 with dead time, in red, and without it, in green.

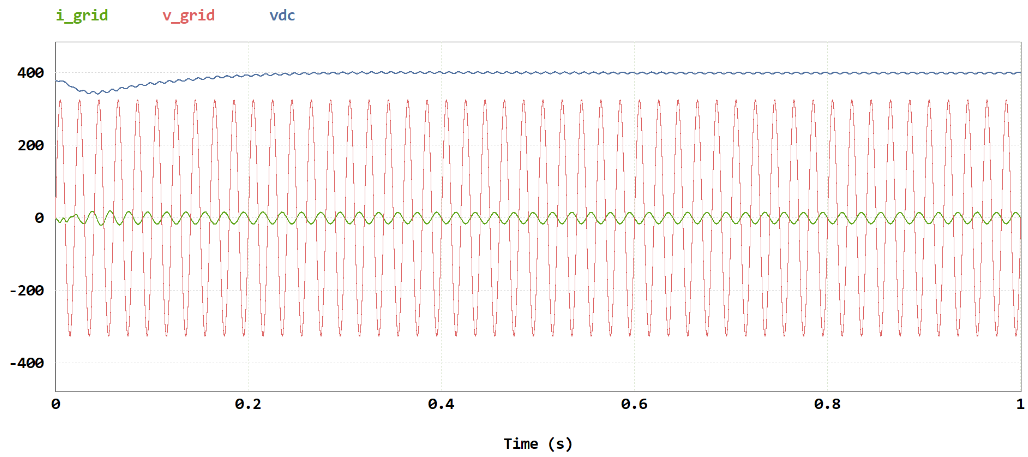

Figure 4.74: Waveforms of the digital simulation with IXTH30N60L2: the grid current in green, the grid voltage in red, and the DC voltage in blue.

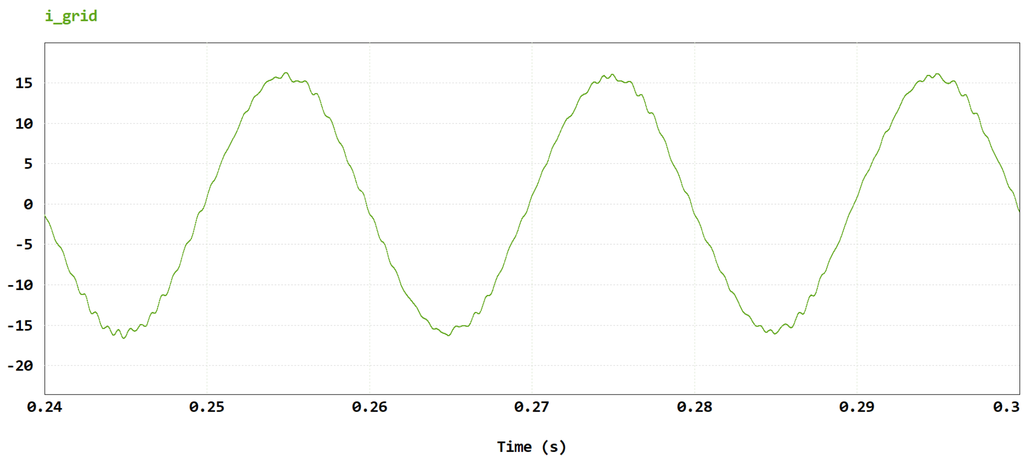

Figure 4.75: Current grid of the digital simulation with IXTH30N60L2

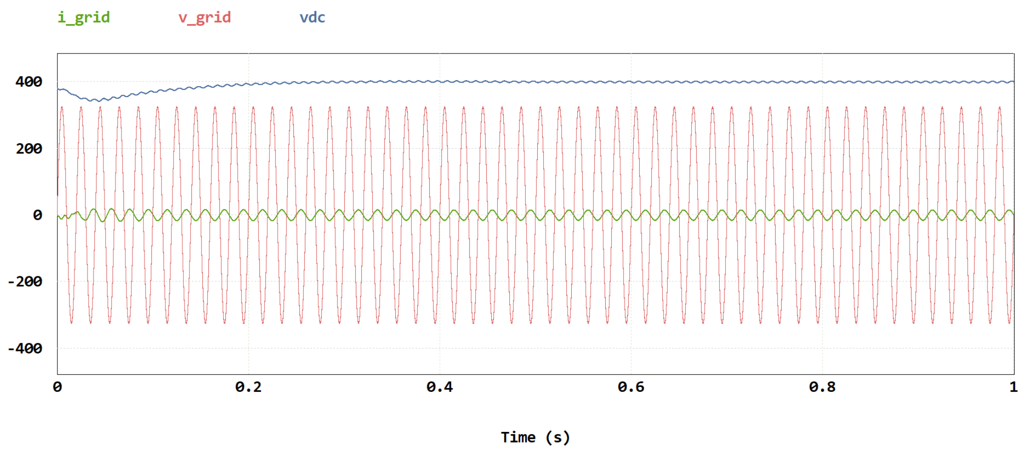

Figure 4.76: Waveforms of the digital simulation with IXTH30N60L2 and dead time: the grid current in green, the grid voltage in red, and the DC voltage in blue.

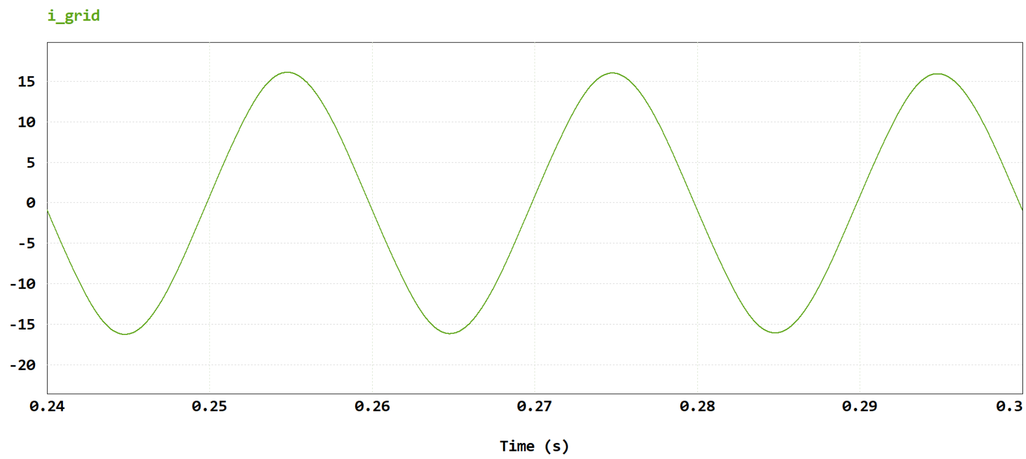

Figure 4.77: Current grid of the simulation with IXTH30N60L2 and dead time.

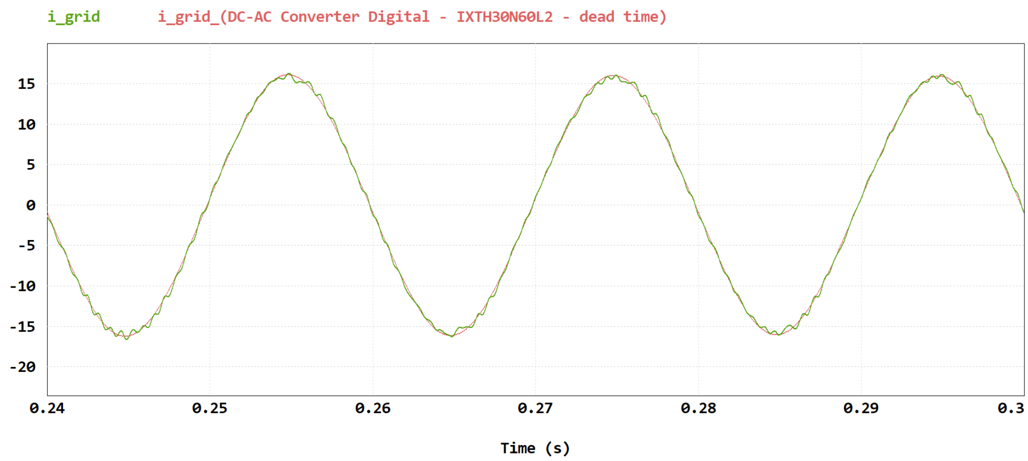

Figure 4.78: Comparison of the grid currents of the simulation with IXTH30N60L2 with dead time, in red, and without it, in green.

4.4 Analysis and Comparison of the Results

In this section, the results of the simulations will be compared and analysed.

4.4.1 IGBT vs MOSFET

Here, the simulations with IGBTs will be compared with the simulations with MOSFETs to decide which of the two is better for the converter.

4.4.1.1 Advantages and Disadvantages of IGBTs and MOSFETs

MOSFETs are renowned for their efficiency in switching and amplification, making them popular for low- and medium-power applications. Their appeal lies in their fast switching capabilities and ease of control. Meanwhile, IGBTs combine the high-voltage capabilities of bipolar junction transistors (BJTs) with MOSFETs' rapid switching speeds and low input power requirements.

As illustrated in Figure 4.79, both MOSFETs and IGBTs are viable options for converters operating at a switching frequency of 10 kHz and an output capacity of $3,680 KVA$. Table 4.1 summarises the features of both IGBTs and MOSFETs. The table highlights that IGBTs offer advantages in high voltage and current capacity but suffer from slower switching speeds and higher losses. Conversely, MOSFETs excel in fast switching, though they incur higher conduction losses at high voltages.

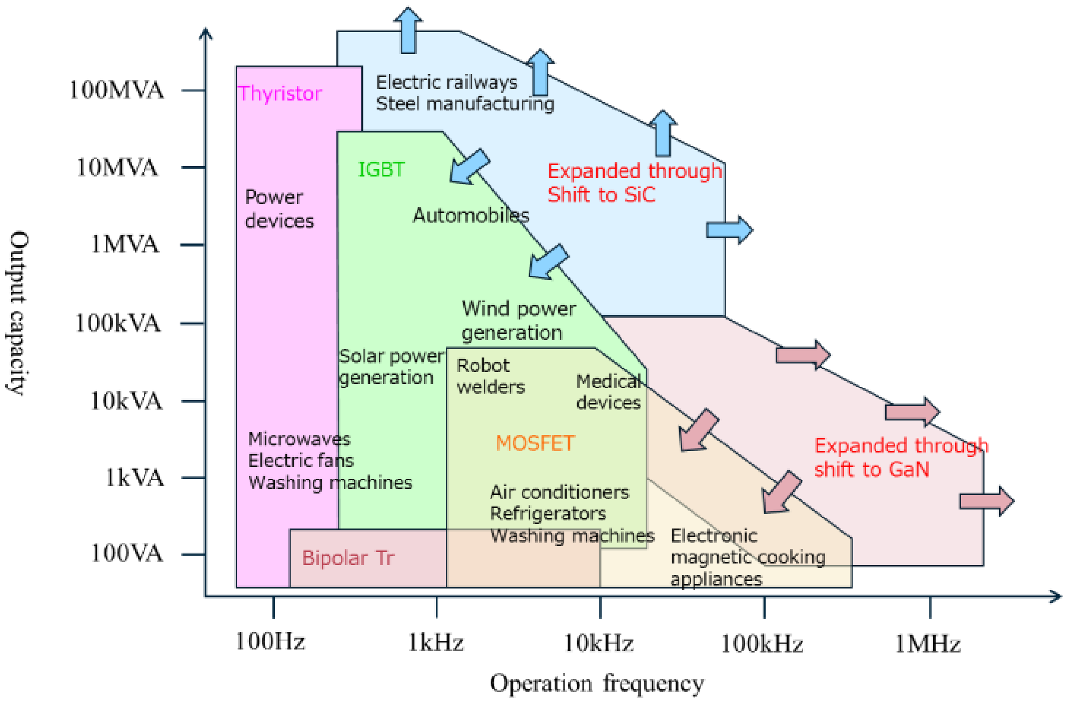

Figure 4.79: Range of Operation of several switching transistors.

Table 4.1: Comparison between IGBT and MOSFET.

Feature	IGBT	MOSFET
Voltage Range	600V - 6,5kV	20V - 1000V
Current Range	High (hundreds of amps)	Moderate to high (tens to hundreds)
Switching Speed	Moderate (up to 50kHz, with some going up to 100kHz like IXYS IXGH30N60C3D1)	High (up to MHz range)
Conduction Losses	Lower (due to lower collector-emitter saturation voltage ($V_{CE(sat)}$))	Higher (due to drain-source on-state resistance ($R_{DS(on)}$))
Switching Losses	Higher (slower switching)	Lower (faster switching)

4.4.1.2 Simulations Comparison

Here, the waveforms obtained from IGBTs and MOSFETs simulations will be compared.

Figure 4.80 is the comparison between the grid currents of the IGBT IKW30N60H3 and the MOSFET IPZ60R040C7. Here, it can be seen that both waveforms are very similar, with the IKW30N60H3 having a higher amplitude than the IPZ60R040C7.

Figure 4.81 is the comparison between the DC voltage of the IGBT IKW30N60H3 and the MOSFET IPZ60R040C7. Here, it can be seen that before $t = 0,16s$ the value of the amplitude of the IPZ60R040C7 is higher than the one from IKW30N60H3. After $t = 0,16s$ the waveform of IKW30N60H3 is the same as the one from IPZ60R040C7.

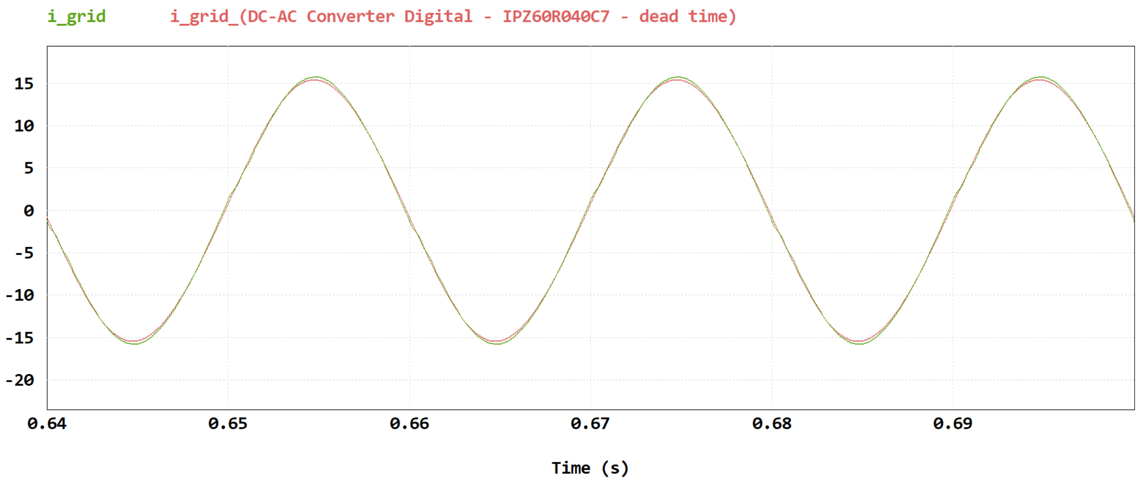

Figure 4.80: Comparison between the grid currents obtained from IKW30N60H3, in green, and IPZ60R040C7, in red

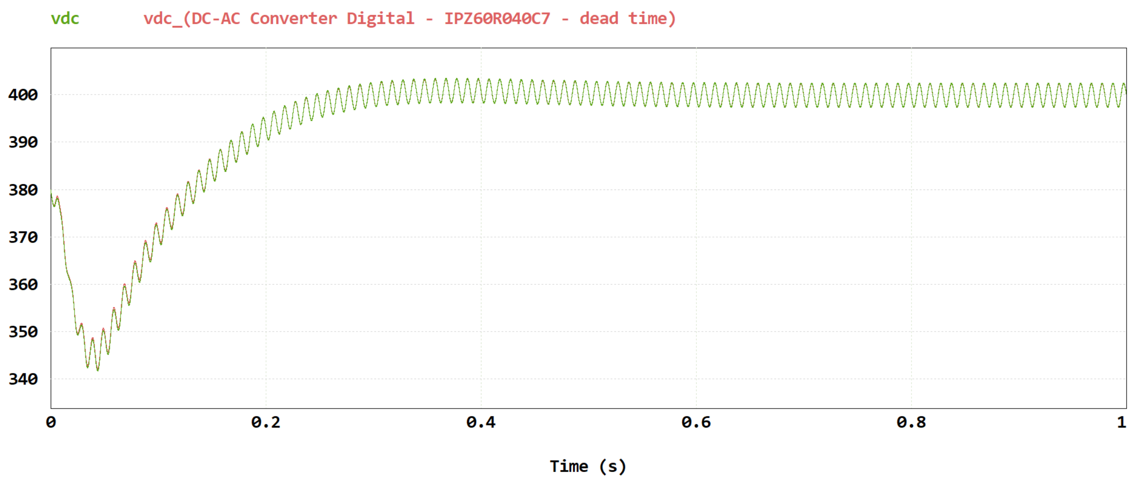

Figure 4.81: Comparison between the DC voltage obtained from IKW30N60H3, in green, and IPZ60R040C7, in red

Figure 4.82 is the comparison between the IGBT IKW30N60H3 and the MOSFET IXTH30N60L2. Here, it can be seen that both waveforms are almost the same, with the differences being almost negligible.

Figure 4.83 is the comparison between the DC voltage of the IGBT IKW30N60H3 and the MOSFET IXTH30N60L2. Here, it can be seen that before $t = 0,07s$ the value of the amplitude of the IXTH30N60L2 is higher than the one from IKW30N60H3. After $t = 0,07s$ the waveform of IKW30N60H3 is the same as the one from IXTH30N60L2.

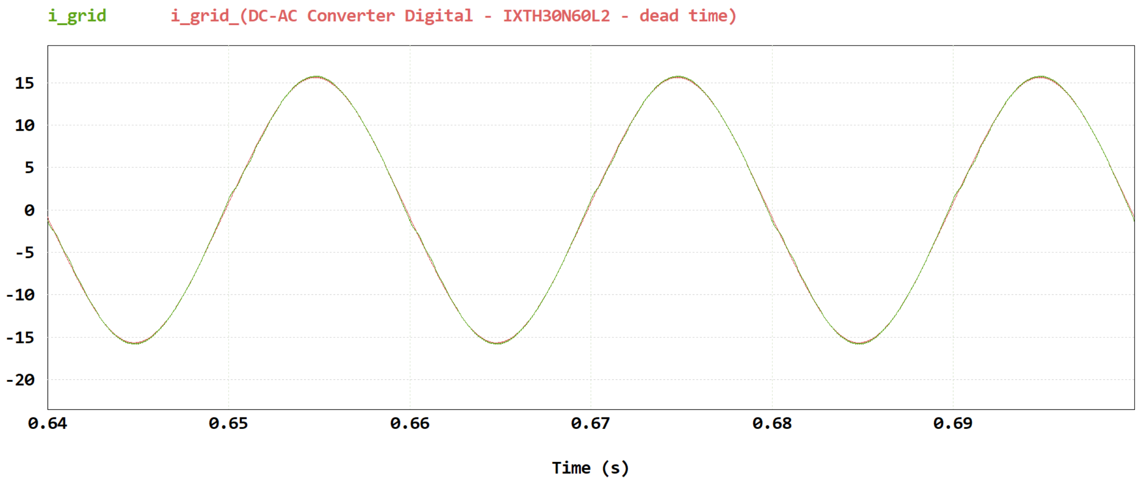

Figure 4.82: Comparison between the grid currents obtained from IKW30N60H3, in green, and IXTH30N60L2, in red

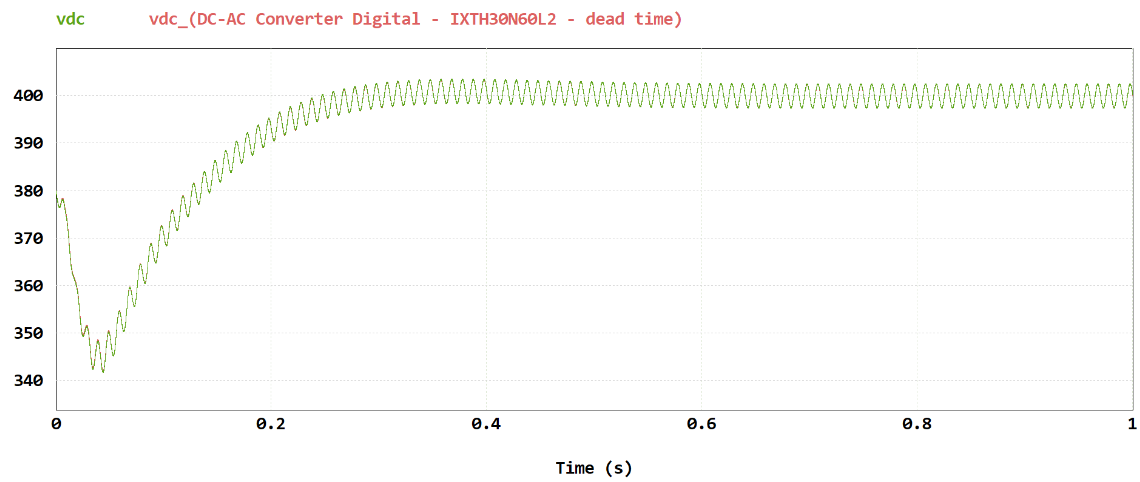

Figure 4.83: Comparison between the DC voltage obtained from IKW30N60H3, in green, and IXTH30N60L2, in red

Figure 4.84 is the comparison between the IGBT BIDNW30N60H3 and the MOSFET IPZ60R040C7. Here, it can be seen that both waveforms are almost the same, with the difference being that the amplitude of the waveform of BIDNW30N60H3 is slightly bigger than the waveform of IPZ60R040C7.

Figure 4.85 is the comparison between the DC voltage of the IGBT BIDNW30N60H3 and the MOSFET IPZ60R040C7. Here, it can be seen that before $t = 0,1s$ the value of the amplitude of the IPZ60R040C7 is higher than the one from BIDNW30N60H3. After $t = 0,1s$ the waveform of BIDNW30N60H3 is the same as the one from IPZ60R040C7.

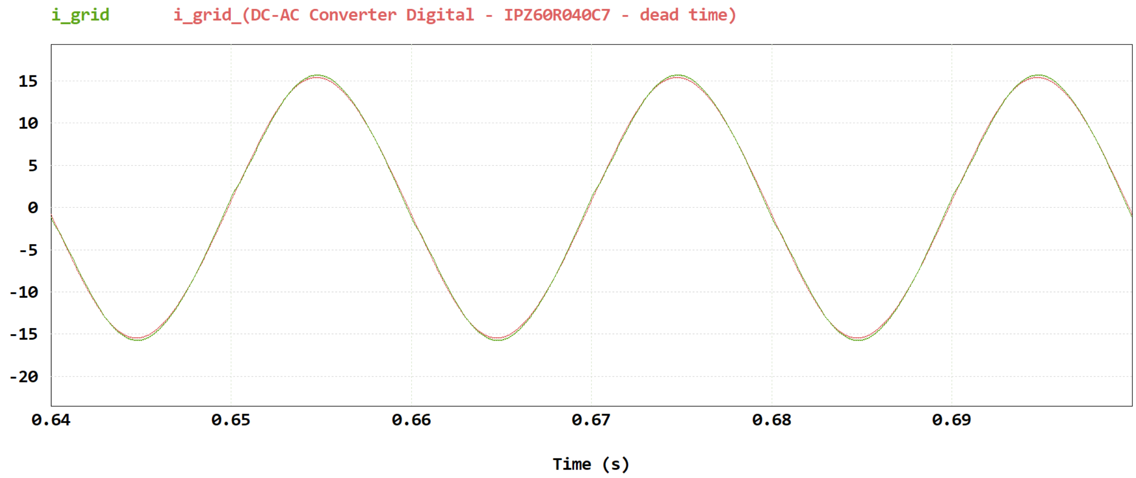

Figure 4.84: Comparison between the grid currents obtained from BIDNW30N60H3, in green, and IPZ60R040C7, in red

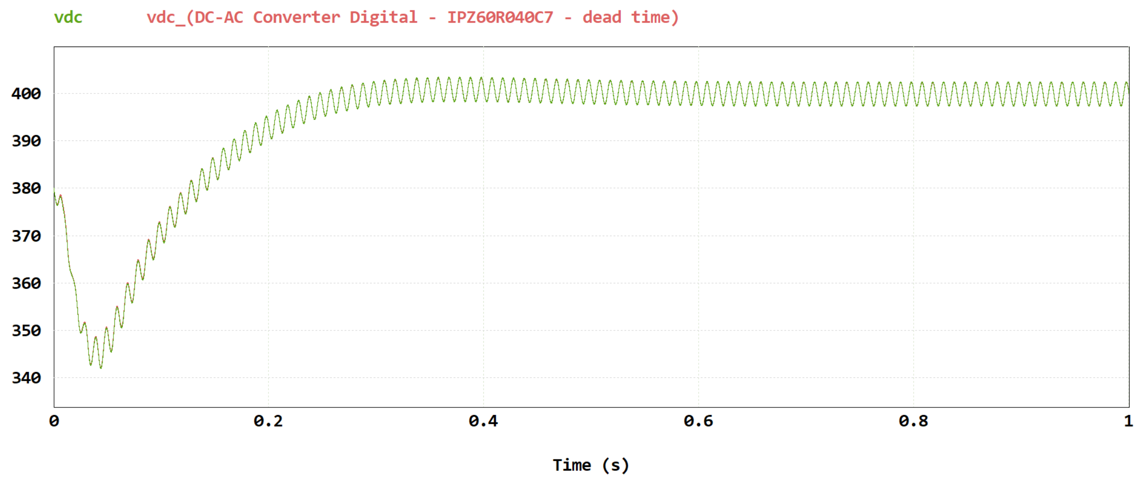

Figure 4.85: Comparison between the DC voltage obtained from BIDNW30N60H3, in green, and IPZ60R040C7, in red

Figure 4.86 is the comparison between the IGBT BIDNW30N60H3 and the MOSFET IXTH30N60L2.Here, it can be seen that both waveforms are almost the same, with the differences being almost negligible.

Figure 4.87 is the comparison between the DC voltage of the IGBT BIDNW30N60H3 and the MOSFET IXTH30N60L2. Here, it can be seen that before $t = 0,1s$ the value of the amplitude of the IXTH30N60L2 is higher than the one from BIDNW30N60H3. After $t = 0,1s$ the waveform of BIDNW30N60H3 is the same as the one from IXTH30N60L2.

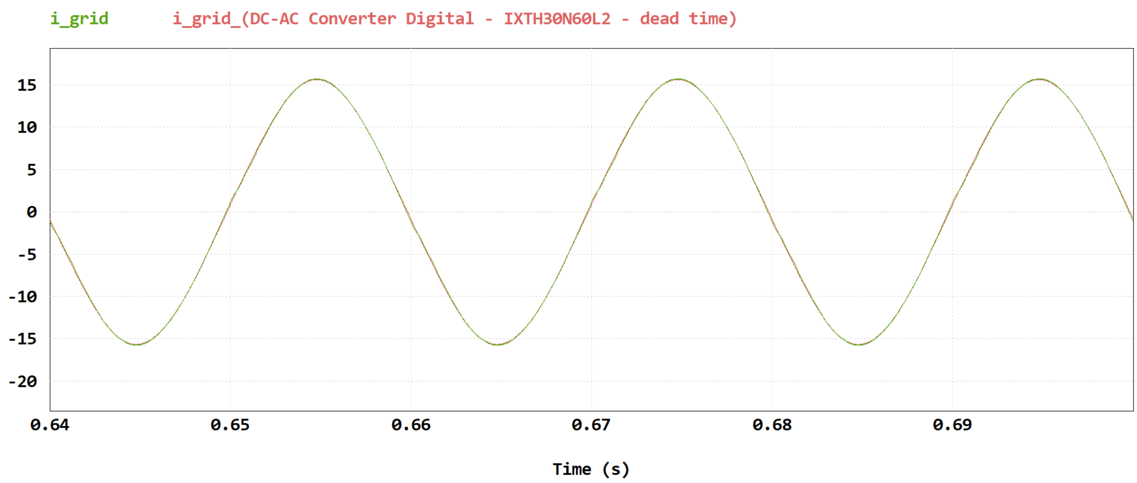

Figure 4.86: Comparison between the grid currents obtained from BIDNW30N60H3, in green, and IXTH30N60L2, in red

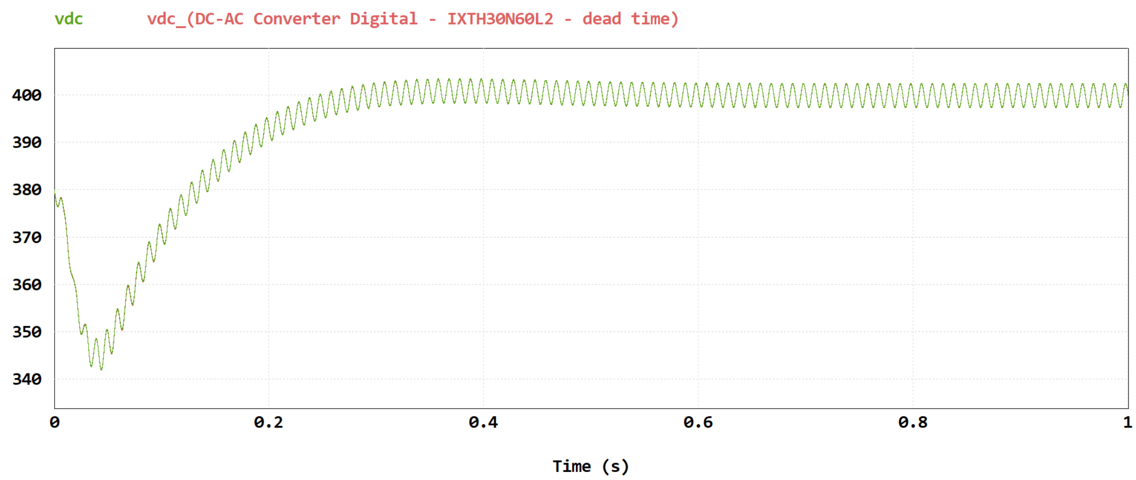

Figure 4.87: Comparison between the DC voltage obtained from BIDNW30N60H3, in green, and IXTH30N60L2, in red

4.4.1.3 Results Discussion

Based on the simulations, the DC voltage waveforms between IGBTs and MOSFETs exhibit minor differences, primarily noticeable at the waveform's onset. However, the most significant distinction lies in the grid current, where IGBTs generally showed higher absolute amplitudes compared to MOSFETs, except for the IGBT BIDNW30N60H3, which yielded results close to those of MOSFETs.

The primary differentiating factor between the used IGBTs and MOSFETs ultimately comes down to cost. The prices for the components are as follows: IKW30N60H3 costs 3.07€ [37], BIDNW30N60H3 costs 3.49€ [38], IPZ60R040C7 costs 7.60€ [39], and IXTH30N60L2 costs 18.42€ [40]. Considering these prices and the simulation results, the IGBT BIDNW30N60H3 appears to be the optimal choice for the converter application.

4.4.2 Analogue vs Digital

Here, the results of the analogue simulations will be compared with their digital counterparts for each respective case.

4.4.2.1 Comparison of Case 1

The waveforms obtained from both the analogue and digital simulations for case 1 were highly similar to each other, as depicted in Figure 4.88 and Figure 4.89.

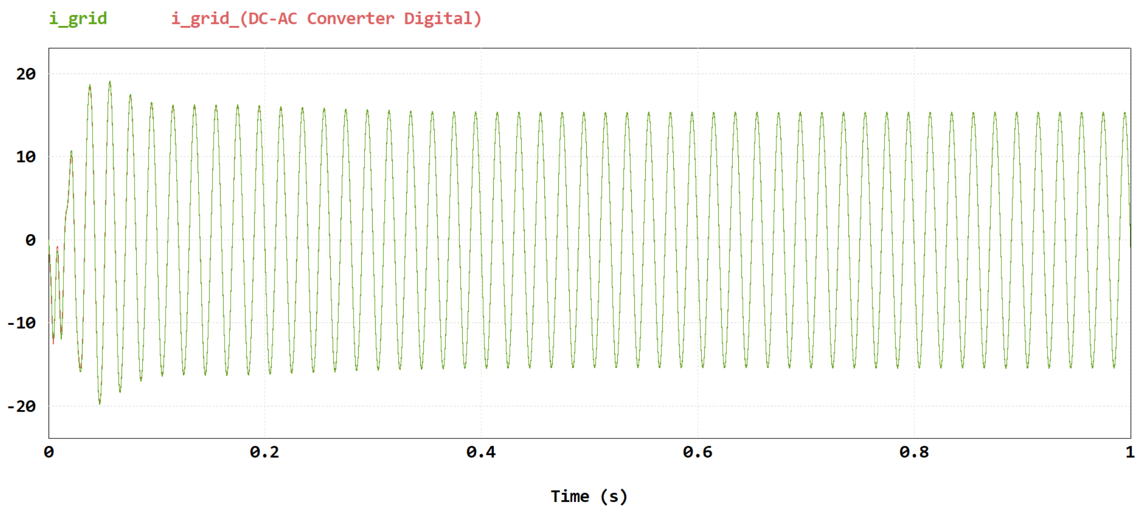

Figure 4.88: Comparison between the grid current of the analogue simulation, in green, and the grid current of the digital simulation, in red, for case 1.

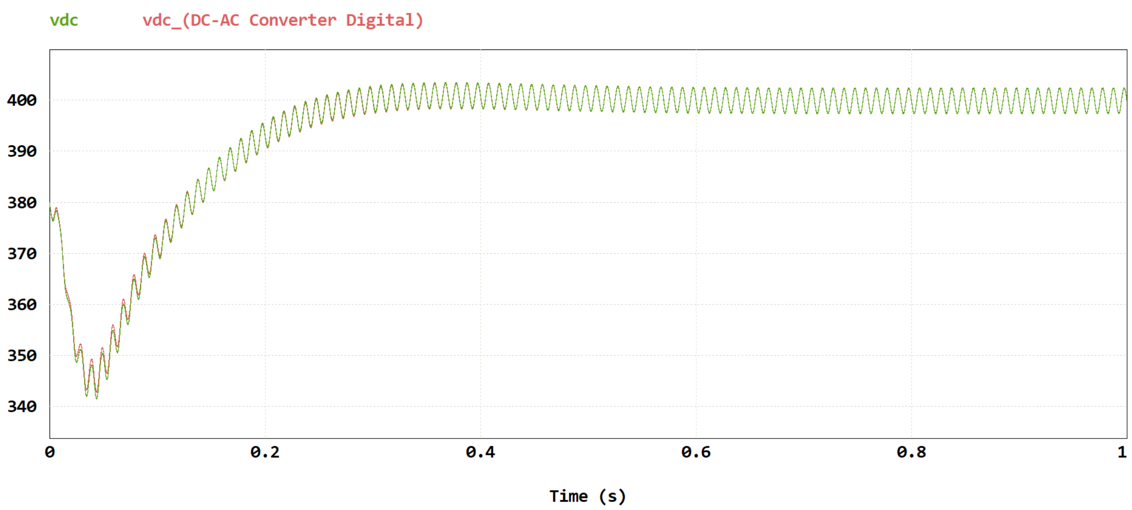

Figure 4.89: Comparison between the DC voltage of the analogue simulation, in green, and the DC voltage of the digital simulation, in red, for case 1.

Figure 4.90 shows a zoomed version of the initial deciseconds of the Figure 4.88, and here it can be seen that from $0s$ to $0,015s$ the absolute value of the amplitude of the current of the digital simulation is bigger than the one from the analogue simulation, from $0,015s$ to $0,1s$ the absolute value of the amplitude of the current in the digital simulation is lower compared to the one from the analogue simulation. After $0,1s$, both waveforms align closely.

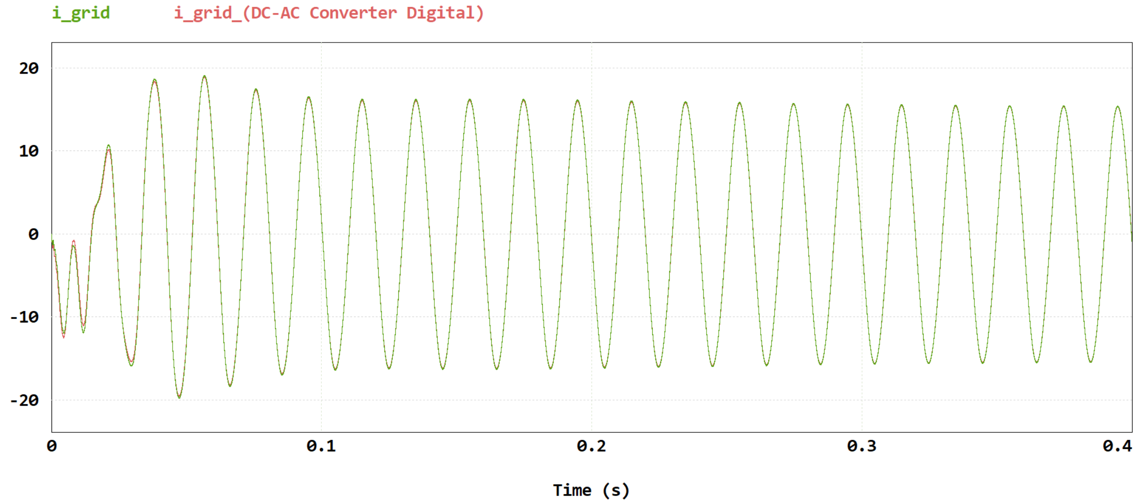

Figure 4.90: Zoom of Figure 4.88

Figure 4.91 is a zoomed version of the initial deciseconds of the Figure 4.89, the DC voltage of the digital simulation is bigger than the one from the analogue simulation from $0s$ to $0,13s$, then from $0,13s$ to $0,3s$ the DC voltage of the digital simulation is smaller than the one from the analogue simulation. After $0,3s$ the waveforms overlap each other.

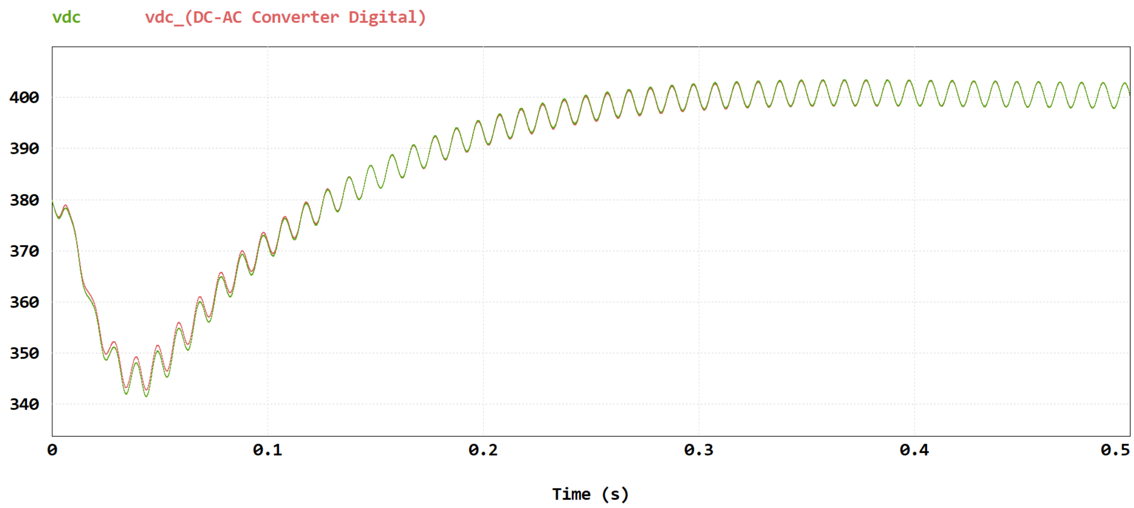

Figure 4.91: Zoom of Figure 4.89

One reason for differences in the waveforms could be attributed to the digital control passing through a Zero-Order Hold (ZOH), which samples data every $\frac{1}{10000}$s (with a sampling frequency of 10000). This introduces delays in the control process. Figure 4.92 displays the phase angle obtained from the PLL for both analogue and digital simulations. Upon closer inspection in Figure 4.93, it becomes apparent that the digital angle is delayed compared to the analogue angle. Figure 4.94 provides a zoomed-in view of the data box from Figure 4.93, showing that the delay is approximately 99ns, which closely aligns with the $\frac{1}{10000}$s sampling interval.

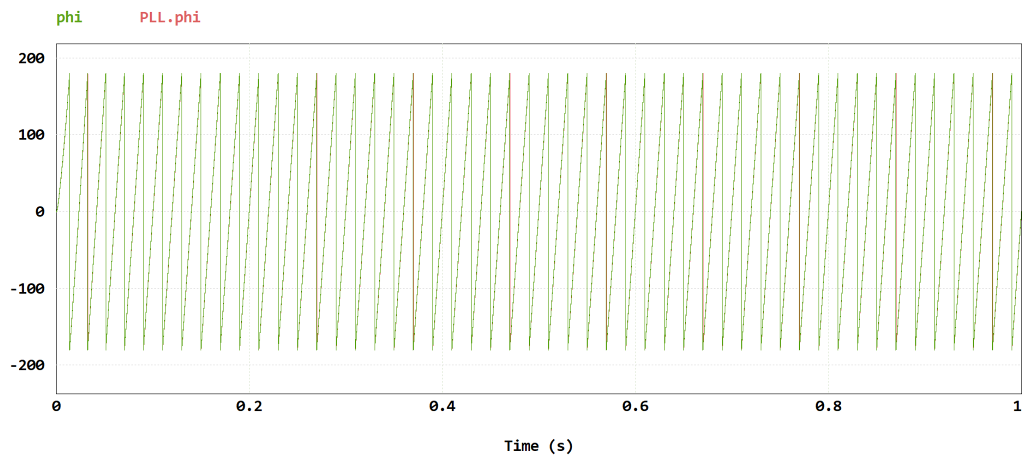

Figure 4.92: Comparison between the phi of the analogue simulation, in green, and the phi of the digital simulation, in red.

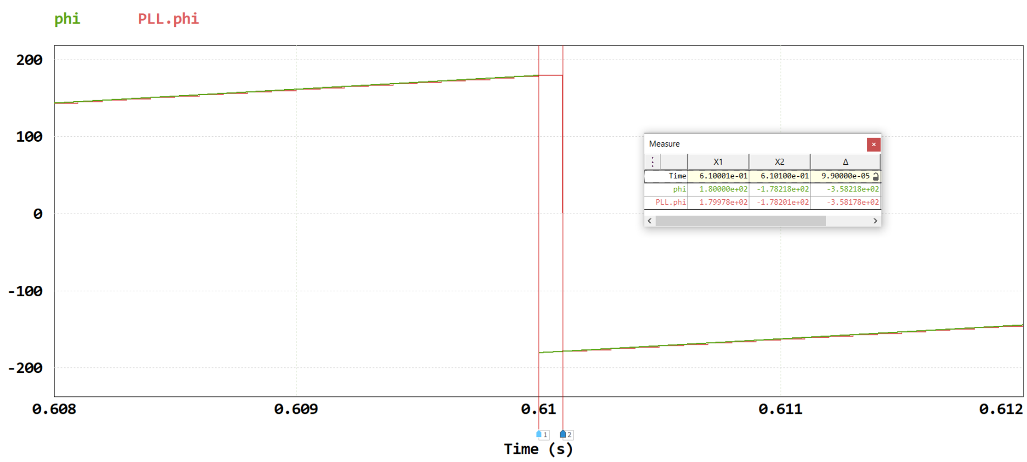

Figure 4.93: Zoom of Figure 4.92

Measure

⋮	X1	X2	Δ
Time	6.10001e-01	6.10100e-01	9.90000e-05
phi	1.80000e+02	-1.78218e+02	-3.58218e+02
PLL.phi	1.79978e+02	-1.78201e+02	-3.58178e+02

Figure 4.94: Zoom of data box shown in Figure 4.93

Another factor contributing to differences is the behaviour of the ZOH, which retains sampled values until the next sampling point (as illustrated in Figure 4.95). This characteristic can lead the control system to smooth out noise in waveforms, as evident in Figure 4.96, where i_α and i_β in the digital simulation approximate i_α and i_β in the analogue simulation, but without the noise. This smoothing effect can introduce slight discrepancies in the control waveforms between analogue and digital simulations.

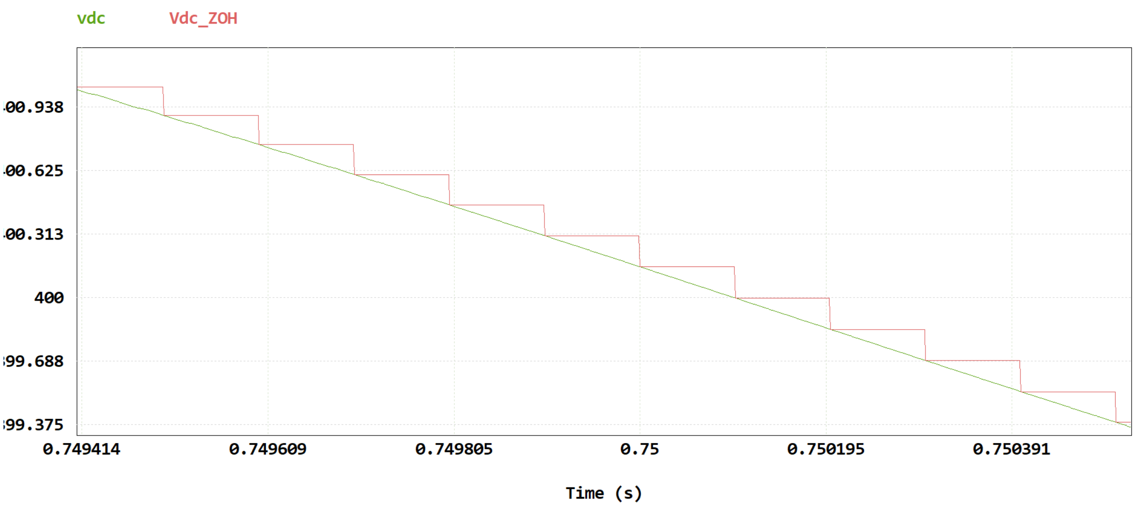

Figure 4.95: DC voltage, in red, and DC voltage after passing through the ZOH, in blue.

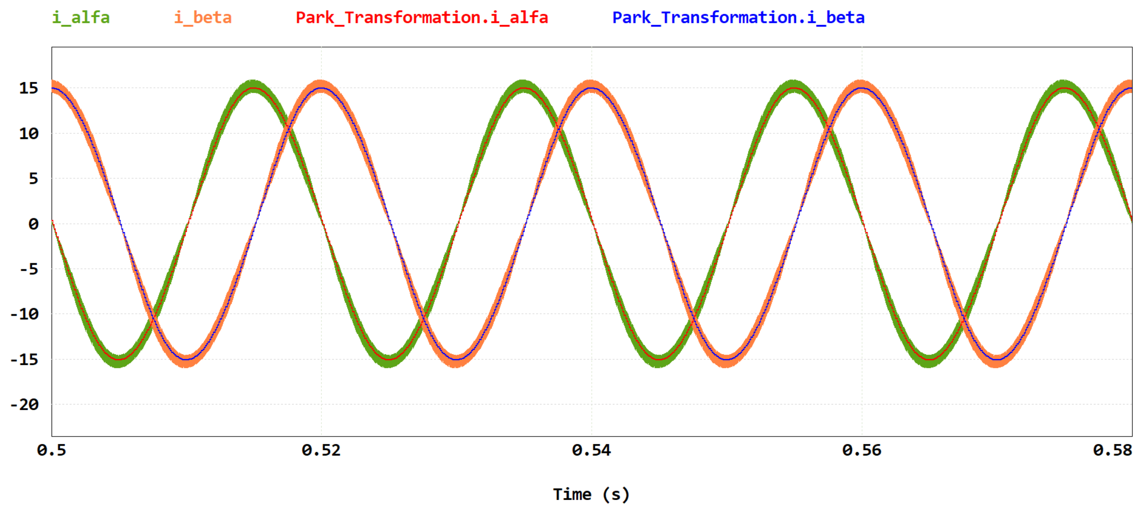

Figure 4.96: Waveforms of i_α and i_β for the digital simulation, in red and blue respectively, and for the analogue simulation, in green and orange respectively.

4.4.2.2 Comparison of Case 2

The waveforms obtained from the analogue and digital simulations for case 2, were very similar to each other, as shown in Figure 4.97 and 4.98.

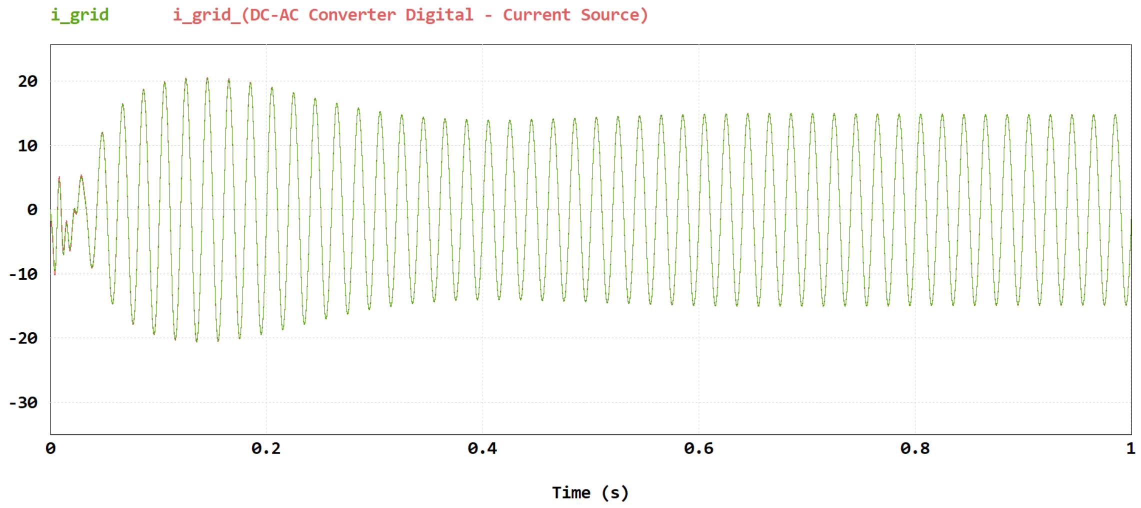

Figure 4.97: Comparison between the grid current of the analogue simulation, in green, and the grid current of the digital simulation, in red, for case 2.

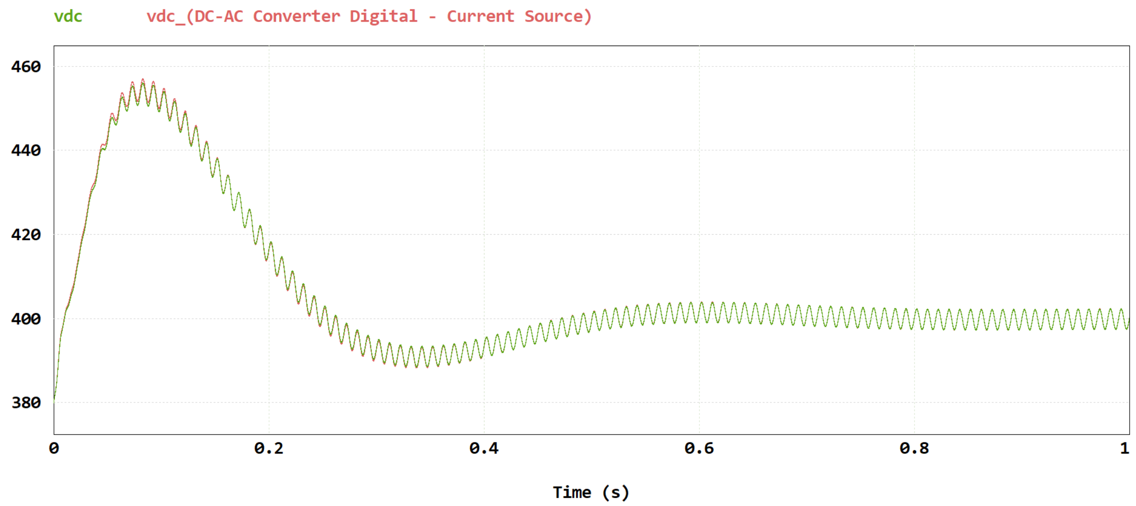

Figure 4.98: Comparison between the DC voltage of the analogue simulation, in green, and the DC voltage of the digital simulation, in red, for case 2.

Figure 4.99 shows a zoomed version of the initial deciseconds of the Figure 4.97, and here it can be seen that from $0s$ to $0,006s$, from $0,017s$ to $0,02s$, from $0,24s$ to $0,025s$, from $0,27s$ to $0,03s$ and $0,36s$ to $0,2s$ the absolute value of the amplitude of the current in the digital simulation is bigger than the one from the analogue simulation, from $0,006s$ to $0,017s$, from $0,02s$ to $0,024s$, from $0,025s$ to $0,027s$ and $0,03s$ to $0,036s$ the absolute value of the amplitude of the current in the digital simulation is smaller than the one from the analogue simulation and after the $0,2s$ both waveforms are the same.

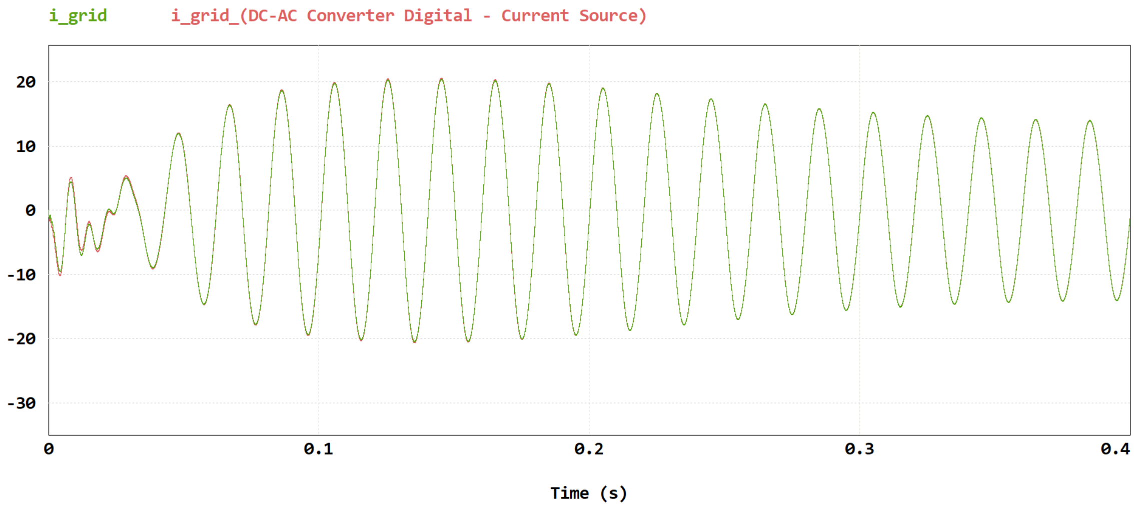

Figure 4.99: Zoom of Figure 4.97.

Figure 4.100 is a zoomed version of the initial deciseconds of the Figure 4.98, the DC voltage of the digital simulation is bigger than the one from the analogue simulation from $0s$ to $0,165s$, then from $0,165s$ to $0,4s$ the DC voltage of the digital simulation is smaller than the one from the analogue simulation. After $0,4s$ the waveforms overlap each other.

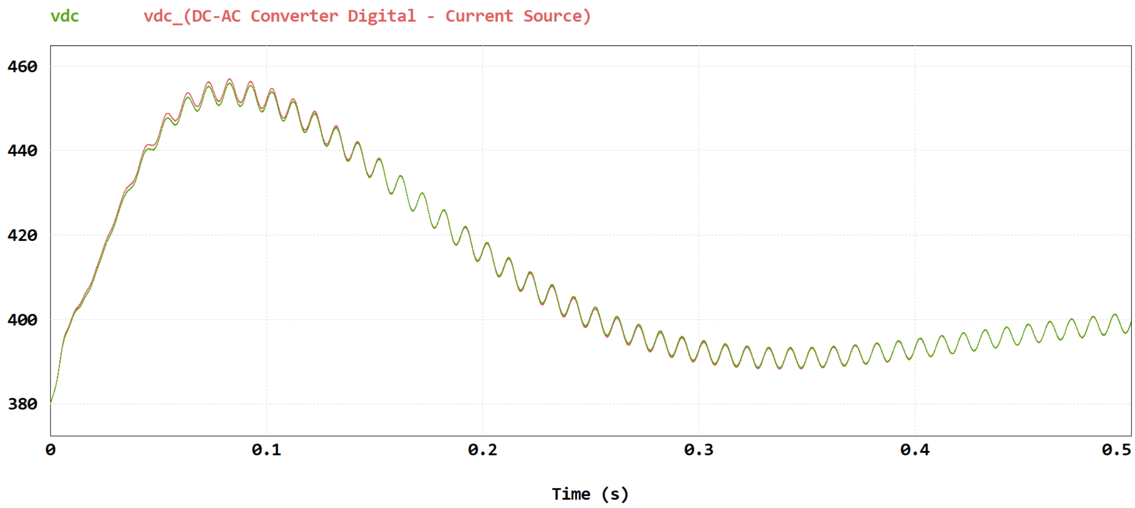

Figure 4.100: Zoom of Figure 4.98

4.4.2.3 Comparison of Case 3

The waveforms obtained from the analogue and digital simulations for case 3, were very similar to each other, as shown in Figure 4.101 and 4.102.

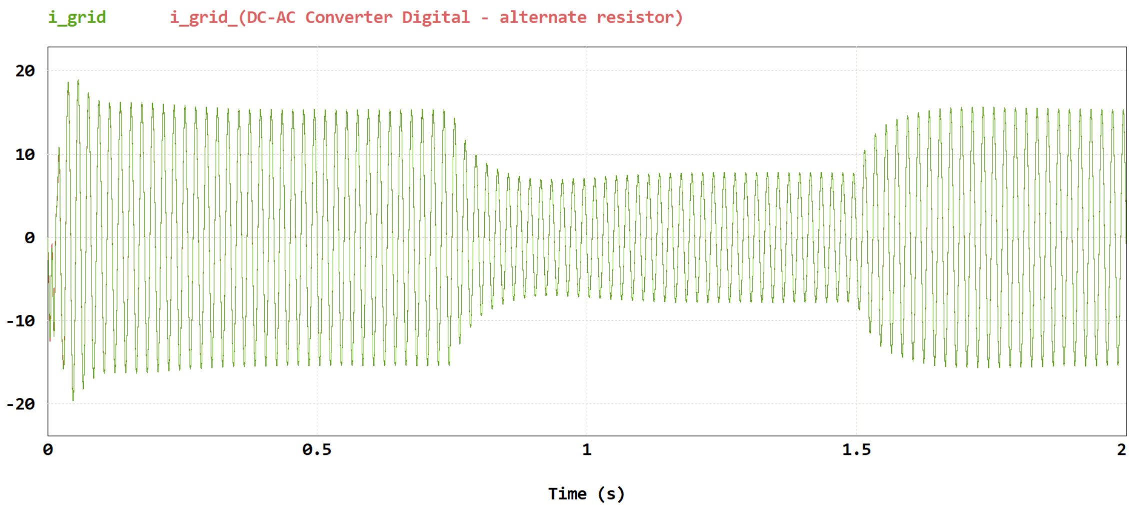

Figure 4.101: Comparison between the grid current of the analogue simulation, in green, and the grid current of the digital simulation, in red, for case 3.

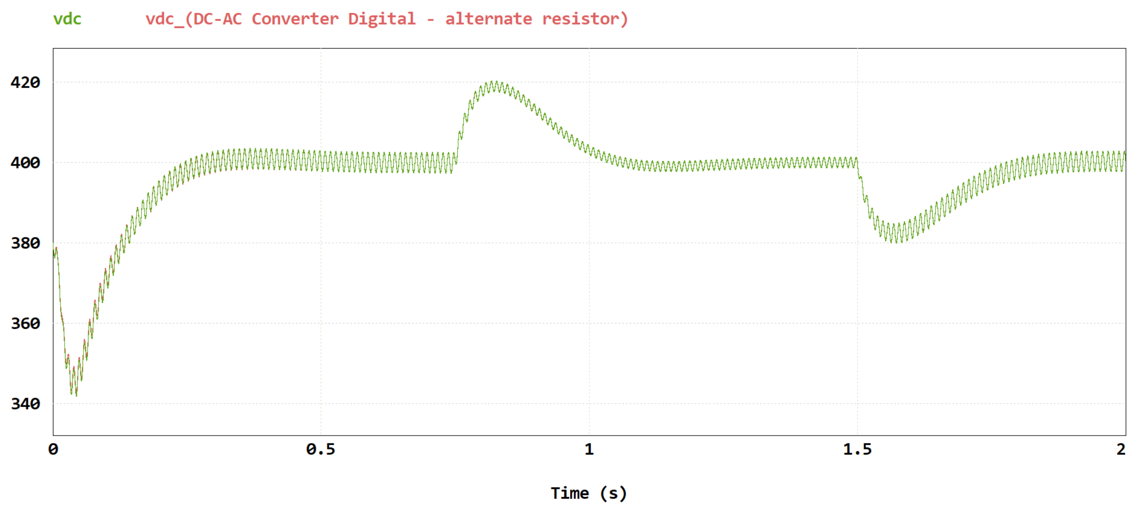

Figure 4.102: Comparison between the DC voltage of the analogue simulation, in green, and the DC voltage of the digital simulation, in red, for case 3.

Figure 4.103 shows a zoomed version of the initial deciseconds of the Figure 4.101, and here it can be seen that from $0s$ to $0,006s$ the absolute value of the amplitude of the current in the digital simulation is bigger than the one from the analogue simulation, from $0,006s$ to $0,043s$ and $0,09s$ to $0,26s$ the absolute value of the amplitude of the current in the digital simulation is smaller than the one from the analogue simulation and from and $0,043s$ to $0,09s$ after the $0,2s$ both waveforms are the same.

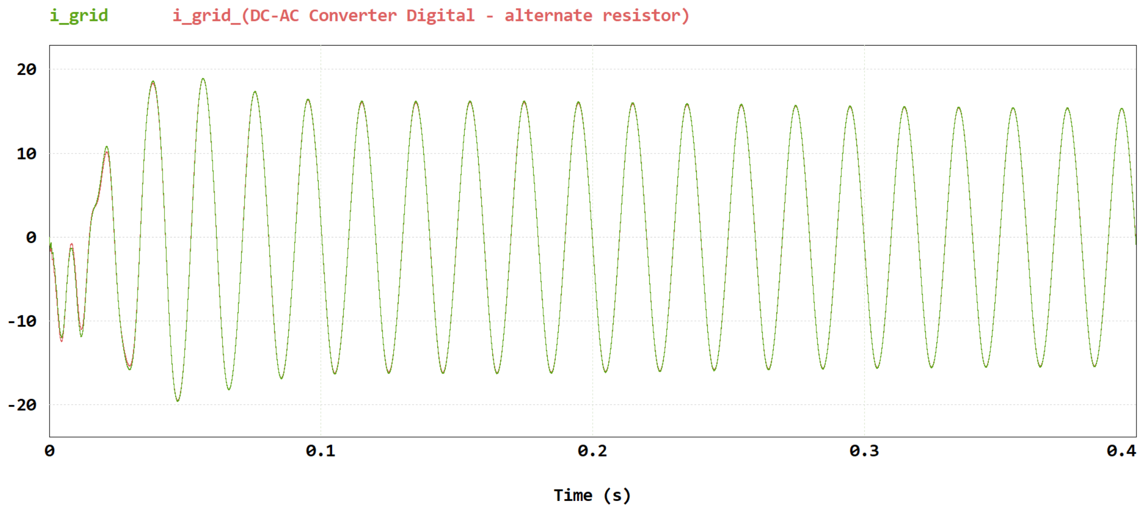

Figure 4.103: Zoom of Figure 4.101.

Figure 4.104 is a zoomed version of the initial deciseconds of the Figure 4.102, the DC voltage of the digital simulation is bigger than the one from the analogue simulation from $0s$ to $0,165s$, then from $0,165s$ to $0,38s$ the DC voltage of the digital simulation is smaller than the one from the analogue simulation. After $0,38s$ the waveforms overlap each other.

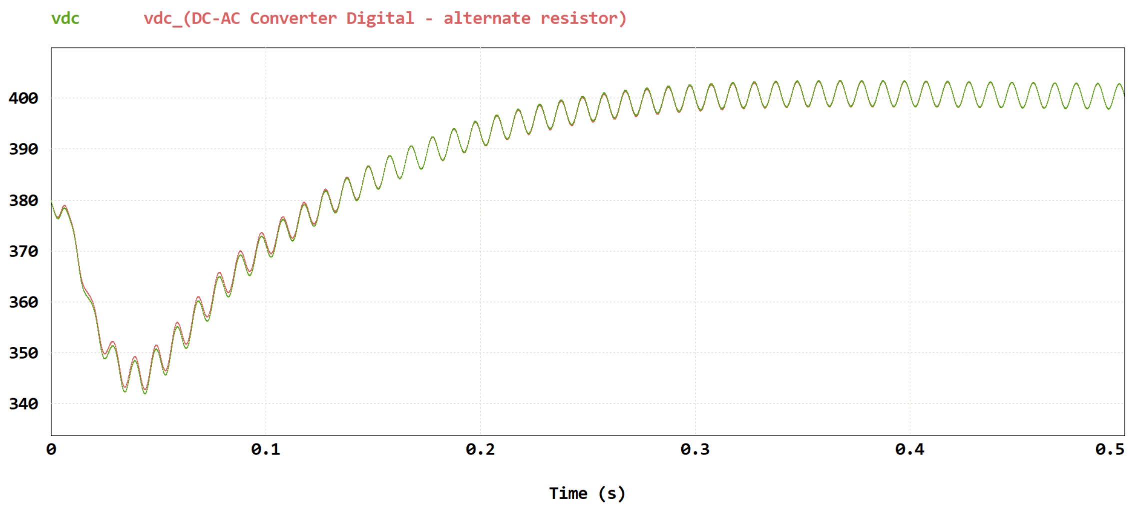

Figure 4.104: Zoom of Figure 4.102.

4.4.2.4 Comparison of Case 4

The waveforms obtained from the analogue and digital simulations for case 4, were very similar to each other, as shown in Figure 4.105 and 4.106.

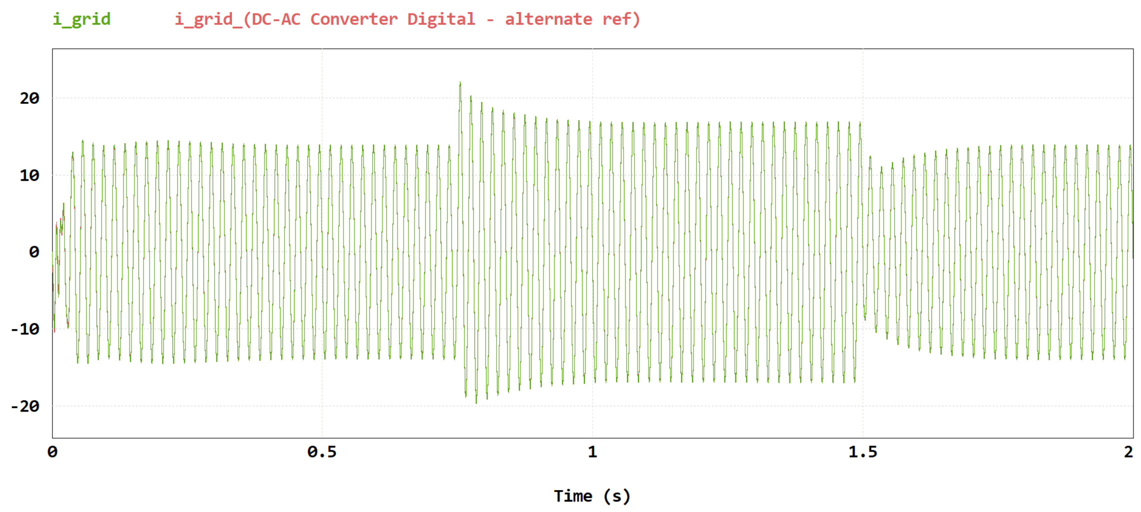

Figure 4.105: Comparison between the grid current of the analogue simulation, in green, and the grid current of the digital simulation, in red, for case 4.

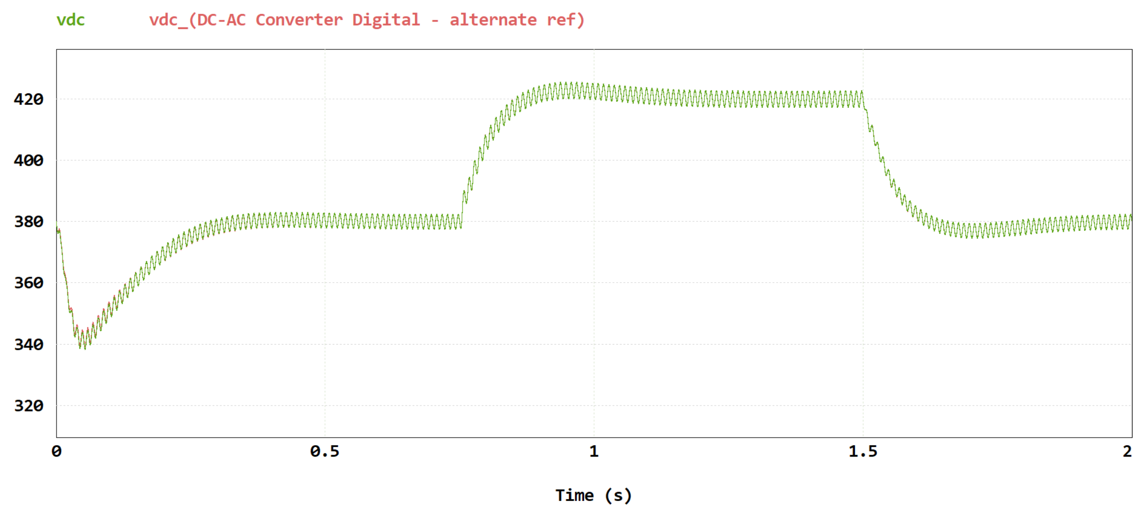

Figure 4.106: Comparison between the DC voltage of the analogue simulation, in green, and the DC voltage of the digital simulation, in red, for case 4.

Figure 4.107 shows a zoomed version of the initial deciseconds of the Figure 4.105, and here it can be seen that from $0s$ to $0,006s$ the absolute value of the amplitude of the current in the digital simulation is bigger than the one from the analogue simulation, from $0,006s$ to $0,043s$ and $0,09s$ to $0,24s$ the absolute value of the amplitude of the current in the digital simulation is smaller than the one from the analogue simulation and from and $0,043s$ to $0,09s$ after the $0,2s$ both waveforms are the same.

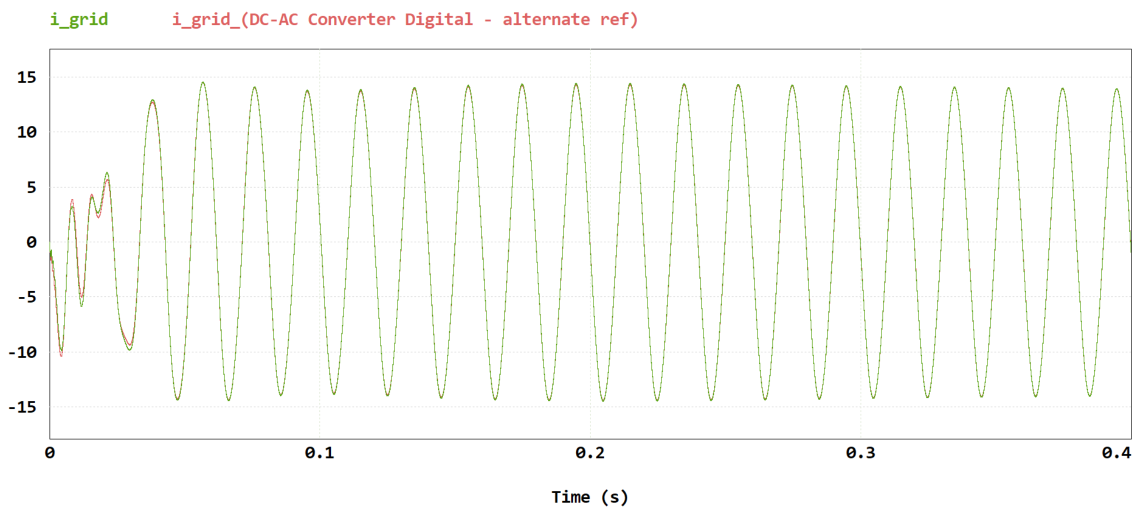

Figure 4.107: Zoom of Figure 4.105.

Figure 4.108 is a zoomed version of the initial deciseconds of the Figure 4.106, the DC voltage of the digital simulation is bigger than the one from the analogue simulation from $0s$ to $0,165s$, then from $0,165s$ to $0,38s$ the DC voltage of the digital simulation is smaller than the one from the analogue simulation. After $0,38s$ the waveforms overlap each other.

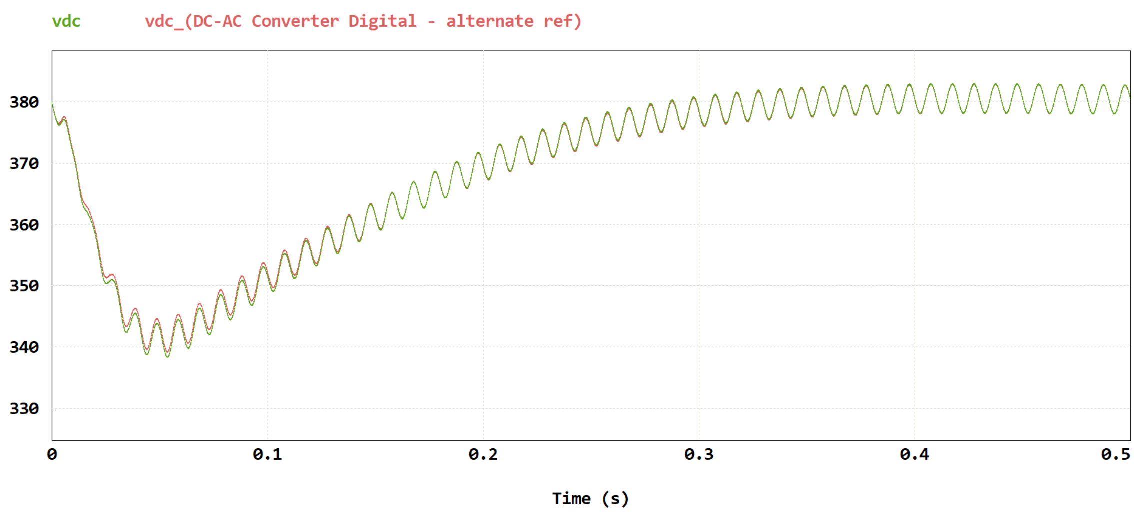

Figure 4.108: Zoom of Figure 4.106.

4.4.2.5 Comparison of Case 5

The waveforms obtained from the analogue and digital simulations for case 5, were very similar to each other, as shown in Figure 4.109 and 4.110.

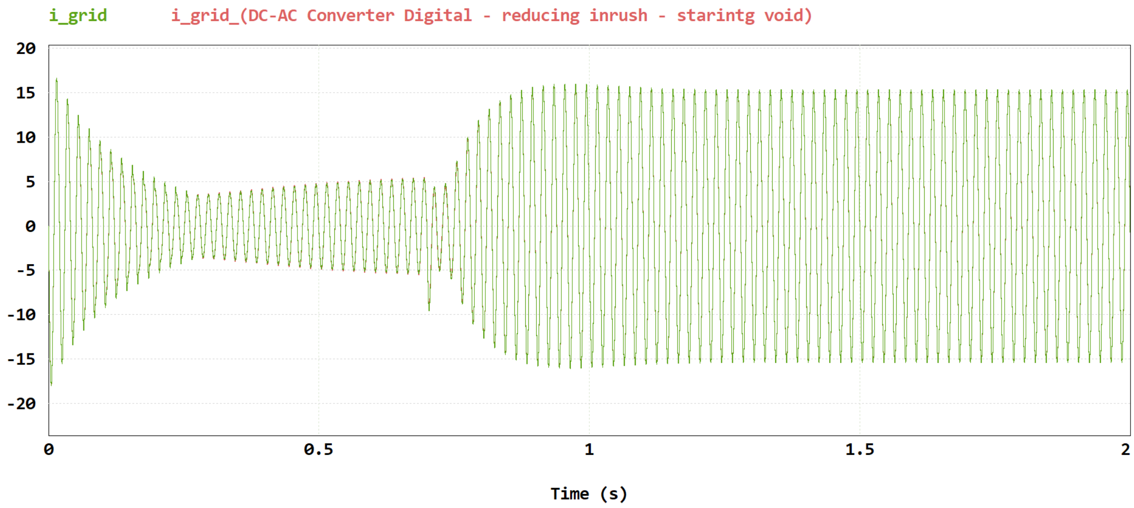

Figure 4.109: Comparison between the grid current of the analogue simulation, in green, and the grid current of the digital simulation, in red, for case 5.

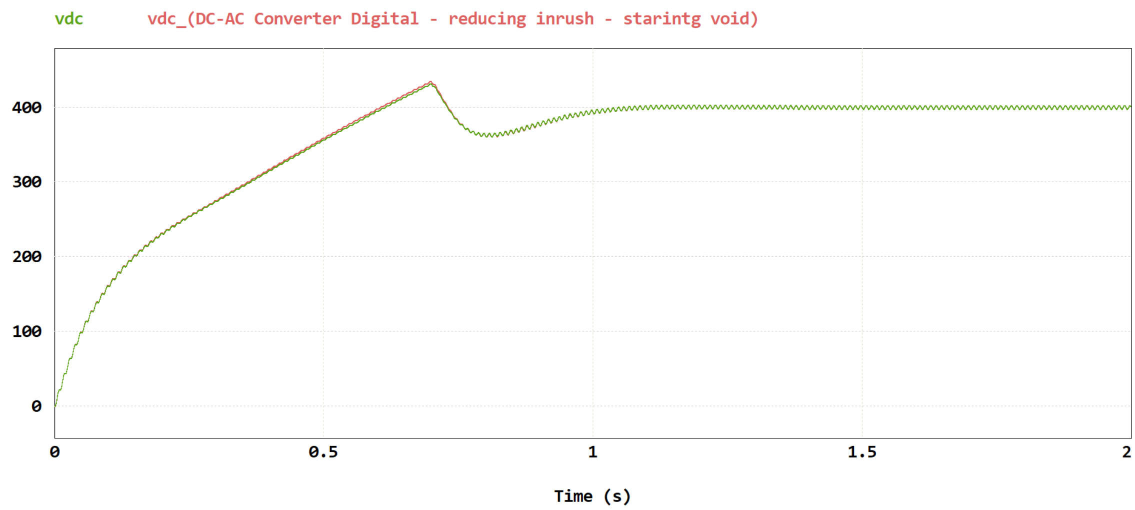

Figure 4.110: Comparison between the DC voltage of the analogue simulation, in green, and the DC voltage of the digital simulation, in red, for case 5.

Figures 4.111, 4.112 and 4.113 shows a zoomed versions of the Figure 4.109, from $0s$ to $0,3s$, $0,2s$ to $0,7s$ and $0,6s$ to $1s$ respectively. From these Figures, it can be seen that from $0,26s$ to $0,7s$ the absolute value of the amplitude of the current in the digital simulation is bigger than the one from the analogue simulation, from $0,7s$ to $0,91s$ the absolute value of the amplitude of the current in the digital simulation is smaller than the one from the analogue simulation. From $0,071s$ to $0,26s$ the waveforms are distorted and the absolute value of the amplitude of the current in the digital simulation is smaller in relation to one from the analogue simulation in these distortions. Both waveforms are the same from $0s$ to $0,071s$ and after $0,91s$.

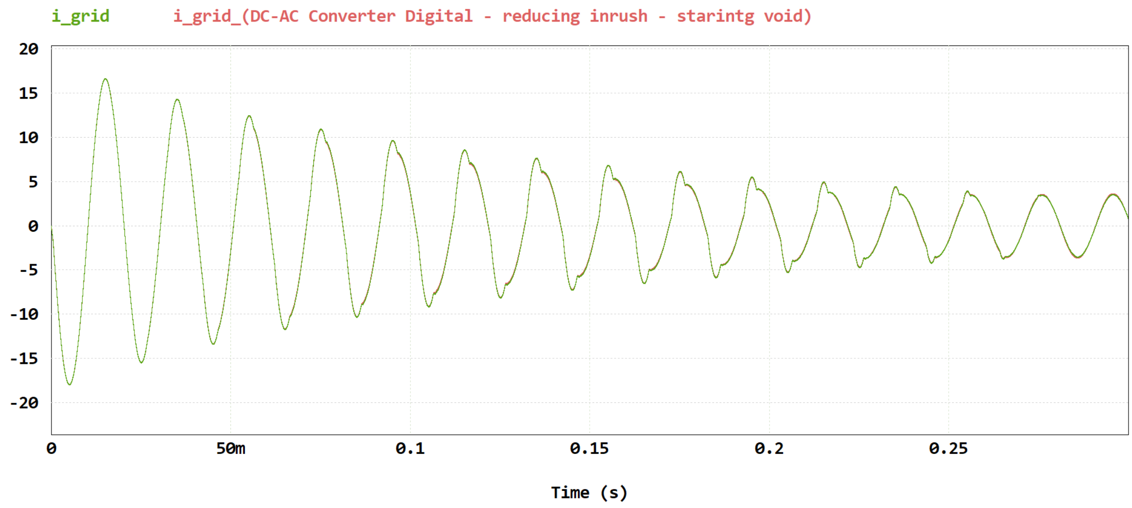

Figure 4.111: Zoom of Figure 4.109 from 0s to 0,3s.

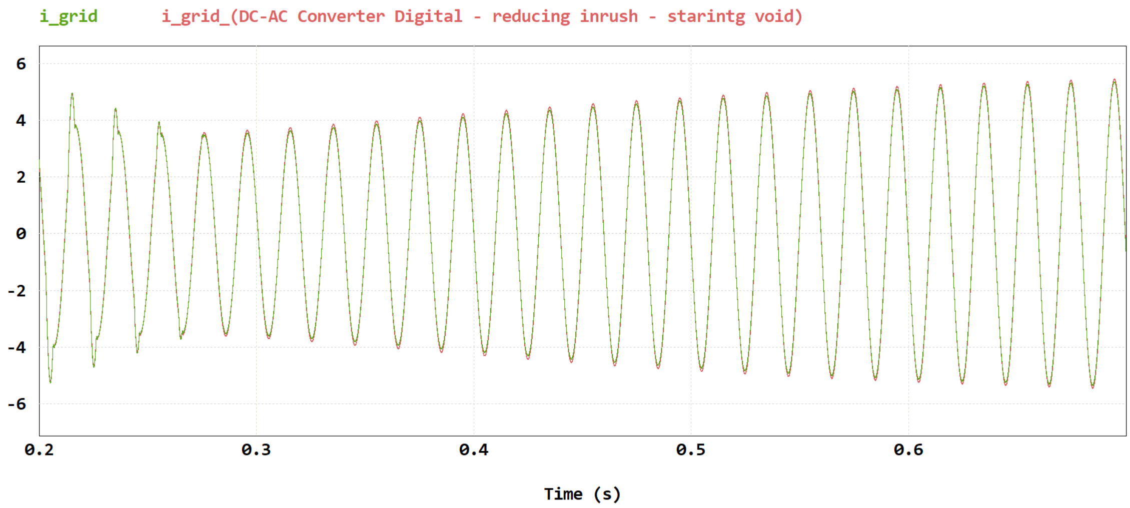

Figure 4.112: Zoom of Figure 4.109 from 0,2s to 0,7s.

Figures 4.114 and 4.115 are a zoomed versions of the Figure 4.110 from $0,02s$ to $0,1s$ and $0,5s$ to $1,2s$ respectively. The DC voltage of the digital simulation is bigger than the one from the analogue simulation from $0,027s$ to $0,88s$, then from $1,18s$ to $1,49s$ the DC voltage of the digital simulation is smaller than the one from the analogue simulation. The waveforms overlap each other before the $0,027s$ and after the $1,09s$.

4.4.2.6 Results Discussion

With the simulations, it can be concluded that the digital control is working as it was supposed to since the results obtained with digital control are similar to those obtained with analogue control.

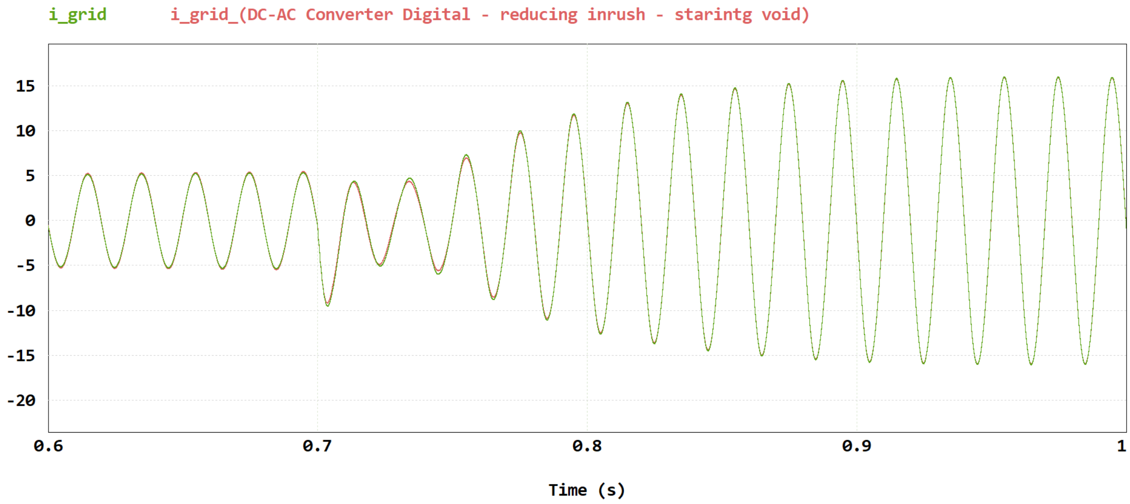

Figure 4.113: Zoom of Figure 4.109 from 0,6s to 1s.

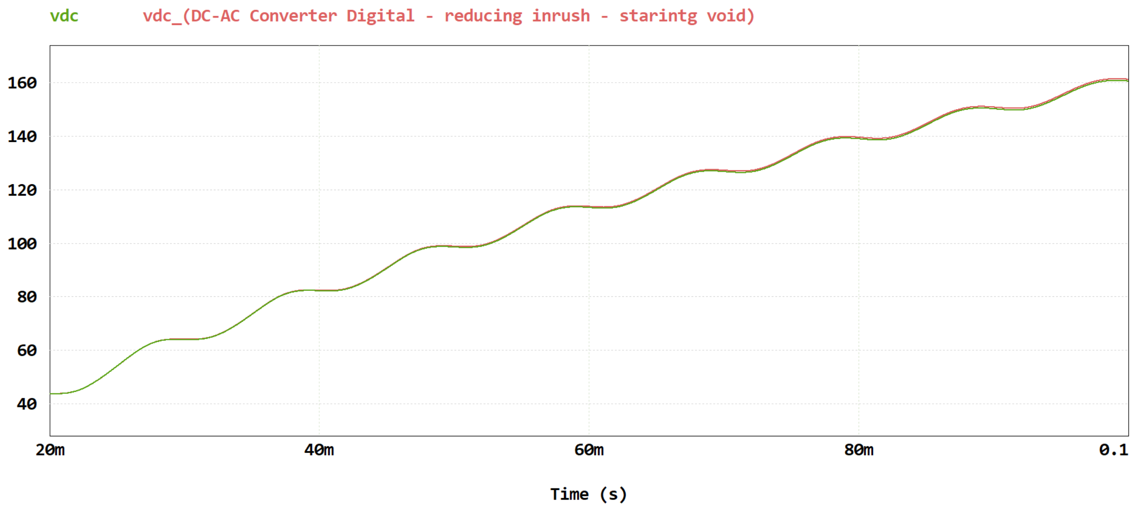

Figure 4.114: Zoom of Figure 4.110 from 0,02s to 0,1s.

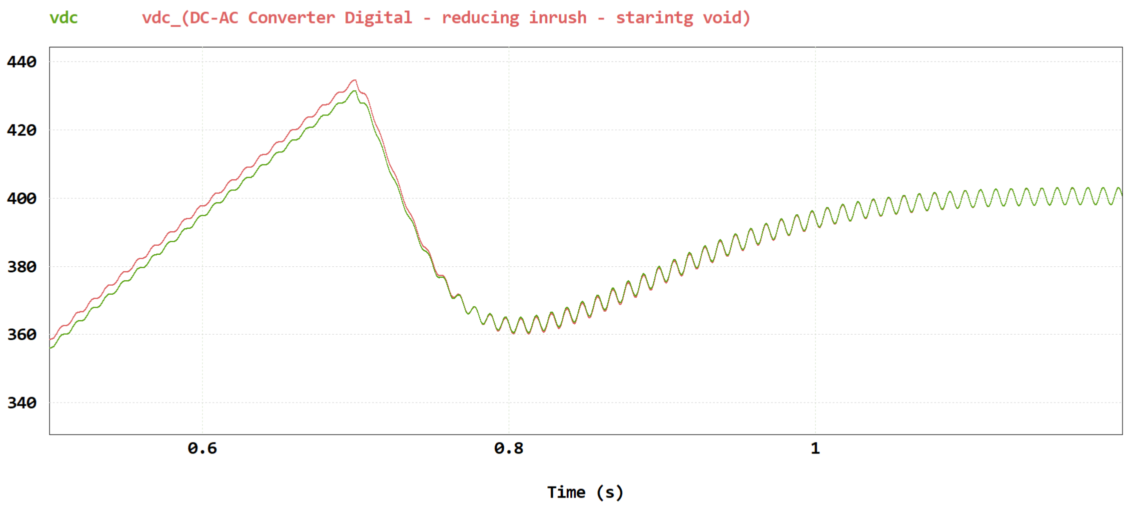

Figure 4.115: Zoom of Figure 4.110 from 0,5s to 1,2s

4.5 Summary

This chapter focused on the modelling and simulation of the proposed bidirectional converter for the UPWIND project. It detailed the development of the converter's model, including the LCL filter and d-q transformation. The chapter presented simulations for both analogue and digital control, addressing various operational scenarios such as normal operation with load, current source, and alternate load. The results were compared to determine the effectiveness of the proposed system under different conditions.

Chapter 5

Conclusion and Future Work

5.1 Main Conclusions

This dissertation has successfully demonstrated the design and simulation of a bidirectional converter using PSIM. The converter exhibited effective dynamic response, and robust bidirectional operation in simulations. While the findings provide valuable insights into the converter's performance, further research and real-world testing are necessary to fully realize its potential in practical applications.

5.2 Future Work

While the development of the bidirectional converter presented in this dissertation has achieved significant results in terms of theoretical design and initial simulations, several critical tasks remain unaddressed. To realize the full potential of the converter, the following areas require further attention:

- **Testing of SiC and GaN Transistors** - Testing SiC and Gan transistors through simulations and comparing them with IGBTs and MOSFETs.
- **Implementation of the control circuit in programming code** - Implementing the control circuit done in the simulations into code so that it can be integrated with the hardware setup to be implemented.
- **Hardware Implementation and Testing** - Development of a physical prototype of the bidirectional converter based on the final design specifications. Verification of basic functionality and identification of any initial issues by carefully powering up the hardware prototype. Execution of a series of rigorous tests to validate the performance, reliability, and safety of the converter. These tests include functional testing, performance testing, and stress and safety testing. And based on the test results, make iterations to the hardware design to address any issues, improve efficiency, and enhance reliability.

References

[1] OHCHR. "About the 2030 Agenda on Sustainable Development". URL: https://www.ohchr.org/en/sdgs/about-2030-agenda-sustainable-development [last accessed June 26, 2024].

[2] UN. "THE 17 GOALS | Sustainable Development". URL: https://sdgs.un.org/goals [last accessed June 26, 2024].

[3] Cristina L. Archer. An introduction to meteorology for airborne wind energy. In U. Ahrens, M. Diehl, and R. Schmehl, editors, *Airborne Wind Energy*, chapter 5, pages 81–94. Springer Berlin Heidelberg, Berlin, Heidelberg, 2013.

[4] A. Cherubini. "Why Airborne Wind Energy". AWE Blog. URL: https://www.antonellocherubini.com/why-airborne-wind-energy.html [last accessed November 08, 2023].

[5] U. Ahrens. Basic differences of wind utilization concepts. In U. Ahrens, editor, *Airborne Wind Energy: An Overview of the Technological Approaches*, chapter 2, pages 5–28. Springer International Publishing, Cham, 2023.

[6] Ricardo P. Aguilera, Pablo Acuna, Georgios Konstantinou, Sergio Vazquez, and Jose I. Leon. Basic control principles in power electronics. In Frede Blaabjerg, editor, *Control of Power Electronic Converters and Systems*, volume 1, chapter 2, pages 31–68. Academic Press, London, 1st ed edition, 2018.

[7] M.P. Kazmierkowskia, M. Malinowski, and M. Bech. Pulse width modulation techniques for three-phase source converters. In M.P. Kazmierkowski, R. Krishnan, and F. Blaabjerg, editors, *Control in Power Electronics*, chapter 4, pages 89–160. Academic Press, Burlington, 1st ed edition, 2002.

[8] A. Schönung and H. Stemmler. Static frequency changers with subharmonic control in conjunction with reversible variable speed ac drives. *The Brown Boveri review*, 51:555–577, 1964.

[9] S.R. Bowes. New sinusoidal pulsewidth-modulated invertor. *Proceedings of the Institution of Electrical Engineers*, 122(11):1279—-1285, November 1975.

[10] N. Mohan, T.M. Undeland, and W.P. Robbins. *Power Electronics—Converters, Applications and Design*. John Wiley & Sons, Hoboken, NJ, 3rd ed edition, 2003.

[11] D. N. Zmood and D. G. Holmes. Stationary frame current regulation of pwm inverters with zero steady-state error. *IEEE Transactions on Power Electronics*, 18(3):814—-822, May 2003.

[12] C. Buccella, C. Cecati, and H. Latafat. Digital control of power converters—a survey. *IEEE Transactions on Industrial Informatics*, 8(3):437—-447, August 2012.

[13] Karl Johan Åström and Björn Wittenmark. *Computer-Controlled Systems: Theory and Design*. Prentice Hall, Upper Saddle River, NJ, 3rd ed edition, 1997.

[14] M. Chinnari, T. Mounika, K. Swetha, A. Bharathi, and Allamsetty Hema Chander. Implementation of hysteresis voltage control for different inverter topologies. In *2020 IEEE India Council International Subsections Conference (INDISCON)*, pages 272–277. IEEE, October 2020. URL: https://ieeexplore.ieee.org/document/9344527/.

[15] I. Takahashi and T. Noguchi. A new quick-response and high-efficiency control strategy of an induction motor. *IEEE Transactions on Industry Applications*, IA-22(5):820—-827, September 1986.

[16] T. Noguchi, H. Tomiki, S. Kondo, and I. Takahashi. Direct power control of pwm converter without power-source voltage sensors. *IEEE Transactions on Industry Applications*, 34(3):473—479, May 1998.

[17] R. Campos, L. Pinto, J. Oliveira, A. Nied, L. Marques, and A. Souza. Single-phase induction motor control based on dtc strategies. In *2007 IEEE International Symposium on Industrial Electronics*, pages 1068—1073. IEEE, June 2007. URL: https://ieeexplore.ieee.org/document/4374746.

[18] M. A. Djema and M. Boudour. Optimized direct power control for single phase grid-connected inverters. In *2019 Algerian Large Electrical Network Conference (CAGRE)*, pages 1—-6. IEEE, February 2019. URL: http://ieeexplore.ieee.org/document/6120037/.

[19] S. Kouro, P. Cortes, R. Vargas, U. Ammann, and J. Rodriguez. Model predictive control—a simple and powerful method to control power converters. *IEEE Transactions on Industrial Electronics*, 56(6):1826—-1838, June 2009.

[20] D. E. Quevedo, R. P. Aguilera, and T. Geyer. Predictive control in power electronics and drives: Basic concepts, theory, and methods. In T. Orłowska-Kowalska, F. Blaabjerg, and J. Rodríguez, editors, *Advanced and Intelligent Control in Power Electronics and Drives*, chapter 5, pages 181–226. Springer International Publishing, Cham, 2014.

[21] S. Vazquez, J. Rodriguez, M. Rivera, L. G. Franquelo, and M. Norambuena. Model predictive control for power converters and drives: Advances and trends. *IEEE Transactions on Industrial Electronics*, 64(2):935—947, 2017.

[22] R. P. Aguilera, Pablo Acuña, Pablo Lezana, Georgios Konstantinou, Bin Wu, Steffen Bernet, and Vassilios G. Agelidis. Selective harmonic elimination model predictive control for multilevel power converters. *IEEE Transactions on Power Electronics*, 32(3):2416—-2426, March 2017.

[23] Tech Simulator. *Design of LCL Filter for single phase grid connected inverter.*, 31 May 2020. URL: https://www.youtube.com/watch?v=ZNUqGBBlKLI [last accessed July 23, 2024].

[24] J. Farhood. *"MODELLING, DESIGN AND IMPLEMENTATION OF D-Q CONTROL IN SINGLE-PHASE GRID-CONNECTED INVERTERS FOR PHOTOVOLTAIC SYSTEMS USED IN DOMESTIC DWELLINGS".* Phd dissertation, De Montfort Univ., Leicester, 2013. https://dora.dmu.ac.uk/server/api/core/bitstreams/d8297db4-c5e8-4a20-9a18-bfaea4527823/content.

[25] Renata Carnieletto, Diego B. Ramos, Marcelo G. Simões, and Felix A. Farret. Simulation and analysis of dq frame and p+resonant controls for voltage source inverter to distributed generation. In *2009 Brazilian Power Electronics Conference*, pages 104–109, 2009. doi:10.1109/COBEP.2009.5347677.

[26] B. Saritha and P. A. Jankiraman. Observer based current control of single-phase inverter in dq rotating frame. In *2006 International Conference on Power Electronic, Drives and Energy Systems*, pages 1–5, 2006. doi:10.1109/PEDES.2006.344427.

[27] B. Crowhurst, E. F. El-Saadany, L. El Chaar, and L. A. Lamont. Single-phase grid-tie inverter control using dq transform for active and reactive load power compensation. In *2010 IEEE International Conference on Power and Energy*, pages 489–494, 2010. doi:10.1109/PECON.2010.5697632.

[28] G. Franceschini, E. Lorenzani, C. Tassoni, and A. Bellini. Synchronous reference frame grid current control for single-phase photovoltaic converters. In *2008 IEEE Industry Applications Society Annual Meeting*, pages 1–7, 2008. doi:10.1109/08IAS.2008.74.

[29] Nayeem A. Ninad, Luiz A. C. Lopes, and Alfred Rufer. A vector controlled single-phase voltage source inverter with enhanced dynamic response. In *2010 IEEE International Symposium on Industrial Electronics*, pages 2891–2896, 2010. doi:10.1109/ISIE.2010.5637255.

[30] S. Samerchur, S. Premrudeepreechacharn, Y. Kumsuwun, and K. Higuchi. Power control of single-phase voltage source inverter for grid-connected photovoltaic systems. In *2011 IEEE/PES Power Systems Conference and Exposition*, pages 1–6, 2011. doi:10.1109/PSCE.2011.5772504.

[31] Powersim Inc. *PSIM User's Manual.* Altair Engineering, 2020a edition, May 2020. Available at https://powersimtech.com/wp-content/uploads/2021/01/PSIM-User-Manual.pdf.

[32] Infineon Technologies. "High speed DuoPack: IGBT in Trenchand Fieldstop technology with soft, fast recovery anti-parallel diode", 2014-03-12. IKW30N60H3 datasheet.

[33] Infineon Technologies, Munich, Germany. *Calculate and minimize the dead time for IGBTs*, Dec. 2021. AN2007-04. URL: https://www.infineon.com/dgdl/Infineon-Deadtime_calculation_for_IGBT_modules-ApplicationNotes-v01_10-EN.pdf?fileId=db3a30431a5c32f2011a5daefc41005b.

[34] Bourns. "BIDNW30N60H3 Insulated Gate Bipolar Transistor (IGBT)", Mar 31, 2015. BIDNW30N60H3 datasheet.

[35] Infineon Technologies. "600V CoolMOS™ C7 Power Transistor", 2015-05-08. IPZ60R040C7 datasheet.

[36] IXYS Corporation. "Linear L2TM Power MOSFET with extended FBSOA", 2009. IXTH30N60L2 datasheet.

[37] MOUSER ELECTRONICS. "Infineon Technologies IKW30N60H3". MOUSER ELECTRONICS. URL: https://www.mouser.fr/ProductDetail/Infineon-Technologies/IKW30N60H3?qs=mzcOS1kGbgc1YDq2tvWpXg%3D%3D [last accessed June 21, 2024].

[38] MOUSER ELECTRONICS. "Bourns BIDNW30N60H3". MOUSER ELECTRONICS. URL: https://www.mouser.fr/ProductDetail/Bourns/BIDNW30N60H3?qs=vvQtp7zwQdMXAvgNNIVqLQ%3D%3D [last accessed June 22, 2024].

[39] MOUSER ELECTRONICS. "Infineon Technologies IPZ60R040C7XKSA1". MOUSER ELECTRONICS. URL: https://www.mouser.fr/ProductDetail/Infineon-Technologies/IPZ60R040C7XKSA1?qs=CVaTMblcXgg0FHF5dfBIwQ%3D%3D [last accessed June 22, 2024].

[40] MOUSER ELECTRONICS. "IXYS IXTH30N60L2". MOUSER ELECTRONICS. URL: https://www.mouser.fr/ProductDetail/IXYS/IXTH30N60L2?qs=cvHLLyFtoE0YL9AxQNeufw%3D%3D [last accessed June 22, 2024].